Space Sci Rev (2010) 152: 23–97
DOI 10.1007/s11214-010-9643-1

Planetary Magnetic Field Measurements: Missions and Instrumentation

André Balogh

Received: 7 January 2010 / Accepted: 26 February 2010 / Published online: 30 April 2010

Abstract The nature and diversity of the magnetic properties of the planets have been investigated by a large number of space missions over the past 50 years. It is clear that without the magnetic field measurements that have been carried out in the vicinity of all the planets, the state of their interior and their evolution since their formation would not be understood even though questions remain about how the different planetary dynamos (in six of the eight planets) work. This paper describes the motivation for making magnetic field measurements, the instrumentation that has been used and many of the missions that carried out the pioneering observations. Emphasis is given to the historically important early missions even if the results from these have been in some cases bettered by later missions.

Keywords Planetary magnetism · Planetary space missions · Space magnetometers

1 Motivation for Measuring the Magnetic Field of Planets and Satellites

The presence or absence of a planetary scale magnetic field places a strong constraint of the state of a planet's interior. The nature of the field (dipolar, multipolar, crustal, induced or, in general, the combination of all such terms in different proportions) provides further indication of the details of the thermal evolution and current state and has been used extensively in constraining models of planetary structure. If a planet's magnetic field is dominated by dipolar and low-order multipolar terms, the presumed existence of a magnetohydrodynamic dynamo in the planet's interior is an additional, important factor in its internal dynamics.

For planets in the solar system, the interaction of the planetary obstacle with the all-pervasive solar wind critically influences the magnetic environment of planets. The interaction depends strongly on the nature of the magnetism of the planetary body, as well as on

A. Balogh (✉)
International Space Science Institute, Bern, Switzerland
e-mail: balogh@issibern.ch

A. Balogh
Imperial College, London, UK

its neutral and ionized atmosphere. The formation of magnetospheres with their often large and usually highly variable current systems (see Baumjohann et al. 2010a, this issue) leads to the magnetic field on and above the surface being a complex resultant from internal and external terms. The interpretation of magnetic field measurements needs to take into account the complex interplay of the different constituents of the measured field vector. Separation of terms of different origins is essential. The inversion problem is always a formidable task and remains impossible or ambiguous if there are not enough measurements. Because of the temporal variability of external terms, measurements not only need to cover a fine spatial grid, but have to provide data as a function of time with an appropriate temporal resolution. The problem of separating internal and external terms is discussed in more detail in this volume (Olsen et al. 2009, this issue).

The Earth's magnetic field is of course the best known in the solar system, thanks to the extensive ground-based measurements carried out with an increasing coverage and accuracy over the past centuries. For planets, on the other hand, measurements of their magnetic field is (almost) exclusively reserved for magnetometers onboard space probes that fly by or orbit the planet at a sufficiently small distance so that its magnetic environment can be detected, measured and modelled. (The exception is Jupiter; the existence of its magnetic field had been deduced from Earth-based and space-based radio astronomy measurements. These could provide an indirect estimate of some parameters of the planet's magnetic field, see, e.g. Smith and Gulkis 1979.)

In the solar system, it is now known that there is a wide variety of magnetized and unmagnetised bodies of very different sizes and different internal and external properties. All bodies for which magnetic field measurements are available present drastically different internal and external characteristics. At the start of the space age, however, thoughts about the magnetic fields of planets were based on comparisons with the Earth. This meant that Venus was considered similar to Earth in terms of its internal state, but the existence of a magnetic field had remained open, in fact quite doubtful due to the very slow rotation rate of the planet. On the other hand, Mars and Mercury, because of their smaller sizes, would have frozen out early in their history and would now have a solid core, hence unable to support a magnetohydrodynamic dynamo. The Moon would also be solid, without a large-scale magnetic field. The outer planets, starting with Jupiter, are clearly different from the terrestrial planets and the origin of their magnetic field cannot be deduced from what we know about the Earth. The status of the early results and theoretical considerations was reviewed by Stevenson (1975), after Mercury's magnetic field was discovered, and Jupiter's was first measured in situ, but before further observations allowed a much more detailed assessment of the theoretical explanations in terms of the planetary interiors and the operation of the planetary scale dynamos. The present understanding and future prospects of planetary magnetic fields are discussed in a review by Stevenson (2010, this issue).

It is remarkable that most planetary spacecraft, from the earliest missions in the 1960s, carried magnetometers, a confirmation that the importance of the magnetic field for characterizing planetary bodies was widely recognised. An example is provided by the Pioneer 10 and 11 spacecraft, the first missions to Jupiter and Saturn, which were equipped with magnetometers as part of their core payload (see Fig. 1). In this paper, the history of magnetic field instrumentation on planetary missions is reviewed, with an outline of the major milestones in both planetary exploration and magnetometer development. The first decade of magnetometry in the space age was reviewed by Smith (1969), Ness (1964, 1970) and Smith and Sonett (1976). The following decades were reviewed by Snare (1998) and Acuña (2002). Key moments in planetary magnetism are sketched out in this volume from the perspective of a leading figure in planetary missions over the past decades (Ness 2010, this issue).

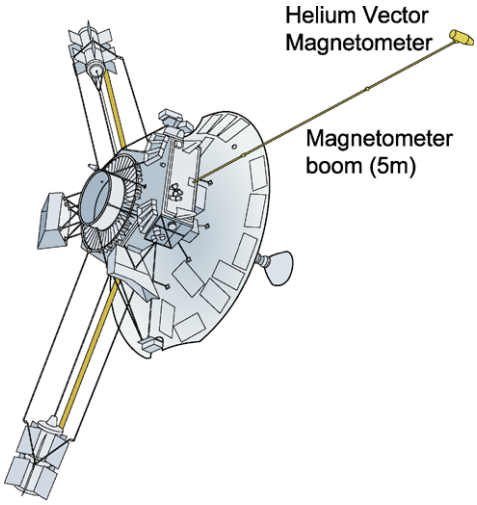

Fig. 1 Drawing of the Pioneer 10 and 11 spacecraft. The drawing shows the 5 m long magnetometer boom and the Helium Vector Magnetometer that was the first to measure in situ the magnetic fields of Jupiter and Saturn

A brief technical review of the key instrument types used on planetary missions is also presented. Only patchy instrumental information is available for some of the early missions, in particular for instruments on the Soviet programs to Mars and Venus. We also review the requirements on the instruments and on spacecraft, as well as on mission type (flyby or orbiter) to meet the scientific objectives of the missions. In order to best structure the presentation of the material, first the more general considerations about instrument type and instrument/mission requirements are described (Sect. 2). This introductory material is followed by the description of instruments and missions to specific planets in Sect. 3 for the terrestrial planets and in Sect. 4 for the outer planets.

2 Magnetometers: Sensors, Electronics, Data Processing and Calibration

The general requirements on magnetometers on different kinds of missions are listed in Table 1. While there has been improvement in the performance of magnetometers, even earlier magnetometers met, in general, these requirements (see e.g. Acuña 2002). The requirements are however not simply on the instruments, but on the measurements; stated like this, the overall performance is assessed end-to-end, combining the instruments with the spacecraft on which they are flown. Generally speaking, the limiting factor on the measurement accuracies tends to be the magnetic environment of the instrument generated by the spacecraft at the location of the magnetometer sensor. In the following, after a few general points concerning the overall functionality of magnetometers, the magnetic cleanliness issues that affect the measurements and the measures to ensure that the magnetic environment of the sensors should be compatible with the mission scientific requirements will be described briefly.

There are two important classes of magnetometers that have been flown on planetary missions. These are the fluxgate type, the most widely used space magnetometer, first at Mercury, the Moon, Venus, Uranus and Neptune, and the vector helium magnetometer that has flown on fewer missions, but in fact was the first to provide usable measurements near Mars, and the first to describe the fields of Jupiter and Saturn. Fluxgate magnetometers subsequently flew also on missions to Mars (determining on the Mars Global Surveyor the origin of Mars' magnetic field) and to Jupiter and Saturn, increasing the observational data base for their magnetic fields.

Table 1 Requirements on the accuracy of magnetic field measurements

Environment	Range	Required accuracy
Earth's field and low Earth orbit	0–45,000 nT	∼0.1 to 1 nT
Magnetospheres	0–10,000 nT	∼0.05 to 0.2 nT
Planetary orbit/flyby		
Mercury	0–1,000 nT	∼0.05 to 1 nT
Venus	0–200 nT	
Moon	0–200 nT	
Mars	0–4,000 nT	
Jupiter	0–100,000 nT	
Saturn	0–20,000 nT	
Inner heliosphere	0–100 nT	∼0.05 to 0.1 nT
Outer heliosphere	0–30 nT	∼0.01 nT

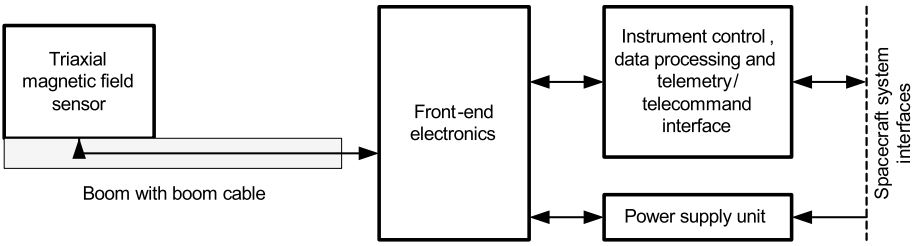

Fig. 2 Basic elements of a magnetometer. The sensor is usually mounted on a rigid, deployable boom to remove it from the close vicinity of the spacecraft and the magnetic background that it generates. The front-end electronics is specific to the sensor and its design has changed little over the past decades. The digital part of the instrument for control, onboard data processing and interfacing with the spacecraft telemetry and telecommand system is usually highly mission specific and has evolved significantly with the development of digital components and systems

These two types of magnetometer are known as DC instruments; their frequency response covers a range from (practically) 0 Hz to an upper limit which is usually in the few tens of Hz, determined by the response of the electronics. Their sensitivity decreases as a function of frequency; for the magnetic component of electromagnetic waves from ∼1 Hz to several kHz, search coil magnetometers are used. Although these instruments have been traditionally included in most recent planetary missions (see, e.g. Gurnett et al. 2004 for the Cassini mission and references therein), their scientific objectives are related to processes and phenomena in the planetary environment and are only indirectly related to the internal fields of the planets. In usual operation, these AC magnetic sensors are considered as antennas and their output is combined with electric field measurements for the characterization of electromagnetic waves in the neighbourhood of planets. These magnetometers will not be discussed in this paper.

As the magnetic field is a vector quantity, instruments have to measure three components, normally in an orthogonal coordinate frame. Both the fluxgate and the helium type magnetometers have a special arrangement to enable the three-axial operation, although by radically different designs. All magnetometers share a common basic functional block diagram, although there are considerable variations in the implementation. The common block diagram is shown in Fig. 2. The sensor and the front-end electronics are intimately linked

and although often separated by a significant physical distance (the length of the boom), they are closely tuned to operate specifically together. The sensor electronics is different for the two types of magnetometer, the outline of their operation is given below. In both cases, however, the analogue voltage or current signal that is proportional to the measured magnetic field is transformed into a digital signal for further processing and transmission through the telemetry to the ground.

The digital processing unit has evolved most drastically during the space age and is the most mission-specific part of the magnetometer. Its role is to execute onboard instrument control functions, such as setting the vector sampling rate and selecting the measurement range. It is also this unit that performs the interface functions with the spacecraft, such as sending the data to the spacecraft telemetry system and receiving and interpreting telecommands that provide the means remotely to control the experiment. The range of onboard digital functions that can be performed on the data has increased considerably with the increase in the performance of, and decrease in the resources needed by digital electronics. Among these functions are filtering, averaging, event-recognition, burst data storage and several more that can be included according to the mission requirement and available resources.

Both types of magnetometer sensors work at the null point, i.e. the ambient magnetic field measured by the sensor is used to generate a feedback of an equal and oppositely directed magnetic field around the sensor and it is the amount of feedback that is used as a measure of the ambient field. This ensures the greatest linearity in the measurements.

2.1 The Fluxgate Magnetometer

Fluxgate magnetometers are the most widely used sensors for space applications in general and for planetary missions in particular (see, e.g. Primdahl 1982; Acuña 2002; Musmann and Afanassiev 2010 and references therein). Several fluxgate magnetometers used on planetary missions are described in the following sections, from the early Mariner series to the most recent planetary magnetometers on missions to Mercury, Venus, Mars, Jupiter and Saturn.

The most frequently used fluxgate magnetometer in space applications uses ringcore sensors. Early on, a single ring core with two sets of sense winding (see below) was used for a two-axis sensor by Acuña and Pellerin (1969). This type of construction (two axes per core) was not generally taken up in subsequent designs; three separate single-axis sensors are normally used for the three components of the magnetic field. (This design has been used more recently by Carr et al. (2005) for a magnetospheric mission and is being used for the BepiColombo Mercury Orbiter mission by Glassmeier et al. (2010). Most currently used fluxgate sensors can trace back their origins to the early work on magnetic material for the cores of the sensors and their general construction to the sensors developed for the Apollo Lunar Magnetometer (Gordon and Brown 1972, also see Snare 1998 for a review of fluxgate magnetometers). As shown in Fig. 3, the fluxgate sensor has a ring-shaped high-permeability ferromagnetic core which has a toroidal drive winding around it. The sensor core and the drive winding are enclosed in a square coil former around which another, sense winding is placed. The two coils (drive and sense) are effectively orthogonal, so that the magnetic coupling between them is minimised, and is ideally zero. Bipolar, symmetric current pulses in the drive winding are used to drive the core material deep into saturation around the hysteresis loop, at a frequency usually about $f_o = 7$ to 15 kHz. A triaxial vector fluxgate magnetometer is constructed from an orthogonal arrangement of three single-axis sensors (Fig. 3, right).

In the absence of an external field, as shown in Fig. 4 (A), the sum of the magnetic flux in the two halves of the toroidal core sums to zero, due the symmetry of the hysteresis loop.

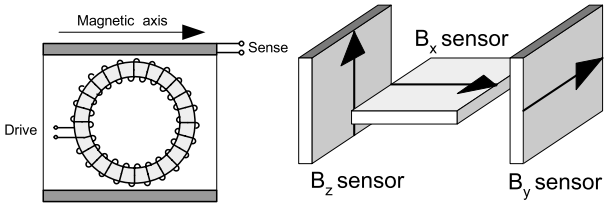

Fig. 3 (*Left*) Sketch of a single axis ring-core fluxgate sensor. The toroidal drive winding is around a ring consisting several turns of a very thin tape of high-permeability magnetic material (such as, for instance, molybdenum-pemalloy). The sense winding is around a rectangular coil former that defines the magnetic axis of the sensor. (*Right*) Arrangement of three single axis sensors to form an orthogonal triad for the measurement of the magnetic field vector. It is possible, by installing a second sense winding perpendicular to the first around one of the sensors, to use a single core for two orthogonal measurements

The signal in the sense winding, due to the magnetic induction law, is the time derivative of the magnetic flux and therefore in this case it is zero. However, in the presence of a non-zero component of an external magnetic field along the axis of the sense winding (case B), the hysteresis loop is slightly displaced, and the flux in the two halves of the core is no longer equal, so the sum of the flux generated in the two halves does no longer add to zero, and the variation of the flux induces a voltage signal as shown in Fig. 4. The voltage signal is the derivative of the periodically variable flux. This induced voltage signal in the sense winding has a frequency of twice the drive signal. This induced signal, of order <1 μV, is proportional to the component of the magnetic field along the axis of the sense winding. It is first amplified, then detected, using a synchronous detector. After some further amplification, the resultant voltage signal is fed back, through a transconductance (voltage-to-current) amplifier and the sense winding, as a feedback current counteracting the effect of the external field in the core. The schematic drawing of the electronics associated with a single-axis ringcore sensor is show in Fig. 5. As shown in the figure, the output signal is an analogue voltage proportional to the magnetic field component along the sensor axis. This signal is suitable for conversion to a digital number and further digital processing and transmission to the ground via the telemetry. The noise performance of fluxgate magnetometers depends on both the magnetic sensor itself (material and construction) and the front end electronics. A set of noise spectral density measurements is shown in Fig. 6.

In the fluxgate instruments described above, the feedback signal to null the field at the sensor was used at the level of the single-axis sensors: the feedback current was added to the pick-up coil to null the field along the axis of the sensor. It is generally recognised that, in high fields, there can be cross-talk between coils on the sensors and also uncompensated transverse fields that can adversely affect the vector measurements. A solution to improve the quality and accuracy of measurements in this case is to enclose the sensor triad inside a three-axis coil system so that the feedback is applied vectorially to the sensors. An elegant solution for minimising the size of the external, vector-feedback coil system was proposed by Primdahl and Jensen (1982) and used on Earth-orbiting missions as described below in Sect. 3.4 (Nielsen et al. 1995). A vector feedback arrangement, using a three-axis Helmholtz-type coil system is also used in the BepiColombo magnetometer intended for Mercury described below in Sect. 3.1 (Glassmeier et al. 2010).

In more recent fluxgate magnetometers, the analogue electronics has been replaced by a digital version. The digital magnetometer presents many advantages; for the measurements of magnetic fields, it provides a significantly greater flexibility in the sensor control and its feedback loop (Auster et al. 1995; Magnes et al. 2003, 2008; O'Brien et al. 2007).

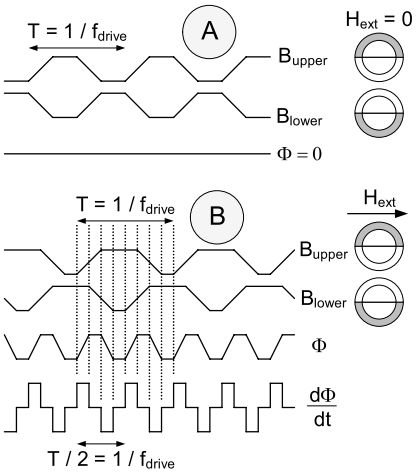

Fig. 4 Simplified principle of the operation of a fluxgate magnetic sensor. *Panel (A)* shows the magnetic flux generated in the two halves of the ringcore magnetic material by the drive current waveform in the absence of an external field. The total flux is zero (the flux generated in the two halves cancel each other). In the presence of an external field, *panel (B)*, the magnetising field due to the drive current waveform is added to the external field in one half of the ringcore and is subtracted from it in the other half. This creates a flux imbalance (there is no cancellation between the two half rings) that has a period half that of the drive waveform. The derivative of the flux signal induces a voltage in the sense coil that surrounds the ringcore

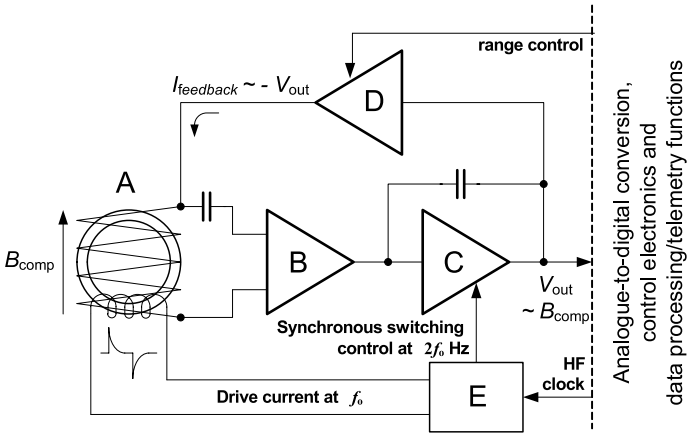

Fig. 5 A single axis fluxgate magnetometer sensor with its associated front end analogue electronics. (*A*) ringcore sensor with drive and sense/feedback windings, (*B*) pre-amplifier, (*C*) integrator with phase synchronous detector at twice the drive waveform frequency, (*D*) feedback transconductance (voltage-to-current converter) amplifier, (*E*) drive current waveform generator. In this configuration, the measurement range of the sensor is controlled through the gain of the transconductance amplifier. Normally three such units make up a complete magnetometer, with the sensors arranged in an orthogonal triad configuration as illustrated in Fig. 3

In the earlier versions of the digital magnetometer, an analogue-to-digital converter was used to transform the sensor output directly into a digitally sampled form so that filtering and phase-sensitive detection can be performed in a dedicated digital device in which the

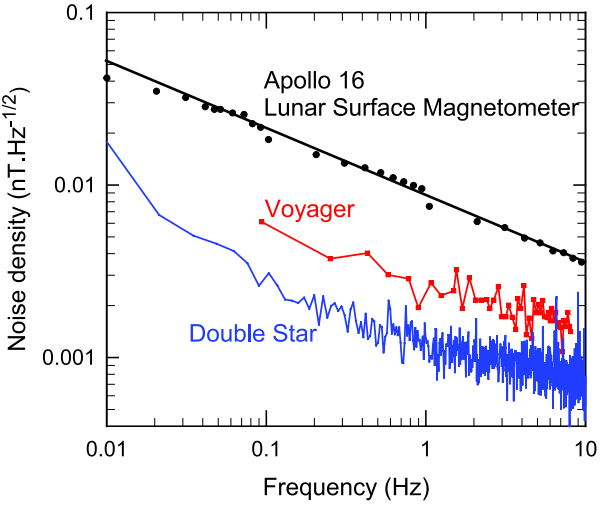

Fig. 6 The noise density of fluxgate magnetometers as a function of frequency. The three instruments illustrated span about 40 years of development. All three use ringcore sensors of very similar dimensions and the same magnetic material, although they are of different construction details. The front-end electronics designs are based on the same schematic but use increasingly better, lower noise amplifiers and other components. Much of the order-of-magnitude improvement in noise performance is attributed to the evolution of the electronics associated with the sensors (after Dyal and Gordon 1973; Behannon et al. 1977; Carr et al. 2005)

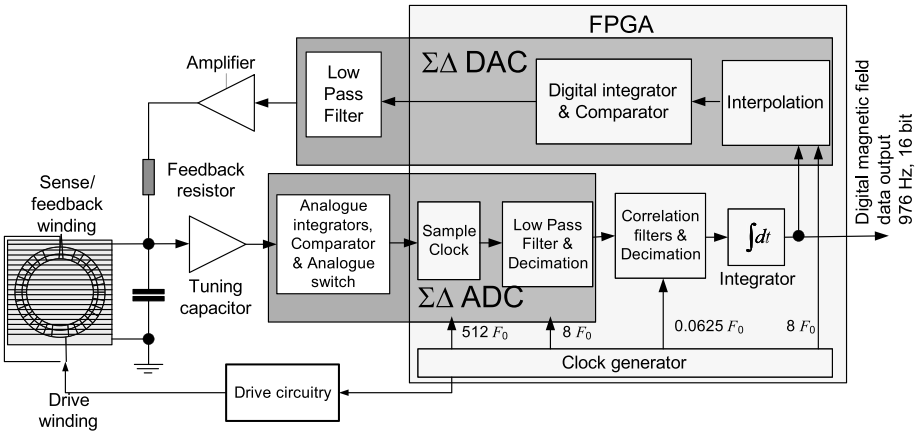

Fig. 7 A schematic diagram of the digital magnetometer, using a second-order sigma-delta modulator instead of the more classical Analogue-to-Digital Converter design (after O'Brien et al. 2007)

field-proportional signal is already in digital form. The same device then also controls the feedback to the sensor through a digital-to-analogue converter. The gain of this design is primarily in the resources needed for the instrument; the noise level of the magnetometer remains limited by the sensor performance.

The more recent version of the digital magnetometer is illustrated in Fig. 7. This design uses a sigma-delta single bit modulator both for digitising the sensor signal and to provide

the feedback to the sensor as illustrated in Fig. 7. One of the main motivations for this design is the ability to implement the electronics of the sensor with components that can tolerate the very high doses of radiation that will be experienced in planned Jupiter missions.

2.2 The Vector and Scalar Helium Magnetometers

A class of magnetometers used on space missions since the 1960s has applied the effect of magnetic fields on the magnetic state of atoms for measuring with high precision and accuracy either the magnitude of magnetic fields (scalar magnetometers) or their three components (vector magnetometers). In general, magnetometers using Nuclear Magnetic Resonance (NMR) or Electron Spin Resonance (ESR) are used to measure the scalar value of magnetic fields, in particular the Earth's field in ground-based geomagnetic observatories. The operation of such resonance magnetometers were generally described by Hartmann (1972). A few such magnetometers have been used in space in conjunction with vector magnetometers to provide high accuracy measurements of the Earth's magnetic field (Primdahl 1998). The helium magnetometer described below can in fact also be configured to operate in a scalar mode that provides a high accuracy measurement of the magnitude of the magnetic field (Slocum and Reilly 1963; Slocum et al. 1971). A helium magnetometer operating in the scalar mode was included in the Cassini Saturn Orbiter magnetometer (Smith et al. 2001).

However, it is also possible to build a quantum-effect based magnetometer in a tri-axial vector-measuring configuration. A particularly successful three-axis (vector) magnetometer based on the quantum-mechanical properties of helium has been used on several key planetary and space missions, such as Mariner 4 and 5 (launched in 1964, Connor 1968; Smith 1969), Pioneer 10 and 11 (launched in 1972 and 1973, Smith et al. 1975a, 1975b), ISEE-3 (launched in 1978, Frandsen et al. 1978), Ulysses (launched in 1990, Balogh et al. 1992a, 1992b) and Cassini-Huygens (launched in 1997, Smith et al. 2001; Dougherty et al. 2004). The basic principle of the helium magnetometer is that in the presence of an external magnetic field the efficiency of optical pumping in a cell containing He is reduced and this reduction can be related quite accurately to determine the components and/or the magnitude of the external field.

In optical pumping, a non-thermodynamic equilibrium distribution of atoms among the various energy substates is produced by incident polarised radiation. The relevant energy levels in ^{4}He are shown in Fig. 8. The circularly polarised light at 1.08 μm passing through the He cell induces optical pumping of the metastable He population in the triplet 2^3S_1 "ground" state (Colegrove and Franken 1960). The change in optical pumping efficiency depends on the intensity of the magnetic field and its angle with respect to the optical axis of the sensor. The polarization of the incident light is an important factor in the way the magnetometer operates and linear polarization has also been used in another implementation of the magnetometer. The general arrangement of a vector helium magnetometer that was flown on several planetary missions is shown in Fig. 9, illustrating the components of the sensor. When a rotating sweep field of ∼300 Hz is applied using the Helmholtz coil that surrounds the optical cell, the pumping efficiency, and therefore the IR throughput detected by the IR sensor vary as the vector sum of the sweep field and the component of the steady ambient field in the sweep plane. Under these conditions, the signal in the IR detector contains a sinusoidal component at the sweep frequency whose magnitude is proportional to the ambient field strength and whose phase relative to the sweep waveform depends on the direction of the ambient field in the sweep plane (see, e.g. Slocum and Reilly 1963 and Smith et al. 1975a). The pT-level performance of an early prototype helium magnetometer is illustrated in Fig. 10.

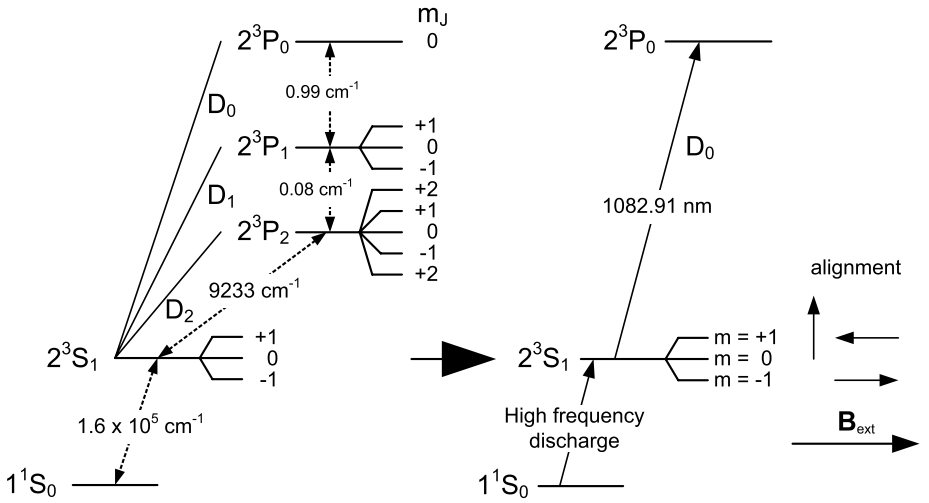

Fig. 8 The energy level diagram for helium used in the optically pumped helium magnetometer. Of particular interest are the 2^3S_1 terms that form a "ground" state for higher levels in optical pumping. *On the left of the figure*, all terms from the ground state to the first excited (^3P) are shown (Colegrove and Franken 1960). *On the right*, the key transitions used in the optically pumped magnetometer are shown, together with the alignment of the spit levels if the 2^3S_1 state in the presence of an external magnetic field

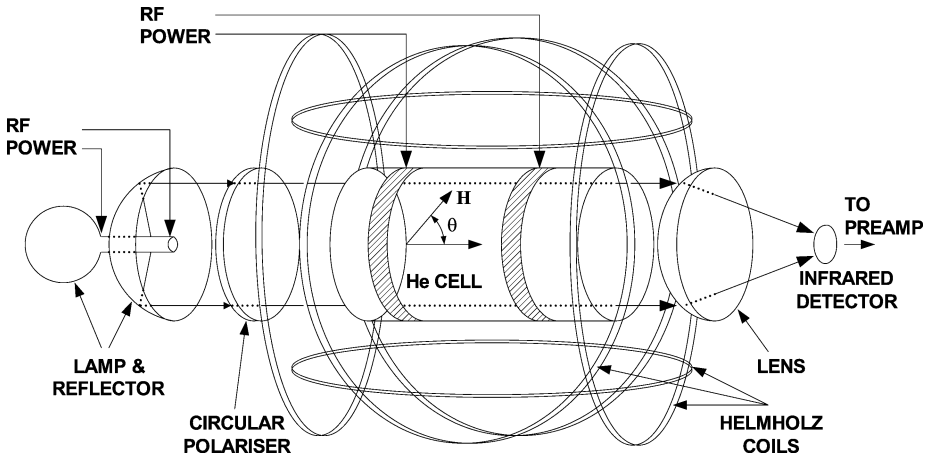

Fig. 9 Schematic diagram of the Vector Helium Magnetometer used on Pioneer 10, 11, ISEE-3, Ulysses and Cassini missions. For the Cassini Saturn Orbiter mission, the magnetometer has been configured to be used either as a scalar sensor (measuring the magnitude of the magnetic field) or as a vector magnetometer (figure courtesy of E.J. Smith)

Phase coherent detection of the output of the IR sensor in the magnetometer electronics produces voltages representing the ambient field components along the optical and transverse axes. These voltages are used to generate feedback currents in the sensor coils that null the ambient field on both axes. The feedback currents are highly linear measures of the two field components. Triaxial (vector) measurements are obtained by alternating the sweep field between two orthogonal planes that intersect along the optical axis. The performance of

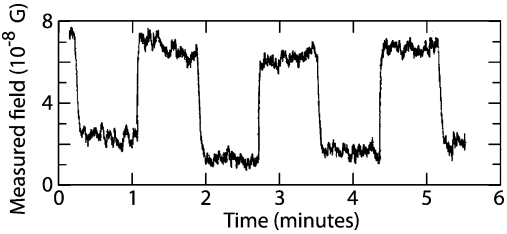

Fig. 10 The output of an early development model of the helium magnetometer demonstrating its excellent low-field sensitivity. A square calibration pulse of amplitude 5×10^{-8} G (or 5 pT) was applied along the sensor optical axis to the instrument contained in a magnetic shield (from Slocum 1972)

the VHM is characterised by its very stable offsets, with variations of no more than ∼20 pT over several years, and its very low noise, ∼3 pT rms/Hz$^{1/2}$; the best current fluxgates have an offset stability of only about 0.2 nT, although their noise performance has been improving (see Fig. 6) and is close to that of the VHM as used on recent missions.

More recent developments include the use of a laser instead of the He lamp used in the original design for providing optical pumping of the helium gas in the sensor cell (Slocum et al. 1988; Slocum 1991). As reported by Slocum (2002), the new design includes vector and scalar operation in the same instrument that can achieve accuracies of better than 1 part in 10,000 (better than ∼1 nT in the Earth's magnetic field) and a sensitivity of ∼0.2 pT/Hz$^{1/2}$. A parallel development of a new generation of helium magnetometers has been announced (Guttin et al. 1994; Gravrand et al. 2001) but no planetary mission has been found as yet for these instruments. (Such a magnetometer had been envisaged as part of the payload for NASA's Juno mission to Jupiter, but its implementation was later abandoned.) A particular advantage of this instrument is that it avoids, through the use of a controlled linear polarizer, the directional sensitivity of the circularly polarized design (Chaillout et al. 1993; Leger 1995). A scalar version of this magnetometer has been incorporated into the payload of the 3-spacecraft Swarm mission (see Sect. 3.4) that is planned for launch in 2012 and will study the Earth's magnetic field (Merayo et al. 2008).

2.3 Magnetic Background, Magnetic Cleanliness

A key characteristic of the performance of magnetometers in space is the magnetic environment at the location of the sensors. For space missions, the accuracy with which the ambient natural magnetic field due to the planet and its environment needs to be measured is between 0.01 to 1 nT, depending on the mission target. Even though spacecraft that have carried magnetometers in the past had been the subject of magnetic cleanliness programmes that enforced upper values of magnetic fields generated by subsystems and payload instruments, the outcome was a spacecraft-generated magnetic field that, on or close to the spacecraft, was significantly higher than the requirement by the magnetometer. This was partly or wholly resolved by placing the magnetometer sensor(s) on a boom that removed them from the vicinity of magnetic sources on the spacecraft (Mehlem 1978), thanks to the inverse cube law of the fall-off of magnetic field intensity as a function of distance from a dipole (and higher exponents for higher order poles). Boom lengths have varied from ∼1 m (Rosetta, Venus Express) to ∼5 m (Pioneer 10 and 11, Pioneer Venus Orbiter, Ulysses), to 12 m (Selene, JAXA's mission to the Moon) and to 13 m (Voyager 1 and 2). Although the use of booms is not by itself a complete solution to magnetic cleanliness, their length (determined from the technical and financial resources that are available) is generally a trade-off between

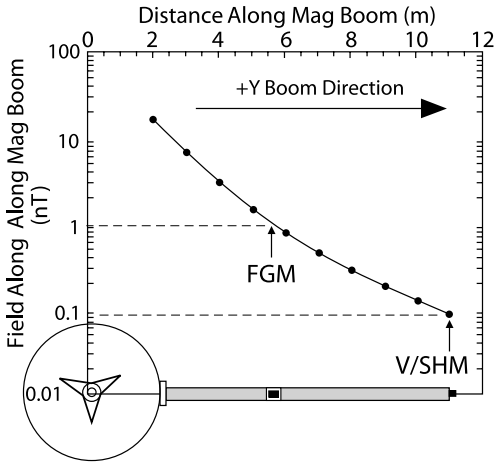

Fig. 11 Background magnetic fields measured (*full circles*) and modelled (*line*) along the magnetometer boom on the Cassini Saturn Orbiter spacecraft after implementing a strict magnetic cleanliness programme (from Narvaez 2004)

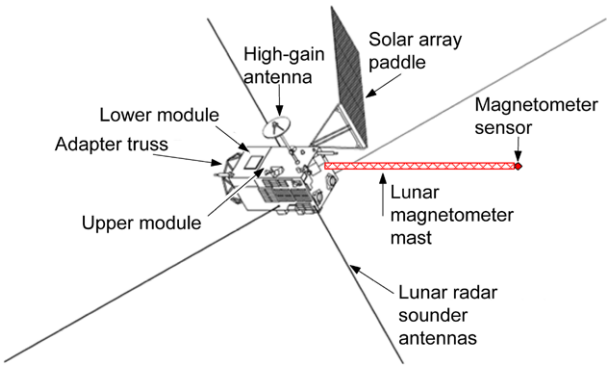

Fig. 12 The Kaguya (Selene) spacecraft of the Japanese JAXA/ISAS was launched in September 2007 to orbit the Moon and make very low altitude (∼50 km) observations, including the detailed mapping of the Moon's crustal magnetic field (drawing courtesy of JAXA/ISAS)

the cost of a strict magnetic cleanliness programme and a tolerable level of background at the location of the magnetometer sensor. Figure 1 in the Introduction illustrates the Pioneer 10/11 spacecraft with its 5 m boom and the vector helium sensor located at the boom tip; the fall-off of the spacecraft background field along the 11 m magnetometer boom, as the outcome of the magnetic cleanliness programme for the Cassini Saturn Orbiter spacecraft, is shown in Fig. 11. Such lengths are adequate when combined with a spacecraft-level test programme.

The much shorter booms used on Rosetta and Venus Express, for instance, and the absence in these cases of a significant magnetic cleanliness programme make the data processing and in-flight calibration challenging. This was already the case for Mars Global Surveyor (see the description of the magnetic background removal program in Sect. 3.3) and represents a general trend by space agencies not to accept the requirements of magnetic field investigations for an adequate cleanliness level at the location of the sensors. A remarkable recent exception to the general tendency of leaving the spacecraft background removal to the magnetic field experimenters is the Kaguya (Selene) spacecraft of JAXA/ISAS, with its 12 m magnetometer boom as illustrated in Fig. 12. The spacecraft, launched on 14 September 2007 was placed into an orbit around the Moon on 4 October 2007 and after a highly successful mission, it was crashed into the Moon on 10 June 2009. When the Kaguya boom was deployed in space, the magnetometer monitored the decrease in the background at its

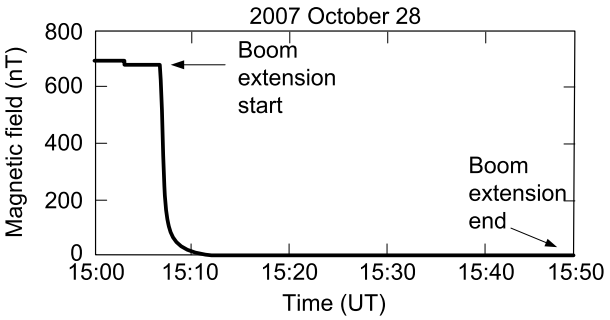

Fig. 13 Magnetic field measured by the boom-end magnetometer on JAXA's Kaguya lunar mission spacecraft as the 12-m boom was extended. The spacecraft background is effectively zero at the location of the magnetometer sensor (from Nazakawa et al. 2009)

location; the resulting data, as the spacecraft background turned to close to zero, are shown in Fig. 13.

The required magnetic cleanliness at the sensors on space missions to planets and their satellites is usually specified as an absolute value, for instance less than 1 nT in the ideal case, and an upper limit on the variability, such as 0.5 nT in 100 s. Such values are in practice difficult to achieve and compromises need to be made, in particular concerning the absolute value of the upper limit of the background. Meeting the stability requirement is in fact more important; a constant but known DC offset at the location of the sensor would be acceptable, but it is difficult to isolate from the varying component of the spacecraft background, and even from the sensor offset itself. The challenges of magnetic field measurements on spacecraft and the techniques used to deal with them have been described by, among others, Iufer (1970), Sanders et al. (1972), Ness et al. (1971), Davis et al. (1973), Neubauer and Schatten (1974), Musmann (1988), Auster et al. (1990) and Narvaez (2004). The topic has remained very active (see further description of the technique in Sect. 2.4). A recent example when a highly sophisticated use of the dual magnetometer (or gradiometer) technique that was applied to the magnetic field investigation on a magnetospheric spacecraft (TC-1 of the Double Star mission) was presented by Georgescu et al. (2008).

The preliminary steps to ensure a magnetically clean spacecraft consist in specifying and verifying by tests the magnetic state of individual components of the spacecraft: subsystem and payload boxes, moving parts and other mechanisms. A magnetic budget is usually drawn up and by using a digital model of the locations of the units and their magnetic characteristics, a magnetic model of the spacecraft can be derived. An early study of modelling and predicting spacecraft magnetic fields was published for NASA by Halacsi (1969). This model can be regarded, however, only as an estimate, as mathematical models can only be approximate, due principally to the complex self-compensation and mutual induction effects among the different units on the spacecraft. In some cases, where full testing was not possible, such as for the very important and successful Mars Global Surveyor (Acuña et al. 1996, see below), there was a special effort to implement self-compensation, in particular of the currents in the solar panels, followed by modelling with special care and in greater detail than usual, so that despite the unusual mounting of the sensors at the outboard ends of the solar panels (see Fig. 33 in Sect. 3.3), the background field could be, after added in-flight calibration, removed from the measurements. For several spacecraft with demanding mission objectives, a long magnetometer boom, a strict magnetic cleanliness program, and a pre-launch testing and modelling program were implemented to ensure the spacecraft's compatibility with the magnetic cleanliness requirements. An example is the Cassini Saturn Orbiter spacecraft, for which the challenge was to ensure the magnetic cleanliness of the Radioisotope Thermoelectric Generators (RTGs), potentially significant sources of background

contamination (Mehlem and Narvaez 1999). As shown in Fig. 11, the final pre-launch magnetic cleanliness of the Cassini spacecraft met the requirements of the mission, thanks in large part to the 11-m magnetometer boom (Narvaez 2004).

A difficult, but critically important aspect of magnetic cleanliness is the pre-flight testing of the magnetic properties of the spacecraft as a whole. For high-performance planetary missions, this testing is an important requirement. There are only very few facilities worldwide that are able to perform whole spacecraft magnetic testing. The Magnetfeldsimulationsanlage (MFSA, or "magnetic field simulation facility", see Kügler 2004), operated by the German industrial testing consortium IABG and situated near Ottobrunn, Germany and the Spacecraft Magnetic Test Facility (SMTF) of NASA's Goddard Space Flight Center in Maryland, USA are the two most used and most important such facilities.

The test facilities contain large three-axial coil systems with the purpose of compensating the Earth's magnetic field, its variations and fluctuations within a central volume so that a spacecraft placed in that volume is in close to zero magnetic field, as it would be in space. The three orthogonal axes each have four co-axial coils, circular Braunbek (1934) coils of 13 m diameter in the case of the NASA facility and square Helmholtz coils of 15 m for the European facility. The central, controlled volume has linear dimensions of about 2 m in the case of the SMTF and about 4 m in the case of the MFSA.

The recently refurbished capabilities of the MFSA are described in Kügler (2004) and a typical application to a spacecraft test is described by Kügler (2001). The controlled volume can simulate either a zero field environment or some other value that can be controlled by the currents in the coils. The stability is very good at $\sim$0.5 nT/hour in both facilities, even when the Earth's field varies—although testing becomes significantly more difficult during geomagnetic storms when the performance of the servo control of the coil currents performs less well. The reference to compensate the Earth's magnetic field is given by a high quality, high stability magnetometer at some distance from the facility, to avoid the reference signal to be affected by the coil currents.

A facility of more recent construction is the Japanese magnetic test facility of JAXA/ISAS in which the lunar spacecraft Kaguya (Selene) was tested (Shimizu et al. 2008). This facility also uses a Braunbek circular coil system of 15 m diameter. The volume of good uniformity, where the magnetic field can be maintained stably to an accuracy of $\pm$2.5 nT, is a 2.3 m diameter sphere centrally located in the coil system.

Two earlier, no longer active but historically important spacecraft-scale magnetic test facilities were located in California, USA. The first of these, at NASA Ames Research Center, Moffett Federal Airfield, was used in the early 1960s to test the early Mariner spacecraft (Mariners 2, 4 and 5), also the OGO (Orbiting Geophysical Observatory) series, and Pioneer 6 (Iufer 1970). It is interesting to note the typical values for the spacecraft fields obtained at the location of the magnetometers for these early missions, as quoted by Iufer (1970): Mariner 2 (130 nT), Mariner 4 (35 nT), Mariner 5 (12 nT), OGO (2 nT), Explorer 18 (0.5 nT), Pioneer 6 (0.25 nT). The second of these facilities, at TRW Inc., Redondo Beach, was used for the Pioneer 10 and 11 spacecraft (Sanders et al. 1972).

Magnetic cleanliness programmes and pre-launch testing are necessary for ensuring accurate measurements in space. However, the resources needed for pre-launch tests are not always available and, even for missions that have completed extensive pre-light magnetic tests, the evaluation of the spacecraft-induced background remains a routine part of in-flight calibration. In the following, specific missions and instruments are highlighted that have proved a challenge to remove the spacecraft background from the measurements. For many missions, two magnetometers, at different distances from the spacecraft body, have been used so that a gradiometrically calculated estimate of the background could be subtracted

from the observations (e.g. Ness et al. 1971); this is discussed further in the next section on magnetometer calibration. Specific cases are also described below. Neither an intensive magnetic cleanliness programme, nor extensive pre-launch testing has been carried out on some of the planetary missions described below: examples that are discussed in some detail are Mars Global Surveyor, the Rosetta cometary mission and Venus Express for which a reduced spacecraft-level magnetic cleanliness programme was carried out, in addition to very comprehensive instrument-level programmes. In the last two of these, only a short boom was used, with two magnetometers, while in the case of MGS, the magnetometers were mounted on the solar panels. Remarkably, however, significant discoveries have been made with both Venus Express and with MGS and, similarly, in-flight testing of the Rosetta magnetometer promises good results once the spacecraft reaches its target comet in 2014.

2.4 Magnetometer Calibration

The calibration of the magnetic field data measured by the instruments is one of the major challenges facing instrument designers and operators. Magnetometers in space or in planetary environments measure field component values over very wide dynamic ranges, with required accuracies (as shown in Table 1), up to five or six orders of magnitude smaller than the ambient magnetic field of the Earth in the laboratory. This necessitates that the calibration process be a conceptually two-step procedure, the first pre-launch, the second in-flight. In the following, a brief description is given of the main elements in the calibration process. The notation selected is not unique, as there are many different descriptions of the calibration techniques, but the principles listed are very general. (This description has been based on that found in Balogh et al. 2001; see also Gloag et al. 2010. An alternative, well documented description of a calibration programme for a terrestrial magnetism mission can be found in Risbo et al. 2003 and Olsen et al. 2003.) Specific references to the calibration of the data are also made in the description of instruments and missions throughout the paper.

The magnetic field to be measured is denoted $\mathbf{B}_{\text{actual}}$; this is a vector quantity and is defined in a physically meaningful coordinate system associated, for instance, with the target planet. The telemetered output of the magnetometer as received on the ground is denoted $\mathbf{V}$; this is also a vector quantity, i.e. an ordered set of three numbers. The relationship between $\mathbf{V}$ and $\mathbf{B}_{\text{actual}}$ can be described as a set of consecutive linear transformations in which the input is $\mathbf{B}_{\text{actual}}$ and the output is $\mathbf{V}$

$$\mathbf{V} = \underline{\underline{c}}^{(\text{sensor})}\,\underline{\underline{c}}^{(\text{transfer})}\,\underline{\underline{c}}^{(\text{att})}\mathbf{B}_{\text{actual}} + \mathbf{c}_0 \tag{1}$$

The transformation matrix $\underline{\underline{c}}^{(\text{att})}$ is simply the rotation of the vector from the physical (planetary) coordinate system into a coordinate system rigidly tied to the spacecraft. The transformation $\underline{\underline{c}}^{(\text{transfer})}$ represents the rotation from the rigid spacecraft coordinates into the coordinates tied to the sensor. This transformation can be included in $\underline{\underline{c}}^{(\text{att})}$ if the sensor is mounted rigidly so that its reference coordinate system is strictly tied to the spacecraft and its attitude determination system, within the limits of the required error budget (∼6 arcmin for many space physics missions). In many early planetary missions this was assumed, as the rigidity of the sensor mounts, often on a rigid boom, was ensured and fully tested before flight. In that case, $\underline{\underline{c}}^{(\text{att})}$ is a set of two consecutive rotations, one from the physical frame into the frame in which the spacecraft attitude is defined and measured and one that transforms from that frame into the frame of the magnetometer sensor mounting. However, when the booms are not sufficiently rigid and the reproducibility of the deployment (as is normally the

case) does not by itself meet the requirements on the knowledge of the angular alignment of the sensor mounting, other measures need to be implemented to determine $\underline{\underline{c}}^{(\text{transfer})}$.

Three different methods have been used for a precise determination of $\underline{\underline{c}}^{(\text{transfer})}$ on planetary missions. The Voyager and Galileo spacecraft, described in Sect. 4.1, used a single calibrated coil at the boom root, referenced rigidly to the spacecraft, that when energised by a calibrated DC current, produced a well-defined and precise magnetic field vector at the location of the magnetometer sensors. The Kaguya lunar spacecraft (described in Sect. 3.5) and the Cassini Saturn orbiter spacecraft (described in Sect. 4.2) used two orthogonal coils mounted on the spacecraft which generated known magnetic field vectors that have been used to determine the precise orientation of the sensors with respect to the spacecraft. Another method, using an optical Attitude Transfer System between the spacecraft body and the magnetometer platform was used on the Magsat mission, as described in Sect. 3.4 (Mobley et al. 1980). In addition, star cameras were used on the spacecraft for determining the attitude of the spacecraft accurately. For terrestrial magnetic field measurements, the accuracy requirement is normally greater than for planetary and space physics missions; it is of order 1 part in 10^5, to reach the required sub-nT accuracy in the earth's magnetic field. For Ørsted and subsequent missions (see also in Sect. 3.4) with the objective to measure accurately the Earth's magnetic field, an Advanced Stellar Compass (ASC) was developed that enabled the absolute attitude of the magnetometer sensor itself to be determined (Jørgensen et al. 1997). By mounting the magnetometer sensor and the ASC on a common optical bench, the absolute determination of the magnetometer attitude no longer relied on the spacecraft attitude measurement, but could be taken directly from the attitude determined by the star camera.

The matrix $\underline{\underline{c}}^{(\text{sensor})}$ represents the properties of the sensor and magnetometer electronics, as determined by pre-launch calibration procedures. It includes the linear scale factors in units of voltage or counts at the output of the instrument per units of the magnetic field component (in nT) measured for each axis. It also includes the rotation from the assumed orthogonal axes defined for the sensor and the (generally nearly, but not strictly orthogonal) magnetic axes of the vector sensor.

The vector $\mathbf{c}_0$ added in (1) results from the offset of the sensor itself and of the sum of the background contributions due to the spacecraft.

Calibration of the received data usually proceeds in consecutive steps, to determine the measured field vector $\mathbf{B}_\text{S}$ in the orthogonal coordinate system tied to the sensor, by performing first a transformation (using a diagonal matrix $\underline{\underline{M}}$ with nominal scale factors) from telemetered values to values of the components in physical units (nT), followed by the application of the calibration matrix $\underline{\underline{c}}^{\text{cal}}$ which incorporates all the scale factor corrections as well as the orthogonalisation of the axes from the magnetic measurement coordinate system to the sensor coordinate system;

$$\mathbf{B}_\text{S} = \underline{\underline{c}}^{\text{cal}}\,\underline{\underline{M}}\,\mathbf{V} - \mathbf{o}^{\text{cal}} \tag{2}$$

The vector $\mathbf{o}^{\text{cal}}$ represents the total offset determined usually in flight; it includes contributions by the sensor and from all external sources. The determination of $\underline{\underline{c}}^{\text{cal}}$ and $\mathbf{o}^{\text{cal}}$ is always a major component of the scientific operation of a magnetometer on a planetary (or other) spacecraft. Pre-launch calibration tests at sensor level (see, e.g. Risbo et al. 2003) cover measurements of the scale factors and their linearity; the frequency response (including the electronics and any digital filtering or other manipulation); the noise of the sensor and electronics as a function of temperature; the sensor offset vector and its stability vs. time and

temperature; the orthogonality of the triaxial sensor; and finally any crosstalk between axes of the sensor (very important for sensors in large fields close to planets and in Earth orbit, cf. Brauer et al. 1997). The parameters thus determined are used as a baseline for the determination of the calibration parameters in flight. Generally speaking, all the parameters in the calibration matrix $\underline{\underline{c}}^{\mathrm{cal}}$ should be considered as time dependent, and the calibration effort needs to be continued throughout the flight operations phase of the instruments.

The determination of the compound offset vector $\mathbf{o}^{\mathrm{cal}}$ remains similarly a continuous task. The reason for this is that the sensor offset, particularly for fluxgate sensors, is variable in time as well as in temperature. In the descriptions of specific instruments in this paper, factors affecting the sensor offset and that due to the spacecraft background are outlined in several instances. For the determination of the offsets, a distinction needs to be made between spinning and three-axis stabilised spacecraft. While most planetary missions use three-axis stabilisation to satisfy the requirements of imaging investigations, a few (e.g. Pioneer 10 and 11) were spin stabilised. In the case of spinning spacecraft, the offsets in the spin plane can be determined relatively easily, as two components of the magnetic field (if one of the axes of the sensor is aligned with the spin-axis) are modulated by the spin and should, for complete spins, average to zero. A departure from the zero average corresponds to the offset for the given axis. As the alignment of the sensor magnetic axes and even its coordinate system in the spacecraft coordinate system aligned with the spin-axis is never perfect, this provides only a partial determination of the zero levels even of the two axes in the spin plane.

Procedures have been developed for the determination of magnetometer offsets relying on the statistical properties of the magnetic field in the solar wind (Davis and Smith 1968; Belcher 1973; Hedgecock 1975). Most changes in the interplanetary magnetic field are changes in direction rather than in magnitude. The method proposed by Davis and Smith (1968) uses this property and minimizes the variance of the squared magnitude of the magnetic field over a suitabl interval to determine the offsets. Belcher (1973) proposed a variant of the Davis and Smith method. As it became known that there are many intervals in the solar wind when the fluctuations are primarily transverse (Alfvénic), Belcher (1973) proposed that the component offsets could be determined by maximising the maximum variance vector to be perpendicular to the average magnetic field. The method proposed by Hedgecock (1975) implemented the fluctuating property of the interplanetary magnetic field to determine the offsets by imposing that the correlation between changes in the inclination of the magnetic field to the coordinate axes and the magnitude of the vector field should be a minimum over a suitably chosen data interval. These methods have been widely used over the past 40 years. As an example, Fig. 14 shows the long term behaviour of the zero level offsets of the Vector Helium Magnetometer on the Ulysses mission (Balogh et al. 1992a, 1992b). The offsets were determined by taking advantage of the spacecraft spin as well as the application of the Hedgecock (1975) method. The extremely high long term stability of the VHM sensor is well illustrated; the systematic variations were due to the spacecraft warming up as it approached perihelion in 1995 and 2001. More recently, Leinweber et al. (2008) have revisited these three methods and have concluded that a suitably modified variant of the Davis and Smith (1968) method is the best for determining magnetometer zero levels.

Terrestrial missions for measuring the magnetic field of the Earth (as described in detail below, in Sect. 3.4) have used the vector measurement of the field in combination with a scalar measurement of its magnitude (Merayo et al. 2000). Given that the scalar magnetometer provides an absolute measurement of the magnetic field magnitude, the methodology proposed by Merayo et al. (2000) allows the determination of nine parameters for calibrating the vector measurements of a tri-axial fluxgate sensor. These are the three zero

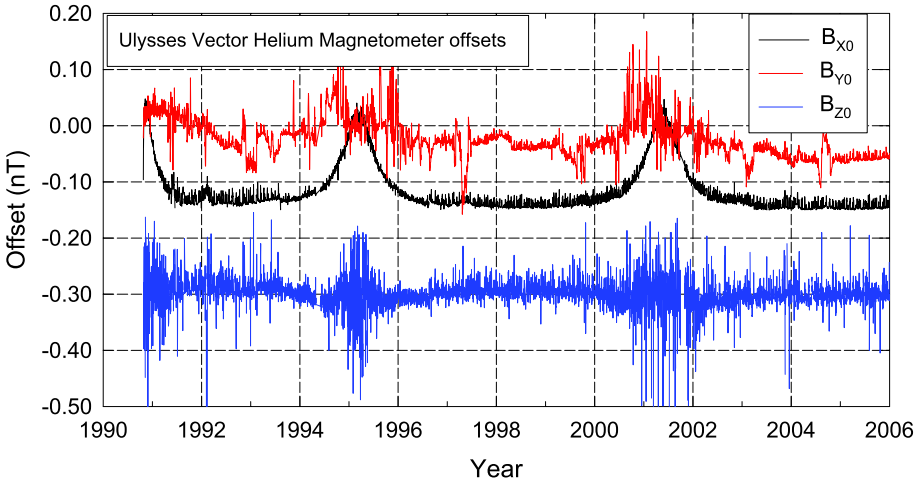

Fig. 14 The zero level offsets of the Vector Helium Magnetometer on the Ulysses spacecraft determined over the first 15 years of its operation in flight using the technique first proposed by Hedgecock (1975). The very high long tern stability of the offset is well illustrated, with a small sensitivity to temperature (notable in 1995 and 2001) as the spacecraft went through perihelion in its nearly polar orbit around the Sun

level offsets on the three axes, three scale factors and three angles that define the misalignment of the sensor axes from an orthogonal reference system. As the resources needed by scalar magnetometers are generally significant, the only planetary mission so far that has used a similar configuration is the Cassini Saturn Orbiter (see Sect. 4.2) that used a triaxial vector fluxgate, together with a vector/scalar helium sensor (Smith et al. 2001; Dougherty et al. 2004). A potential alternative to the use of a scalar magnetometer is an independent measurement of the magnetic field magnitude. This was done on ESA's Cluster spacecraft (not a planetary mission as such) by an electron gun instrument that measured the gyroradius of electrons of calibrated energy and thus the magnetic field strength. The intercalibration with the fluxgate vector magnetometer on the same spacecraft has been investigated by Georgescu et al. (2006).

The determination of the background field at the location of the magnetometer sensor due to the spacecraft is an important part of the in-flight calibration of the magnetic field data. The topic of magnetic cleanliness has been described above, in Sect. 2.3. In the following sections, several further mentions are made to the dual magnetometer technique, whereby two sensors are used along a boom at different distances to use gradiometry for deducing the spacecraft field. Early application of the technique proposed by Ness et al. (1971) was made on the Mariner 10 spacecraft as discussed in Sect. 3.1. However, the technique needs to be used with some care, as was pointed out by Davis et al. (1973), Neubauer and Schatten (1974), Neubauer (1975) also examined the fall-off of the spacecraft signature with distance that's highly relevant to the application of the method. Further use of the technique was made on the Voyager mission (see Sect. 4.1). The gradiometer technique has had to be brought up to date in recent years as the precautions for minimising the spacecraft fields (the magnetic cleanliness programmes described in Sect. 2.3) have not been fully carried out on some of the missions like Rosetta and Venus Express. For these, the gradiometer technique was the only tool that allowed the recovery of a clean magnetic field signal from the measurements (Delva et al. 2003; Pope et al. 2009). Important, if unintended experience was gained in the application of the technique to the Double Star TC-1 mission (Georgescu et al. 2006).

Use of the gradiometer technique for terrestrial missions in which use is made of a scalar magnetometer in combination with a vector sensor was examined by Primdahl et al. (2006). Using the example of Ørsted (see Sect. 3.4), they developed a procedure for assessing the spacecraft field at the location of the triaxial fluxgate sensor, using the measurements of the magnitude of the field at the end of the boom by a scalar sensor. However, their results showed one particular potential limitation of the technique. This is due, as concluded by Primdahl et al. (2006) to an unknown shift in the offset values of the magnetometer itself that is caused by the launch stresses. Because of this, the pre-fight determination of the sensor offset cannot be used in the gradiometer equations, at least not without some considerable uncertainty.

3 The Terrestrial Planets

The four terrestrial planets, Mercury, Venus, the Earth and Mars, together with the Moon are solid bodies, composed of a mostly iron core and a silicate mantle (Stevenson et al. 1983). Their magnetic properties, despite the similarities of their constitution, are very different. Apart from the Earth which has a very well documented magnetic field and magnetic environment, the other three (plus the Moon) are less well known, but their main magnetic field (if any) has been observed and modelled. Historically, the earliest planetary missions explored Venus and Mars; this was somewhat unfortunate, since, as we now know, Venus appears not to possess a global magnetic field at all and Mars' is a complex remnant crustal field confined to a part of the planet. Mercury provided the greatest surprise by having a small but very interesting planetary scale magnetic field. The moon has no large scale magnetic field but its local concentrations of magnetized material have interesting implications for its history.

3.1 Mercury

The small planet Mercury, the terrestrial planet closest to the Sun, was not considered to have a planetary dynamo and was assumed to be Moon-like. The reason for this assumption was that, given the size of Mercury, its interior would have cooled and frozen rapidly after its formation, not allowing a dynamo to start and operate. Even Mercury's known, very high density that implied a large iron core was considered an inadequate argument for any part of Mercury's core to remain liquid to allow a dynamo to operate. Given this consensus about Mercury's likely internal state, it is very surprising that a magnetometer was included in the payload of Mariner 10, the mission known as Mariner Venus/Mercury 73 prior to its launch in 1973. However, the magnetic field measurements, demonstrating the existence of a global planetary field, led to a fundamental re-assessment of the planet's thermal evolution and the current state of its interior (Ness 1978).

The magnetometer on Mariner 10 consisted of two triaxial sensors, one at the end of a 5.8 m boom, the other at 2.3 m inboard from the boom tip (Ness et al. 1974, 1975). The sensors were built by Schonstedt Instrument Company, manufacturers of several of the early space-borne magnetometers. The performance of the sensors enabled the measurement of the unexpected magnetic field and magnetosphere of Mercury during the two flybys close to the planet, on 29 March 1974 and 16 March 1975. A sketch of one of the two triaxial fluxgate sensor units is shown in Fig. 15.

This was the first time that a dual magnetometer system was used to measure the magnetic field of a planet (not counting the Mariner 10 flyby of Venus), and it is of interest to note the method used to subtract the disturbance magnetic field generated by the spacecraft

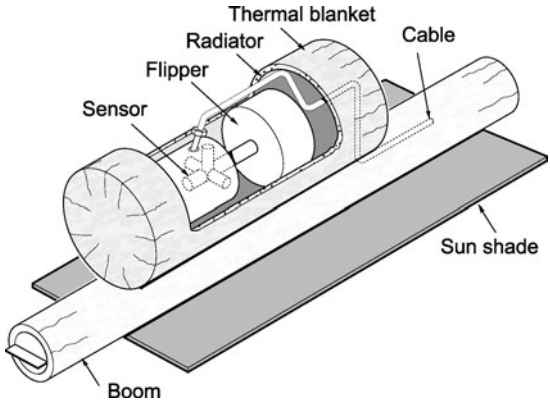

Fig. 15 A cutaway sketch of one of the two Mariner 10 triaxial sensor units, showing the flipper assembly next to the three orthogonal single axis Schonstedt fluxgate sensors (redrawn by N. Powell after http://nssdc.gsfc.nasa.gov/nmc/experimentDisplay.do?id=1973-085A-04). The mass of the two magnetometer instruments including the analogue electronics was 4.3 kg and its average power consumption was 13.6 W. The instrument had a data rate of 1052 bps. The complete instrument was designed at the Goddard Space Flight Center

from the measurements. Following the description of the post-launch calibration of the data by Ness et al. (1974), the first step was to calculate the vector contribution of the spacecraft $\mathbf{B}_{SC}$ at the location of the outboard sensor by combining the measurements at the inboard and outboard sensors through $\mathbf{B}_{SC} = \alpha/(1-\alpha)[\mathbf{B}_{IB} - \mathbf{B}_{OB}]$ where $\alpha = 0.3$ is a coupling coefficient between the sensors assuming a spacecraft-centred dipole (calculated from the distances along the boom and adding the distance of the boom root from the spacecraft centre); $\mathbf{B}_{IB}$ and $\mathbf{B}_{OB}$ are the raw measurements at the inboard and outboard sensors, respectively. It was found that at the location of the sensors the dipole assumption for the spacecraft background was adequate, although the strength and orientation of the dipole was variable. The spacecraft background field $\mathbf{B}_{SC}$ is then averaged over 3 seconds and then a corrected vector $\mathbf{B}_{OBC}$ is calculated by subtracting from each measurement sample the averaged value of the spacecraft-generated background $\mathbf{B}_{OBC} = \mathbf{B}_{OB} - \langle \mathbf{B}_{SC} \rangle$. The sampling rate for the outboard sensor was 25 vectors/s; for the inboard sensors three such vectors sampled at 40 ms intervals were averaged to give a time resolution of 120 ms. The magnetometer offset was determined from the pre-flight calibration tests and from in-flight assessments using the periods when the spacecraft was rolled and also when the flipper that exchanged mechanically the sensor axes was activated. The accuracy of the measurements following the correction for the spacecraft background and its variable component (due, among other causes, to the operation of the scan platform on which the dual television cameras were mounted) was assessed to be ± 1 nT.

This accuracy was more than sufficient for the results from two flybys of Mercury to provide the intriguing but remarkable result that there was a strong likelihood for the existence of a global, planetary scale dynamo in Mercury's interior. As detailed by Connerney and Ness (1988) in their definitive analysis of the Mariner 10 data, the limitation on describing the planetary field arose from the limited set of observations from the two flyby trajectories, rather than the magnetometer, its performance and any spacecraft generated backgrounds. The time between the first and last bow shock crossings was 33 minutes on the first flyby on 29 March 1974 and 27 minutes on the third flyby on 16 March 1975. The intervals spent between magnetopause crossings in and out of Mercury's magnetosphere was even

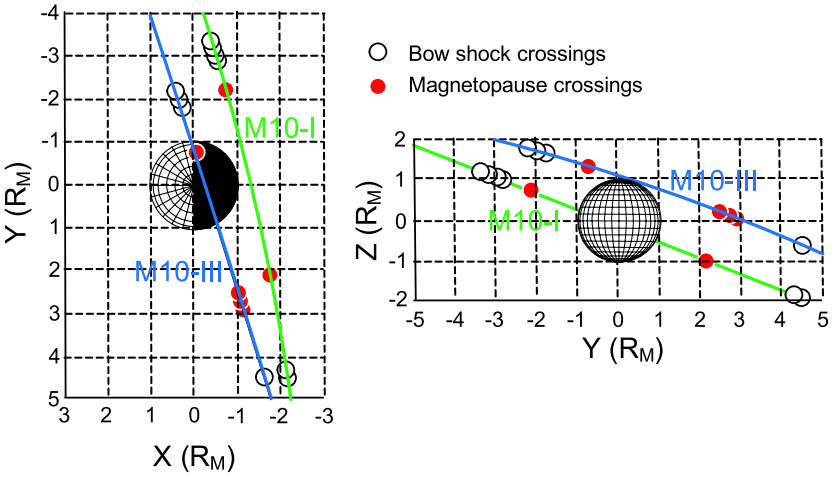

Fig. 16 Flyby trajectories of the Mariner 10 spacecraft at Mercury in 1974 (M10-I) and 1975 (M10-III), with indications of the locations of the bow shock and magnetopause crossings. *The diagram on the left* is the view from above the north pole of Mercury, with the Sun on the left, *the diagram on the right* is the view of the planet and the paths of the spacecraft seen from the direction of the Sun

shorter, 18 minutes on the first flyby and 13 minutes on the third flyby, giving a total of 31 minutes of data that were associated directly with the planetary field. The flyby trajectories are shown in Fig. 16, indicating the limited spatial coverage. The magnitude of the magnetic field during the two close flybys is shown in Fig. 17. The analysis of the data, despite the limited data sets, showed (Connerney and Ness 1988) that the equivalent equatorial dipole field was between about 200 and 350 nT. This range of figures was confirmed by modelling the magnetosphere of Mercury, based on the boundary crossings observed by Mariner 10. The problem of identifying and quantifying the planetary field against the background of the fields of external origin, due to the interaction with the solar wind was widely recognised and addressed using different models and assumptions concerning the details of the interaction. This problem, however, could not be resolved using the Mariner 10 data; the resolution will come from the next generation of missions to Mercury, MESSENGER, soon to be in orbit around the planet and the two-spacecraft Bepi-Colombo mission that will explore Mercury towards the end of the next decade.

The MESSENGER spacecraft has already provided, during its two flybys of Mercury in January and October 2008, ample confirmation of the global magnetic field of the planet and the very likely existence of a dynamo operating in the planet's interior (Anderson et al. 2008, 2009; Slavin et al. 2009). MESSENGER, only the second space mission to reach Mercury, will be the first to orbit around the planet. Launched on 3 August 2004, the spacecraft needed an Earth flyby a year after launch, followed by two Venus flybys on 24 October 2006 and 5 June 2007, and then three flybys of Mercury. All three flybys have already been successfully completed on 14 January, 6 October 2008 and 29 September 2009. The spacecraft will be finally injected into an eccentric orbit on 18 March 2011. Mercury is deep in the gravitational well of the Sun and a large amount of (breaking) energy is required to place a spacecraft in orbit around it; the use of planetary flybys is a cost-effective solution to the problem, at the cost of a very long transfer time from Earth to the planet (McAdams 2003).

The trajectories of the two first flybys were similar, as shown in Fig. 18. (The third flyby had also a very similar geometry, but the results have not been published before this paper

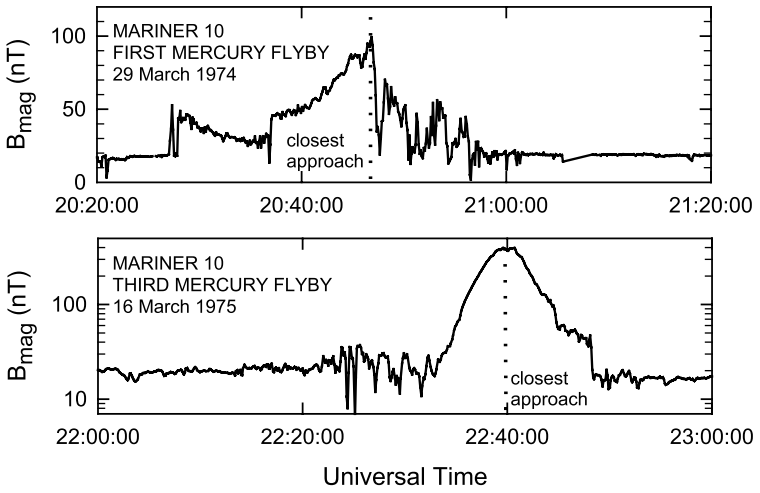

Fig. 17 The magnitude of the magnetic field measured by Mariner 10 on the two close flybys of Mercury in 1974 and 1975. Note the different profiles of the field on the two flybys. The first flyby was marked by a sudden collapse of the field followed by a highly disturbed interval that has been attributed to a major reconfiguration of the magnetosphere possibly caused by a Hermean version of a substorm. *In the lower panel*, the dominant global dipole term is evident; note that the field magnitude for this flyby has been plotted on a logarithmic scale to follow the representation originally published by Ness et al. (1976a, 1976b)

was completed.) Both were in a plane close to the equator and, although the closest approach was, in both cases, at a height of 200 km over the planet's surface, the maximum magnetic field measured was about 160 nT, less than the maximum field (about 400 nT) measured by Mariner 10 on the third flyby at a closest approach distance of 327 km, but at high latitude as shown in Fig. 16. The magnetic field magnitude measured during the two flybys by MESSENGER as shown in Fig. 19; the differences are due mainly to the different dynamic state of the magnetosphere at the two epochs (after Anderson et al. 2008 and Slavin et al. 2009). The two flybys differed by their relative phasing in Mercury longitude that allowed different regions of the surface to be imaged further to complement the earlier Mariner 10 coverage. The successful third flyby that took place on 29 September 2009 was also in Mercury's equatorial plane, at an altitude, at closest approach, of 231 km, although the data coverage was interrupted because the spacecraft was automatically switched into its safe operating mode. Mercury orbit insertion will take place between 18 and 21 March 2011 into a high inclination ($\sim$80°) eccentric orbit with a period of 12 hours, a perihem height of 199 km at latitude $\sim$60°N and an apoherm at a maximum distance of $\sim$15,200 km from the planet's surface. The dynamo hypothesis for the origin of Mercury's magnetic field, already favoured after Mariner 10, has been considerably strengthened by the consistent observations during the first two MESSENGER flybys (Anderson et al. 2009) as the analysis of the data confirms that the value of a pure dipole would be $\sim$250 nT R_M^3, but with an apparently weaker value near the equator (matching in magnitude the equally equatorial measurement by Mariner 10 on its first flyby) which implies the influence of higher order moments and/or magnetospheric (tail) currents that are stronger or closer than expected. The equatorial surface field has been confirmed to be in the range 250 to 290 nT, roughly about mid-range of the earlier Mariner 10 estimates. Further refinement will now come from the one year long orbiting phase of MESSENGER in 2011–2012.

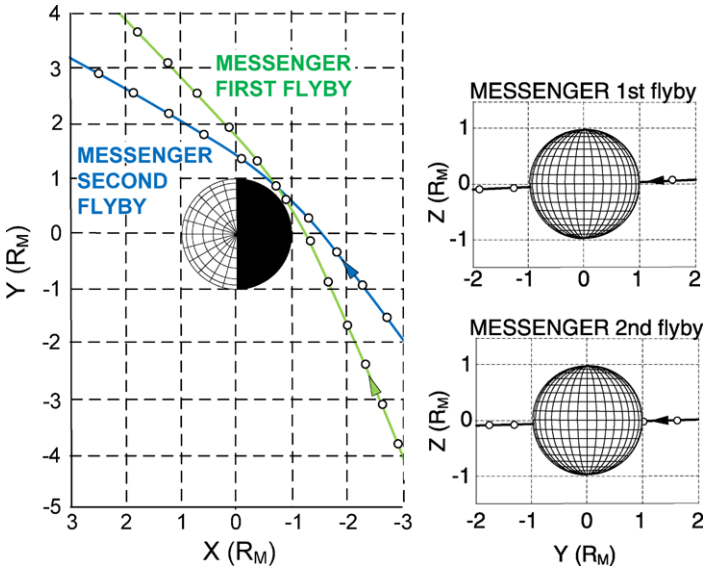

Fig. 18 The geometries of the first two flybys of Mercury by MESSENGER on 14 January and 6 October 2008. Both flyby trajectories were close to Mercury's equatorial plane at a closes approach altitude of 200 km s. *On the left*, the trajectories are shown in Mercury's equatorial plane with the X axis pointing toward the Sun. *On the right*, the view is from the Sun in the plane perpendicular to the equatorial plane. The markers on the flyby trajectory paths indicate 5 minute intervals. The third flyby on 29 September 2009 is to have a similar geometry, at an altitude of 228 km

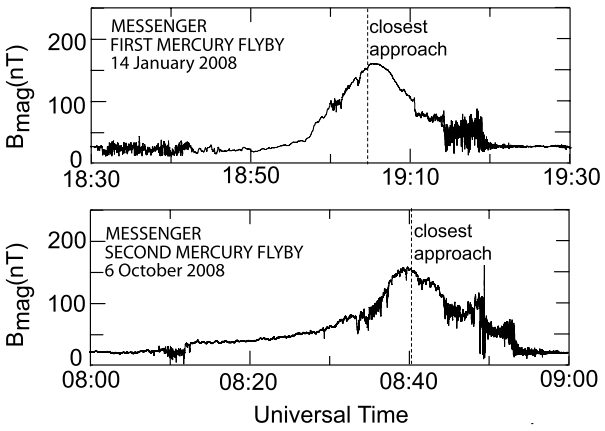

Fig. 19 The magnitude of the magnetic field measured by MESSENGER on its first two flybys of Mercury. The dominant dipole component of the internally generated field is evident, as is the strong variability introduced by the externally generated currents in Mercury's magnetosphere. After (*top panel*) Anderson et al. (2008), and (*lower panel*) Slavin et al. (2009)

The resolution of the details of Mercury's magnetic field between internal and external effects will remain a difficult task with a single-spacecraft mission, because of the very dynamic nature of the magnetosphere (see reviews and assessments by Russell et al. 1988; Slavin 2004; Scuffham and Balogh 2006; Alexeev et al. 2008). The separation of external and internal terms in the measurements has been discussed in general terms by Olsen et al. (2009), and specifically for Mercury by Connerney and Ness (1988), Korth et al. (2004), Scuffham et al. (2006), Anderson et al. (2008, 2009) and Johnson et al. (2009). An additional factor especially important for Mercury is the role of induced magnetic fields (Grosser et al.

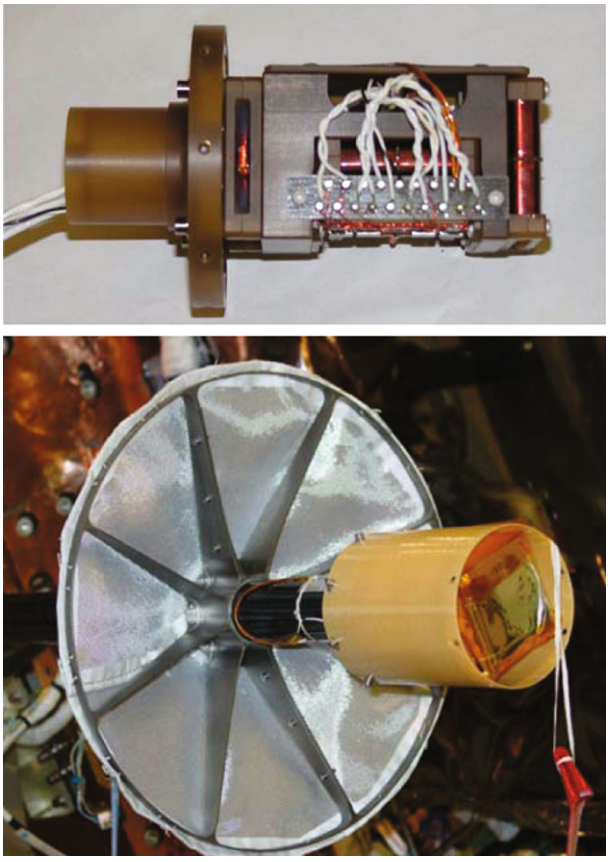

Fig. 20 *Upper panel*: The MESSENGER tri-axial fluxgate magnetometer sensor. *The boom* mounting is on the left. The three single axis sensors can be seen in profile on the right. *Lower panel*: The MAG sensor mounted on the boom tip behind its special, additional heat shield. The sensor is inside a protective cover that was covered with a thermal blanket prior to launch (photos courtesy of M.H. Acuña and B.J. Anderson)

2004; Glassmeier et al. 2007a; Saur et al. 2009), due to the large iron core and the high variability of the external magnetic environment.

The magnetometer on board the MESSENGER spacecraft has been described in detail by Anderson et al. (2007). The magnetometer sensor (see Fig. 20, upper panel) is placed at the end of a deployable boom of 3.6 m. The scientific requirements impose an absolute accuracy of 3 nT in measuring the magnetic field. This implies that the spacecraft field at the location of the sensor should not vary by more than 1 nT. A mission to Mercury, particularly an orbiter, is exposed to a very harsh thermal environment both from the factor 10 increase in solar input and from the infrared radiation of the planet's sunlit side. MESSENGER carries a sun-shield protecting the spacecraft; the magnetometer boom is extended in the anti-sunward position. An additional, more local shield was also needed to further protect the magnetometer when during orbital manoeuvres there will be intervals when the magnetometer is not in the shade of the sun-shield (Fig. 20, lower panel). Particular care had to be applied to the design and construction to this local shield, in particular to the materials used, to avoid the generation of thermo-electric currents that would affect the performance of the magnetometer. As the sensor is operated in the shadow of the spacecraft and its protective shield, its temperature in orbit will be less than 20°C even when illuminated by the planet, in fact the sensor carries a non-magnetic heater (already used on previous missions an thus fully flight-proven) which operate in a proportional mode from −15°C and −40°C.

The MESSENGER magnetometer is a three-axis ringcore fluxgate, originally developed in the 1970s by Acuña (1974) and successfully flown in continually improved versions and with different analogue and digital electronics on a large number of missions. Other planetary magnetometers by M.H. Acuña will be cited extensively in this paper. The sensor is operated during the mission in a single range of ±1530 nT per sensor axis; using a 20-bit analogue-to-digital conversion but transmitting only 16 bits gives a digital resolution of 0.047 nT. (There was an additional, high-field range of ±51,300 nT built into the instrument for ground-testing before launch.)

The analogue outputs of the three sensors are first filtered by 10 Hz low-pass filters to avoid aliasing and then digitized at the rate of 50 ms per sample in three parallel analogue-to-digital converters (ADCs). The 20-bit ADCs are synchronized and transmit the digitized values of the three magnetic field components to the instrument's Event Processing Unit (EPU) that takes care of instrument-specific control functions such as triggering the synchronization of the samples. The EPU interfaces with the Digital Processing Unit of the spacecraft to receive commands and to transmit the data to the telemetry. The optimized functionality of the instrument in matching the transmitted data (in terms of using matched analogue and digital filters) and data rate (in units of vectors/s) is very complex but results in 11 possible data rates, from 0.01 to 20 samples/s, covering all the possible data rates required by the scientific requirements. The performance of the MAG instrument on MESSENGER has been excellent through to date and it is expected to complete the survey of Mercury's magnetic field during the orbiting phase of the mission.

The highly variable contribution, already emphasised, that the external currents make to measurements in Mercury orbit will limit the scope of single-point measurements in determining the fine structure of the planet's internal magnetic field. Models of the origin of Mercury's internal field and the relationship of the presumed dynamo to the internal structure, state and material properties of the planet may only be distinguished by more accurate values that can be attributed to the internal field. This accuracy is limited by the need to remove the variable external component from the observed data. The joint BepiColombo mission of the European Space Agency and Japan's Aerospace Exploration Agency (JAXA)/Institute of Space and Astronautical Science (ISAS), due to be launched in 2014, will consist of two orbiters around Mercury, operating at the same time (Benkhoff et al. 2010). The Mercury Planetary Orbiter (MPO) supplied by ESA will have a low altitude, nearly circular polar orbit, while the Mercury Magnetospheric Orbiter (MMO) of JAXA/ISAS will have an eccentric orbit synchronized to the MPO orbital period. The currently planed orbits are shown in Fig. 21. The periods of the orbits are, respectively, 2.3 hours for the MPO and 9.2 hours for the MMO, allowing coordinated phasing for simultaneous measurements.

Both spacecraft carry magnetometers. The magnetometer on the MPO has been described by Glassmeier et al. (2010) and the one on the MMO by Baumjohann et al. (2010b). On the

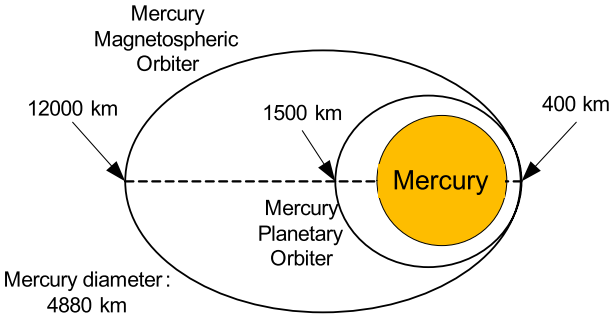

Fig. 21 Orbits of the two spacecraft, Mercury Planetary Orbiter and Mercury Magnetospheric Orbiter of the BepiColombo mission

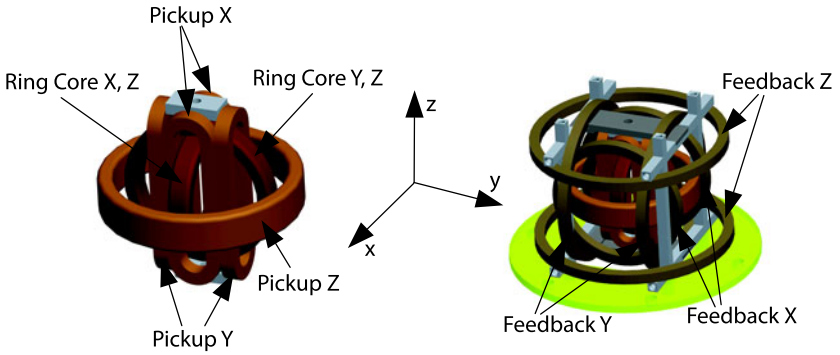

Fig. 22 Schematic drawing of one the two triaxial fluxgate sensors used on the BepiColombo Mercury Planetary Orbiter. *On the left*, the inner part of the sensor is shown, consisting of the two orthogonal ringcores surrounded by the sense or pick up coils for each axis. *On the right*, the same sensor is shown enclosed in the triaxial coil system that generates the feedback field to null the field at the sensor (from Glassmeier et al. 2010)

MPO, two identical triaxial fluxgate sensors are used on a 2.8 m boom extending from the spacecraft, to enable the use of the dual magnetometer/gradiometer technique to determine and remove the spacecraft background field (Ness et al. 1971; Neubauer and Schatten 1974), even though the technique needs to be applied with considerable care (Davis et al. 1973). The geometrical arrangement of the sensors and pick up and feedback coils is different from the arrangement used, for instance, on MESSENGER, and has the advantage of being compact and very light. The sensors use two ringcores in orthogonal planes; by placing orthogonal pickup or sense coils around each ringcore as shown in Fig. 22 the components of the magnetic field in all three orthogonal directions can be measured. In this design, the feedback coils (two circular coils per axis) are separated from the sense coils and use a quasi-Helmholtz geometry.

The feedback coils are also used for a vector compensation of the sensors whereby a magnetic field of programmable magnitude and direction can be applied, up to $\pm$5,000 nT per axis, to null the effect of static background fields generated by the spacecraft.

A further feature of the MPO magnetometer is the use of digital front-end electronics in lieu of the more classical analogue design. As described in more detail above in Sect. 2.1, in the digital magnetometer electronics, the sensor signal is digitized at a high rate ($\sim$40 kHz) and processed to generate the feedback current signal through a precision digital-to-analogue converter. The controller associated with this function handles at the same time the sensor and the interface to further digital processing of the instrument data for transmission to the telemetry. Digital magnetometers of similar design are already used in the instruments on the Rosetta Comet Lander (Auster et al. 2007), the Venus Express mission (Zhang et al. 2006), and planned missions to Jupiter (O'Brien et al. 2007). There is a single measurement range of $\pm$2,000 nT per axis, with a resolution of 2 pT, and an instrument noise of $\sim$10 pT/Hz$^{1/2}$. The telemetry depends on the different operating modes of the spacecraft and the instrument; magnetic field samples will be taken at rates of 0.5 to 64 vectors/s, with a short-duration burst mode when 128 vectors/s can be recorded.

As for the MESSENGER magnetometer described above, a key consideration of the accommodation of the magnetometer sensors on the boom of BepiColombo has been the thermal protection against both direct sunlight (which is up to $\sim$10 times more intense than in Earth orbit) and illumination in the infrared from the sunlit surface of the planet. The

sensor has been designed to operate in the unusually wide temperature range of $-100°C$ to $+200°C$ and has a low ($\sim$50 pT/°C) thermal offset drift coefficient. A protective cover envelops the sensor, consisting of a box shaped structure supporting Optical Solar Reflectors (OSRs), a frequently used device for thermal protection which has a low absorptance ($\alpha = 0.1$ to 0.2 at the end-of-life) and high emittance ($\varepsilon > 0.8$). Also, because of the high temperatures of surfaces exposed to the Sun, large temperature gradients are expected and, unless special care is taken, the possibility of thermoelectric currents. The potential variability of these currents is a serious hazard to the objectives of the investigation, and both careful design and extensive testing are required to avoid their harmful effects.

The second component of the BepiColombo mission is the Mercury Magnetospheric Orbiter (MMO), a spinning spacecraft in a more eccentric orbit than the MPO, concentrating on a suite of magnetospheric instruments, although with some planet-targeted telescopes as well. The magnetometer on the MMO (Baumjohann et al. 2010b) is also a dual tri-axial fluxgate, the outboard one mounted at the tip of a 4.4 m boom, while the inboard one is located at 1.6 m from the boom tip. The two sensors are different, the outboard one closely resembles the sensors on the MPO, including the front-end digital version of the electronics, while the inboard one is a classical sensor consisting of three ringcores arranged in an orthogonal triad, with an analogue version of the front-end electronics, similar to the schematic shown in Fig. 5 in Sect. 2.1.

In order to use the two sensors for implementing the background measurement and elimination using the dual-magnetometer method (Ness et al. 1971; Neubauer and Schatten 1974), it is important that the two magnetometers be fully synchronized for simultaneous measurement of the magnetic field. This is ensured by their common use of a 128 Hz synchronization signal. Otherwise, the magnetometers are fully independent of each other; each is operated on a different electronics and data chain on board to provide full redundancy.

The operating range of the magnetometers is ± 2000 nT with a 3.8 pT digital resolution. Each samples the magnetic field at the rate of 128 vectors/s. This high sampling rate provides the capability to observe that high variability of Mercury's plasma environment; from an instrumental point of view, it also allows a high level of correlation of the spacecraft-generated background so that it can be removed with high accuracy from the measurements.

The principal advantage of the two-spacecraft approach to determine Mercury's magnetic field is that the external conditions, the very highly variable magnetosphere, can be better characterised and its effects better identified in the measurements. A more accurate and more detailed determination of both the magnetospheric and the planetary magnetic field is expected from the mission.

3.2 Venus

There are close similarities between Venus and the Earth in terms of size and density, although there are also significant differences, not only because of Venus' atmosphere and surface temperature, but also because of its very slow and retrograde rotation rate. It is this slow rotation rate that already implies that if there is a dynamo in the interior of Venus, it is much weaker than that of the Earth, so that no Earth-sized dipole field was expected. Scaling laws led Busse (1976) to predict a surface field for Venus of about a fraction $1/430$ (or less) of the Earth's surface field. Consequently, the scale (and nature) of the interaction of the solar wind with Venus was certain to be different from that of the Earth. However, given the uncertainties in both the knowledge of Venus's interior state and its thermal evolution, as well as in dynamo theory, measurements were essential to confirm the existence or absence of an intrinsic magnetic field for Venus.

In the 1960s, several early space probes attempted to approach Venus carrying a magnetometer in their payload. Mariner 2, launched in 1962, was the first to report an absence of magnetic signature as it flew by on 14 December 1962 on a trajectory with a closest approach of ∼41,000 km or 6.77 Venus radii (Smith et al. 1963). The absence of any signature that could be associated with the flyby of the planet excluded an intrinsic magnetic field at all comparable to that of the Earth. During the flyby, the components of the measured magnetic field digitized with relatively large steps (using an 8-bit analogue-to-digital converter) so that the total change in the magnetic field amplitude was less than 10 nT (Smith et al. 1965a, 1965b). Changes of this magnitude were seen by Mariner 2 away from the encounter, so even this small value could not be attributed to the planet. An upper limit of the planetary field estimated by Smith et al. (1965a, 1965b) was at most about 5% of that of the Earth; it was estimated, that an identical trajectory to that of Mariner 2 around the Earth would have yielded a signal of amplitude ∼125 nT. The magnetometer used on the Mariner 2 mission was a three axis fluxgate (FGM) instrument (fabricated by Institut Dr Förster, Germany) with the electronics built under the supervision of the Jet Propulsion Laboratory.

Mariner 5 had been the backup spacecraft for the Mariner 4 mission to Mars. However, as Mariner 4 was successful (see Sect. 3.2), Mariner 5 was sent to Venus instead. Launched on 14 June 1967, the spacecraft flew by Venus on 19 October 1967 at a closest approach distance of 4,000 km. This allowed a good set of measurements of Venus' plasma and magnetic field environment (Bridge et al. 1967) that provided the basis for a valid first model of the characteristics of the planet-solar wind interaction features, dominated by the Venus ionosphere. However, It was not possible to exclude the possibility of a weak intrinsic magnetic field, but the close approach allowed to establish a much lowered upper limit, less than a fraction $1/400$ of that of the Earth, than was possible with Mariner 2. The magnetometer on Mariner 5 was identical to the one flown on Mariner 4; it was the first time a quantum effect instrument, a Vector Helium Magnetometer was embarked on a planetary mission (Slocum and Reilly 1963; Connor 1968). This instrument is described in more detail in Sect. 2.2, see also Fig. 28.

A series of Soviet spacecraft were aimed at Venus in the 1960s, 1970s and 1980s, with the primary aim of delivering entry probes and landers; however, some magnetic field measurements were also made. A value of $\sim 3 \times 10^{12}$ T m^3 for the intrinsic magnetic field was proposed by Dolginov et al. (1978), so about a fraction $1/3000$ or less of the Earth's dipole. Also, on its way to Mercury in early 1974, NASA's Mariner 10 spacecraft flew by Venus at a closest approach of ∼5800 km and confirmed the previous upper limit for the magnetic field through the observation and positioning of a bow shock (Ness et al. 1974).

Pioneer Venus Orbiter, launched on 20 May 1978 and inserted into orbit around Venus on 4 December 1978 provided the best comprehensive set of observations in the complex plasma environment to determine Venus' intrinsic magnetic field. The instrument has been described by Snare and Means (1977) and Russell et al. (1980a). The magnetometer was of the fluxgate type, with three single axis sensors, but located somewhat unusually along a 4.7 m long boom. Two of the single axis sensors were located at the boom tip, to minimise the spacecraft-induced background, while the third sensor of the tri-axial set was located at about 1.7 m inboard on the boom, inclined at 45° from the spacecraft spin axis. The arrangement is shown schematically in Fig. 23.

Initial observations suggested that it was much less than 10^{12} T m^3 (Donahue 1979). A more detailed analysis yielded 4.3×10^{11} T m^3 (Russell et al. 1980b, 1980c) as an upper limit. A significant improvement on this value could only be reached by a more extended spatial coverage around the planet and an in-depth examination of all the possible sources

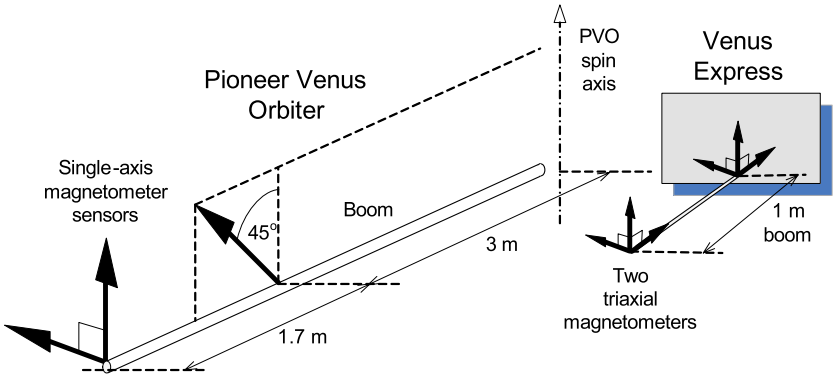

Fig. 23 The geometry of the fluxgate magnetometers used on Pioneer Venus Orbiter (Russell et al. 1980a, 1980b) and Venus Express (Zhang et al. 2008). The three-axis magnetometer on PVO was notable for the unique geometry of removing one of the sensors to a third of the way from the boom tip and installing it at an angle with respect to the spin axis to act also as a gradiometer monitoring the background field of the spacecraft. The dual tri-axial senor arrangement on VeX is also unique in that one set is on the tip of the 1 m long boom, while the other is installed on the spacecraft at the boom root. A highly complex and novel data processing method uses the output of the two tri-axial sensors to eliminate the background caused by the spacecraft

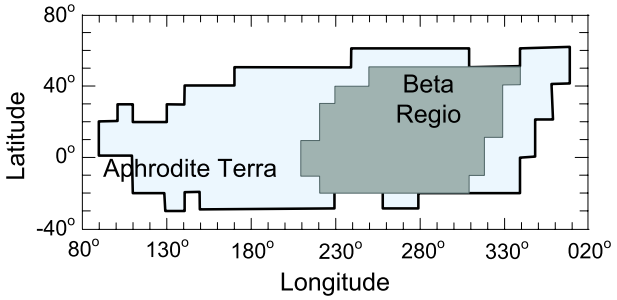

Fig. 24 Pioneer Venus Orbiter coverage used for the definitive data analysis to establish the likely absence of any intrinsic planetary field and to lower the limits of uncertainty. The original analysis by Russell et al. (1980b) used the darker shaded area, while the later analysis by Phillips and Russell (1987) used the larger, lighter shaded area that led to a reduction of by a factor 3 in the upper limit for the intrinsic magnetic field. The limitations that defined the spatial extent of the usable data were the altitude (North and South) and the flow zenith angle (East and West), defined to exclude the regions affected by the solar wind interaction with the ionosphere of the planet (after Phillips and Russell 1987)

of error, including instrumental errors (Phillips and Russell 1987). In particular, given the longer data set in the latter work, the coverage over the planetary surface was significantly increased, as shown in Fig. 24. As a result of this work, the deduced value for the intrinsic magnetic field of the planet is consistent with zero, with an upper limit (based on the uncertainties in the determination) 8.4×10^{10} T m^3, so at least a factor 100,000 weaker than that of the Earth.

The selection of data that can be used from the orbiter data that was collected is a critical step in the determination of the planetary field (Russell et al. 1980c). First, the data set used needed to be restricted to a volume near the planet in which magnetic field measurements could be considered to include the intrinsic field of the planet without being overwhelmed

by other sources of magnetic fields, such as currents resulting from the interaction of the ionosphere with the solar wind. The strongest currents are on the sunward side of the planet; the analysis excluded the dayside region by limiting the data set to solar zenith angles greater than 120°. Additionally, the altitude above the surface was limited to a maximum of 600 km from the periapsis height of 150 km. The combination of the height and solar zenith angle constraints restricts the usable seasons when the usable data were collected. As the orbit was fixed in inertial space, and the rotation period of Venus is very long (243 days in a retrograde direction) there was an overlap between the planetary longitudes covered from one night-time season to the next. The later re-examination of the usable volume by Phillips and Russell (1987) led to increasing the volume used by raising the maximum altitude of the volume to 750 km and relaxing the condition on the solar zenith angle from 120° to 105°.

The usable volume during the night-time portions of the orbit was divided into $10° \times 10°$ bins in planetary latitude and longitude. These bins contained data from a variable number of orbits and there fore varying quantities of data; in the first study by Russell et al. (1980c) two seasons were included in which the periapsis fell within the restricted volume (one of these in fact was used only partially because of limited ground coverage of the telemetry), while in the later study, Phillips and Russell (1987) could use three additional seasons of data from 378 orbits, giving a total of 18,000 vectors, each a 12-second averaged value that were used in the analysis.

The data in each bin was averaged and used to calculate the equivalent value of the planetary dipole that would yield the observed magnetic field value in the centre of the bin. Thus a large number of "equivalent" dipole moments, a total of 181 were calculated that were used to derive a mean value for the components of a equivalent planet-centred dipole. Error calculations, taking into account that not all moment determinations were independent, yielded error values that were commensurate with the values of the components of the planetary moment determined from the measurements (that would yield a surface field of $\sim$0.35 nT). The Pioneer Venus Orbiter results are therefore consistent with a zero intrinsic planetary magnetic field. The reasons for the apparently complete absence of a global magnetic field source within Venus is not yet understood, although modelling its thermal evolution it is possible to derive scenarios and parameters that would lead to such a non-magnetic state.

The next mission to Venus equipped with a magnetometer is the currently operating Venus Express of the European Space Agency, launched on 9 November 2005 and inserted into an eccentric 24-hour orbit around Venus on 11 April 2006. The spacecraft, a copy of ESA's Mars Express spacecraft, had not been designed to be magnetically clean (Mars Express did not carry a magnetometer), nor to have a magnetometer boom, so the instrument selected to be included in the payload was a dual tri-axial fluxgate magnetometer that comprised also a boom to carry one of the vector sensors. The boom could only be 1 m long and the second vector magnetometer had to be mounted on the spacecraft platform immediately next to the mounting of the boom. The arrangement is shown schematically in Fig. 23, next to the PVO sensor arrangement.

Although PVO had shown that Venus does not possess a measurable global internal magnetic field, its limited coverage (see Fig. 24), particularly at high latitudes, leaves the opportunity to Venus Express to search for local magnetization, given its periapsis at high latitude (80°). Even though surface temperatures are above the Curie temperature for basalt rock, pure iron or material under high pressure may preserve historic magnetization (Tielong Zhang, personal communication). The orbits of PVO and Venus Express are illustrated in Fig. 25.

For the Venus Express magnetometer, producing usable data in the presence of the very high spacecraft magnetic background at the magnetometers sensors has been a unique challenge (Zhang et al. 2008; Pope et al. 2009). Full use is made of the dual magnetometer

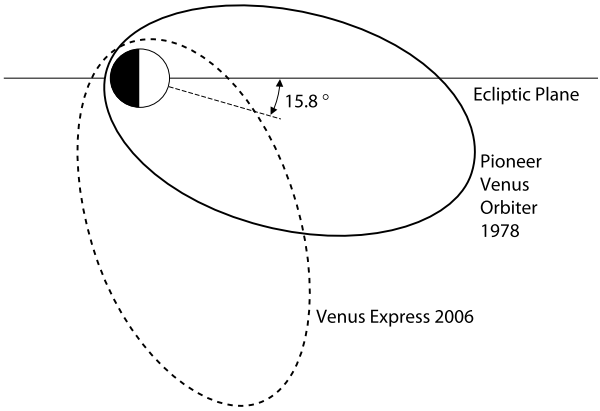

Fig. 25 The orbits of Pioneer Venus Orbiter and Venus Express. Both orbits have a period of 24 hours, with a periapsis of 150 km for PVO and 250 km for Venus Express. The periapsis latitude for Venus Express is 80°. The high latitude of the periapsis of Venus Express provides opportunities for exploring potential local sources of magnetisation

technique first proposed by Ness et al. (1971) but rarely used to its full capability; even in this case, the technique is used in a highly sophisticated mathematical environment to avoid the potential pitfalls pointed out by Davis et al. (1973). For the Venus Express instrument, one of the key features is the simultaneous high speed sampling of the ambient field vector, at 128 Hz, at the location of the two sensors. Both sensors are affected by large stray fields, typically ∼200 nT at the outboard location and several thousand nT at the boom root. The basic measurement ranges are, respectively, ±262 nT and ±524 nT, but both sensors can be automatically compensated whenever necessary by an artificially imposed field of up to ±10,000 nT. The relatively low value ranges are justified by the high resolution that can be achieved when the magnetic field at the outboard sensor is within the measurement range. There are several operational features of the spacecraft related to the solar array driving mechanism, the antenna and the reaction wheels, among others, that generate large transient background effects. The data processing and calibration software operates on the differences between the values measured by the outboard and inboard sensors. The software incorporates self-adapting features, such as neural networks and fuzzy logic to characterise the disturbances that need to be removed. The methodology used does not aim to identify the sources of the disturbances but only their effects at the location of the outboard sensor. It has been estimated (Zhang et al. 2008) that after the data cleaning operations, the absolute value of the magnetic field can be determined to an accuracy ∼1 nT, and that the differences can be determined to ∼0.1 nT.

3.3 Mars

For a surprisingly long time, for more than thirty years after the first missions to Mars, it remained unclear whether Mars had an intrinsic magnetic field. The measurements by the American probe Mariner 4 and by several Soviet probes (Mars 2, 3 and 5 and Phobos) showed a magnetic signature that could be associated with the interaction of the solar wind with Mars. However, it was not possible to conclude if the obstacle was only Mars's ionosphere or the ionosphere combined with a weak planetary field. The upper limit (or perhaps the value) of Mars's magnetic moment was stated to be about 10^{12} T m^3, or about a fraction 10^{-4} of the Earth's field. The failure to determine the magnetic field of Mars was at first the lack of a sufficiently close-by orbiter data, and also the somewhat limited resolution of the magnetometers on the Soviet probes. But possibly the most important factor was the difficulty to identify and isolate in the observations a non-dipolar, yet important

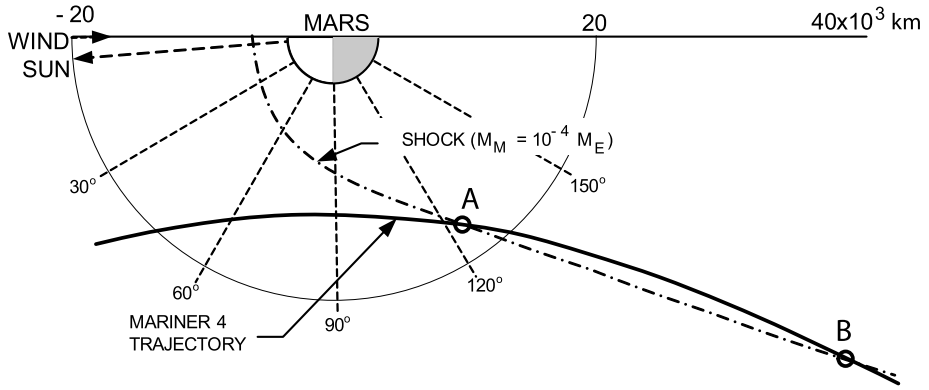

Fig. 26 The flyby trajectory of Mariner 4 at Mars. The contour of a bow shock scaled from that of the Earth, assuming that the magnetic moment of Mars is a fraction of 1/10,000 of that of the Earth is also shown, together with the two points marked A and B that correspond to the sudden increase and sudden decrease in the magnetic signal shown in Fig. 27 (after Smith 1969)

magnetic field against a background dominated by the interaction of the solar wind with the ionosphere in somewhat similar manner to what happens at Venus.

The first mission with an interesting, but far from definitive result was Mariner 4 which was launched on 28 November 1964 and flew by Mars on 15 July 1965. The flyby orbit is shown in Fig. 26; the closest approach was at 9,846 km from the Martian surface at 01:00:57 UT. The mission was successful, particularly in providing the first close-up photographs of Mars. The magnetometer operated throughout the flyby, the data it provided are shown in Fig. 27. Just after closest approach (at 13,200 km or $3.9R_M$), there was first an abrupt increase in the magnitude of the magnetic field at 01:23 on 15 July 1965, followed by an equally abrupt decrease three hours later, as described by Smith et al. (1965a, 1965b) and by Smith (1969). (There was a 54 minute gap in the telemetry during this interval, due to Mars eclipsing the spacecraft from Earth visibility.) These two events, marked A and B in Fig. 27, corresponded to the points also marked A and B along the flyby trajectory. A bow shock, scaled from that of the Earth assuming a magnetic moment $\sim 1/10^4$ smaller for Mars is shown in Fig. 26, matched to the two points along the trajectory with the abrupt changes in the magnetic field magnitude. Smith et al. (1965a, 1965b) and Smith (1969) pointed out that although the interaction of Mars with the solar wind could be similar to that of Venus, i.e. mostly/wholly with the ionosphere of the planet, the observations were also consistent with a small Martian intrinsic field. This point was emphasised by the modelling comparisons between Earth and Mars by Dryer and Heckman (1967) who concluded that the magnetic dipole moment of Mars was about 3×10^{12} T m^3, close to the possible value suggested by Smith et al. (1965a, 1965b). The magnetometer used on this mission was the first vector helium instrument (Connor 1968) that was to lead to a series of instruments on key planetary missions for the next 40 years. The schematic of the instrument is shown in Fig. 28.

The interpretations of the observations of the Soviet probes Mars 2, 3 and 5 in the 1970s remained controversial, given that it was possible to argue that the ionospheric interaction model, as for Venus, could explain qualitatively and quantitatively the observed size and character of the obstacle to the solar wind flow (Russell 1978). That interpretation itself was challenged on the basis of the comparison between respective abilities of the ionospheres of Venus and Mars to hold off the solar wind and act as the primary obstacle to the flow (Slavin and Holzer 1981) who concluded that unless the solar wind pressure is exceptionally high,

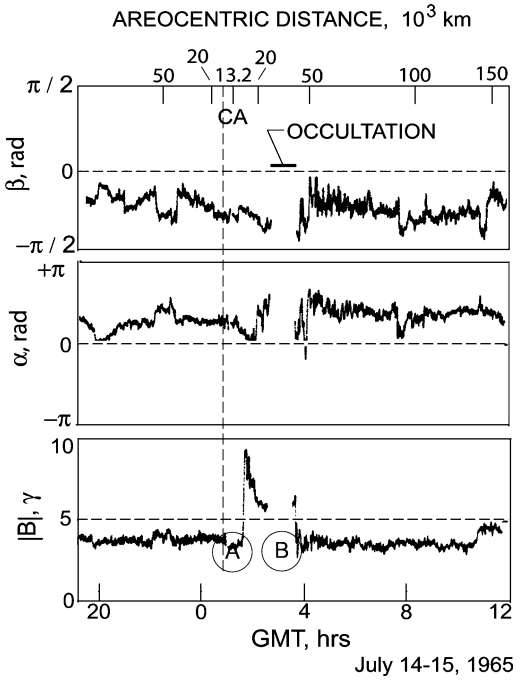

Fig. 27 The sudden increase followed by a sudden decrease in the magnetic field (marked A and B) appears to correspond to the inbound and outbound crossings of the Martian bow shock as illustrated by the open circles at points A and B on the flyby trajectory in Fig. 26. This is likely to be the first evidence, long disregarded, that Mars has a small magnetic field, although its nature as a remnant crustal field could not be appreciated (after Smith 1969)

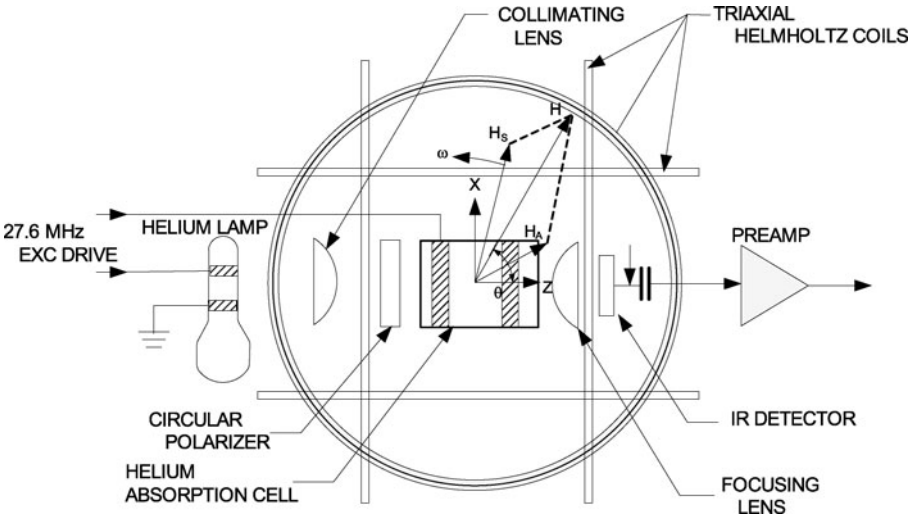

Fig. 28 The vector helium magnetometer used on the Mariner 4 spacecraft that was the first to measure a significant magnetic signal in the vicinity of Mars. An identical instrument was flown on the Mariner 5 mission to Venus (after Connor 1968)

the size of the obstacle in the case of Mars did imply an intrinsic field somewhat in excess of 10^{12} T m^3.

However, Dolginov et al. (1973) insisted on a weak intrinsic field of about 2.4×10^{12} T m^3 that implied an equatorial intensity of about 60 nT, based on the observations of the bow

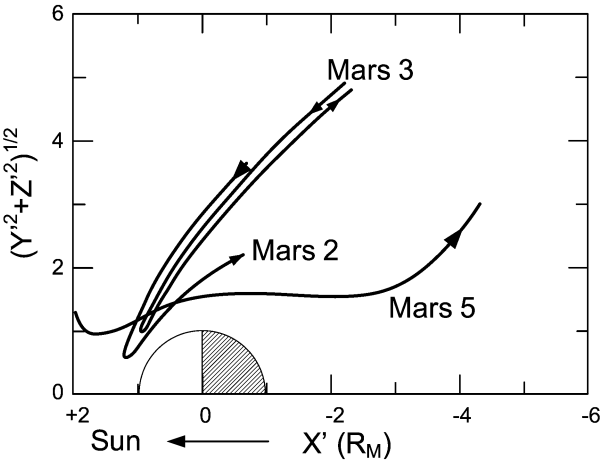

Fig. 29 Trajectories of the Soviet Mars probes that reached the planet in the 1970s and were able to detect the bow shock but could not decisively determine the nature of the interaction with the solar wind, in particular whether a small planetary magnetic field contributed to the interaction in addition to the Venus-like ionospheric interaction type (after Slavin et al. 1991)

shock by the Mars 2 and 3 probes. These authors came to an interestingly insightful conclusion: "Such a small dipole moment can be understood if it is assumed that the observed field is an ancient field, being a trace of a magnetic dynamo existing in the past. In any case, it can be expected that, on the surface of Mars, regions with fields of high intensity can exist." Following the next successful space probe, Mars 5 that was placed in orbit around Mars on 12 February 1974, the arguments in favour of a small intrinsic field were reinforced by the observations (Dolginov et al. 1976). The trajectories of the Mars 2, 3 and 5 spacecraft are shown in Fig. 29; these were sufficiently close to the planet to observe the effects of the solar wind interaction with the ionosphere, but (as has been made clear by the Mars Global Surveyor measurements described below) were not able to detect the highly localised crustal magnetic sources.

The last exchange of arguments on whether Mars had an intrinsic field or not occurred following the Phobos-2 mission (Möhlmann et al. 1991; Dolginov 1992; Russell et al. 1992). The trajectory of Phobos 2 around Mars is illustrated in Fig. 30 (after Slavin et al. 1991); Möhlmann et al. (1991) concluded that the solar wind interaction is primarily with the ionosphere/upper atmosphere of Mars, but they also found some periodic signatures in the magnetic field that corresponded to the rotation of the planet. It was this signature that was interpreted by them as evidence of an intrinsic magnetic field. Slavin et al. (1991) examined data from all the previous Mars missions, from Mariner 4, to establish the position and variability of the Martian bow shock. Both the mean distance of the bow shock at about 1.5 planetary radii corresponding to an "obstacle" to the solar wind at a height about 500 km and its lack of dependence on the phase of the solar cycle were arguments for the interaction with the solar wind to be different from that of Venus. This therefore led to the conclusion of a small intrinsic field of $\sim 10^{12}$ T m^3, as concluded by the majority of the previous studies. Slavin et al. (1991) also noted the unusually large bow shock distances observed occasionally by Mars 2, 3 and Phobos 2. These distances were compatible with a height of the Martian obstacle of 2000 to 4000 km, incompatible with the ionospheric-only interaction model. Furthermore, an explanation based on low solar wind pressure was also unlikely, as the solar wind parameters implied were quite unrealistic but not impossible. There was only a limited sample of such extreme bow shock crossings that could not be statistically related to the planetary rotation and remained at that stage without a satisfactory explanation. However, the later observations of Mars Global Surveyor confirmed the likelihood that periodic asymmetries in the bow shock location corresponded to the phasing of the most

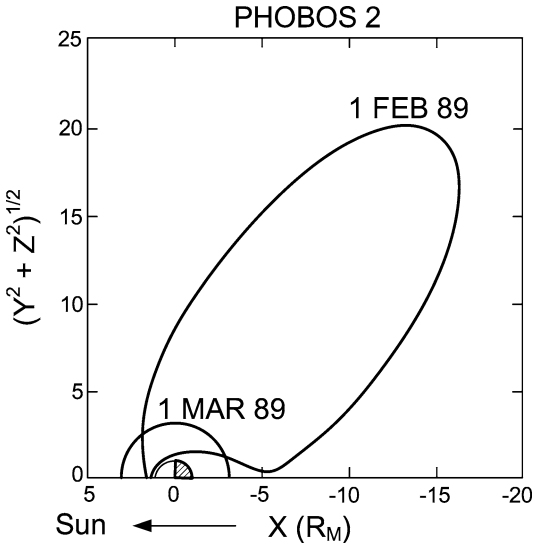

Fig. 30 Two typical orbits of the Phobos 2 spacecraft that allowed the determination of the solar wind interaction with the ionosphere of Mars, but was not sufficiently close to the planet to detect the high intensity, highly localised crustal sources (after Slavin et al. 1991)

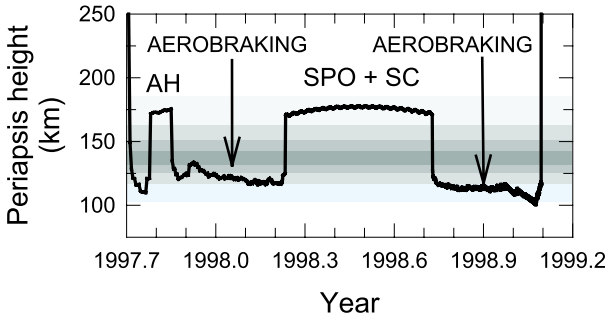

Fig. 31 The height of the periapsis of the Mars Global Surveyor Orbit during the first, aerobraking phase of the mission, below the ionosphere, shown in *the grey shaded area* (according to a model derived from Mars Express observations). The periapsis was raised twice, once for troubleshooting (AH: Aerobraking Hiatus) and once for awaiting for the phasing of the orbit (SPO: Science Phasing Orbits) and because of solar conjunction (SC). The lowest periapsis phases were the best suited to map Mars's crustal magnetic field. The periapsis was raised to ∼380 km (off the scale of the figure) in March 1999 for the start of the mapping phase of the mission

intense crustal magnetic sources that extended the size of the Martian obstacle to the solar wind (Acuña et al. 1999).

The resolution of the question of Mars' planetary magnetic field came from the magnetic field observations by the Mars Global Surveyor (MGS) spacecraft (Dallas 1997). MGS was launched from Earth on 7 November 1996, placed into orbit around Mars on 11 September 1997 and operated until 2 November 2006. The eventual operational orbit, the circular mapping orbit, at a height of ∼380 km above the Martian surface) was achieved in March 1999. In the early part of the mission, the original high eccentricity orbit with a period of ∼44 hours was gradually modified using aerobraking, exploiting the drag of the spacecraft at periapsis to lower the apoapsis and circularise the orbit. The history of the periapsis height during the aerobraking phase of the mission is shown in Fig. 31, together with a grey-shaded representation of the ionospheric electron density, based on Mars Express measurements of

the electron density. The peak density is at ∼140 km, above the periapsis during aerobraking, as can be seen in Fig. 31.

The observations during this early phase of the mission, particularly those during the lowest periapsis, aerobraking phases have led to the definitive result that Mars has no measurable global magnetic dipole and to the discovery that part of the Martian crust is magnetised (Acuña et al. 1998, 1999, 2001; Ness et al. 1999). The latitude range of the periapsis around which the measurements were made was first in the northern hemisphere but, during the second aerobraking phase, moved to the southern hemisphere close to the polar region. A reasonably comprehensive coverage in latitude could therefore be performed. As concluded by Acuña et al. (1998), the magnetic field observations show an interaction of the atmosphere/ionosphere with the solar wind, similar to that on Venus. However, MGS also detected highly localised, intense sources of magnetisation. One of these measurements, during the first aerobraking phase is shown in Fig. 32 (from Acuña et al. 1998). The measurements, made at ∼100 km, show the source with magnetic field strengths of 400 nT, compared to the upper limit of a few nT expected from a possible global field.

The comprehensive survey through the whole aerobraking phase of the mission was reported by Acuña et al. (1999) who provided a map and a description, in terms of Martian geology, of the sources of crustal magnetisation. During the second aerobraking phase, magnetic fields up to ∼1600 nT were measured, representing intense sources that are likely to be the causes of the increased asymmetric Martian obstacle size first noted in the Phobos 2 data. Having established the extent and topography of the crustal magnetic field sources, the second phase of the MGS mission, the mapping phase at a close to circular orbit of ∼400 km height provided the confirmation of the earlier results and enabled a full description of the nature of the magnetism of Mars and the planet's interaction with the solar wind that shapes its environment.

As reported in detail by Acuña et al. (2001) who included observations from the mapping phase of MGS as well, it is now certain that Mars had a planetary scale dynamo in its very early history, but that the dynamo stopped operating at about 3.9 Gy ago. The crustal magnetisation is effectively restricted to the very old, heavily cratered terrain in the highlands in the southern hemisphere. There are numerous implications for the evolution and geology of Mars in the magnetic field maps that have been extensively discussed in the literature (see Connerney et al. 1999; Nimmo and Stevenson 2000).

There were two factors in the great achievement of Mars Global Surveyor in providing answers to the long-standing questions concerning the magnetic field of Mars. One was undoubtedly the mission orbit design which included a low periapsis phase, essentially below the ionosphere for a significant interval of time early in the mission (see Fig. 31). (Note that this phase was primarily introduced as part of the strategy to lower the apoapsis through repeated aerobraking passages in the upper atmosphere near periapsis, but it proved to be crucial in resolving the question of the Martian magnetic field.) An example of the very highly localised intense crustal filed signatures is shown in Fig. 32 (after Acuña et al. 1998); these fields could only be measured at the altitudes the MGS altitudes during the mission phase when it was very close to the surface of the planet. The second was the remarkable implementation of the magnetometer experiment on the MGS spacecraft. The instrument itself was identical to that flown on the Mars Observer spacecraft launched in 1991; however, that spacecraft failed just before Mars orbit insertion. MGS was conceived as a replacement for Mars Observer, but one that had a radically different configuration to match a less capable launcher that had been used for Mars Observer. Due to this reduction in resources, the experiment package with the purpose of discovering the true nature and extent of Mars's magnetic field, the magnetometer and the electron reflectometer could not be mounted on a

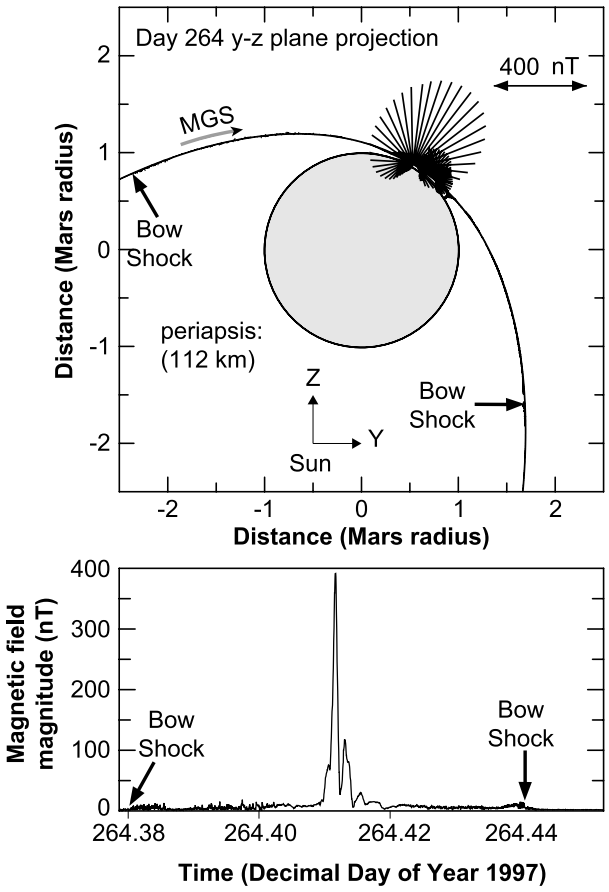

Fig. 32 The magnetometer on the Mars Global Mission discovered isolated magnetic anomalies that gave sudden, very large increases in the measured magnetic field, showing that they corresponded to highly magnetised, but locally narrow crustal features. *Upper panel*: projection of the near-periapsis orbit of MGS with a projection of the measured magnetic field vector along the orbit. The view is from the Sun, in a plane perpendicular to Mars' equatorial plane. *Lower panel*: the measured magnitude of the magnetic field through the periapsis pass. Two distinct anomalies can be seen, the first, larger one near 32.9°N latitude, 22.4°W longitude, the other near 22.8°N latitude and 23.6°W longitude (after Acuña et al. 1998)

boom as they had been on Mars Observer (which had a deployable 6 m boom), so another accommodation was needed that would enable the magnetometer to measure the expected nT range magnetic fields at Mars in the presence of a magnetically uncontrolled spacecraft. The configuration that was devised (Acuña et al. 1996) was to place the two triaxial fluxgate magnetometer sensors at the ends of the two solar panels (see Fig. 33). While this mounting removed the sensors from the spacecraft to a distance of 4.5 m, the length of the extended solar panels, it was important to minimise the magnetic field generated by the currents flowing in the solar panels. An ingenious wiring scheme was devised and extensively modelled that led to the nominal self-cancellation of the background fields at the magnetometer sensors (Acuña et al. 1996).

The in-flight performance of the magnetometer sensors in the spacecraft environment needed careful analysis to determine the sources of noise/background at the location of the sensors (Acuña et al. 2002). While the solar array performed close to the levels predicted by the pre-flight modelling (with a background field at the sensors <0.2 nT), other subsystems of the spacecraft did introduce significant levels of background that needed to be monitored and corrected. The Travelling Wave Tube Amplifier (TWTA) that was mounted with the high gain antenna of the spacecraft, in particular, introduced a background that proved to be a significant source of variable offset and needed to be characterised. During the first,

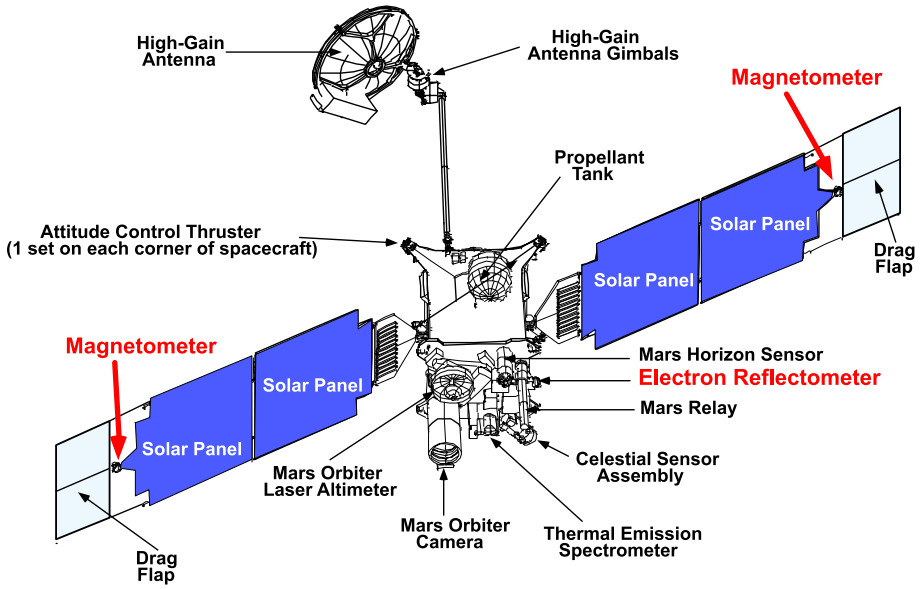

Fig. 33 General view of the Mars Global Surveyor spacecraft, indicating its main components, including the two tri-axial magnetometers at the ends of the solar panels and the electron reflectometer (after MGS—NASA Facts)

aerobraking phase of the mission, through to March 1999, the High Gain Antenna remained in a fixed position, so that its magnetic field seen at the location of the sensors was constant. However, during the mapping phase of the mission, the High Gain Antenna was constantly articulated and thus introduced a variable background at the location of the sensors that was synchronous with the orbit.

Modelling and subtracting the background due to the TWTA and the High Gain Antenna were essential. Measuring the magnetic fields simultaneously with the two sensors, at the ends of the two solar panels allowed to identify the "common mode" signal that was the ambient field due to Mars and the difference signal that was due to the spacecraft. As described by Acuña et al. (2002), the modelling of the differences led to an rms deviation between measurements and model of ∼0.5 nT with the solar panel in the shadow of Mars, and double that value when the solar panels were illuminated.

These outside contributions to the magnetometer zero level and its measurement noise have been significantly greater than the magnetometer's own zero-level offsets and noise. The stability of the zero offset for the Mars Observer magnetometer (identical to the one mounted on MGS) was better than 0.15 nT over a temperature range of $-40°C$ to $+60°C$. Based on previous magnetometer sensors of closely similar materials and construction used on missions such as Voyager, the estimated zero-level drift was determined to be about 0.2 nT/year. The noise of the magnetometer was 0.006 nT in the frequency band 0 to 10 Hz. These values (Acuña et al. 1992, 2002) show that the performance of magnetometers far surpasses the constraints on the measurements generated by external sources. This is the case for most missions, to the planets and elsewhere; the platform noise dominates the background in the data.

3.4 The Earth

The best known, longest studied planetary magnetic field is that of the Earth (see, for an up-to-date review, Hulot et al. 2010, this issue). Complementary to the very long series of ground-based observations, extending now for several centuries, the space age has brought a significant new tool in dedicated space missions that have provided extensive maps of the Earth's magnetic field from low-Earth orbit. Given the emphasis in the current review to planets other than the Earth, the following is intended to provide a brief summary of what has been achieved by spacecraft measurements and the missions and instruments that have been used to date. A review of space data and their contribution to geomagnetic field modelling from the early Sputnik 3 (1957) up to Magsat (1979–1980) was given by Langel and Baldwin (1992). A more up-to-date summary survey of the relevant missions, in particular Magsat, Ørsted and CHAMP, can be found in Kramer (2002) and Olsen et al. (2002).

An early series of low-orbiting satellites with a scalar magnetometer to measure the Earth's magnetic field were the three Polar Orbiting Geophysical Observatory (POGO) satellites launched and operated between 1965 and 1971. The POGO satellites (the low orbit members of the six OGO satellite series) were in polar orbits, with a perigee close to 400 km and an apogee between 900 and 1500 km. The satellites were large and extensively instrumented (each carrying in excess of 20 instruments). The payload included a rubidium-vapour scalar magnetometer (Farthing and Folz 1967). Measurements were made over a range of 15,000 to 64,000 nT and with a precision of 0.5 to 1.5 nT. The objective was to make refined measurements to improve the description of the magnetic field and to monitor secular variations. Although the precision of the magnetometer was not matched by the positional uncertainties (contributing maybe as much as a 7 nT error to the data), the three POGO satellites made a first significant and systematic contribution to the acquisition and use of space data for the main geomagnetic field (Cain 1971; Langel 1974). In addition, the measurements contributed to a better understanding of the structure and behaviour of the magnetic field in the inner magnetosphere (Cain and Sweeney 1970).

Magsat was the first spacecraft dedicated by NASA to the study of the Earth's magnetic field (Mobley et al. 1980; Langel et al. 1982). The spacecraft carried both a scalar and a vector magnetometer. It was launched on 30 October 1979 into a sun-synchronous orbit with an inclination of 97°, a perigee of 352 km and an apogee of 578 km. The orbital period was 94 minutes. The mission lasted seven and a half months before orbit instabilities led to the re-entry of the spacecraft into the atmosphere.

The Magsat instrumentation consisted of a caesium vapour scalar magnetometer that was due to deliver the magnitude of the magnetic field to an accuracy of 1.5 nT or better (Farthing 1980). Unfortunately, a partial failure of the scalar magnetometer limited its scientific usefulness, although it was able to contribute to the in flight calibration of the vector magnetometer. This latter was a triaxial fluxgate magnetometer (Acuña et al. 1978; Acuña 1980), built to have an especially high level of mechanical, thermal and magnetic stability. The triaxial fluxgate assembly is shown schematically in Fig. 34. The single axis sensors were of the classical ring core type, with the magnetic material being a specially selected molybdenum permalloy developed to have low noise and high stability, originally for the Voyager missions. The vector feedback was applied to each single-axis sensor separately, around a high-stability coil-former. The alignment and temperature stability of the feedback coil are critical for meeting the measurement requirements, as potentially the largest error sources. The reasons why the solution of a feedback coil system around the triaxial sensor assembly was not retained (that was to be used for Ørsted, see below) were partly the bulk of the

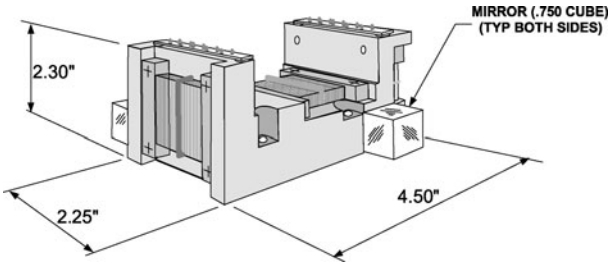

Fig. 34 Schematic diagram of the triaxial fluxgate magnetometer for Magsat (after Acuña et al., 1978)

external coil system and partly the excessive stray fields that would have been generated by the coils that would have disrupted the measurements of the scalar magnetometer that was physically relatively close to the vector fluxgate (see Fig. 34).

The triaxial assembly, as a whole, was manufactured out of a single block of machinable ceramic material characterised by its very low thermal expansion coefficient ($\sim 10^{-6}$), matched to that of the sensor core, its supporting structure and the feedback coil and its support. Dimensional stability and accuracy were of major importance to meet the demanding requirements: mounting surfaces were polished to an accuracy better than 10 μm and all structural deformations had to be less than 50 μm to ensure the alignment stability of 5 arcsecs. The magnetometer electronics, described in detail by Acuña et al. (1978), had to match the accuracy of the sensor. A fully redundant system was designed, with high precision components.

It was recognised from the outset that two of the key requirements for the spacecraft were a very precise attitude determination for the vector measurements, and a magnetically clean environment for both scalar and vector magnetometers. The attitude determination at the location of the three-axis fluxgate sensor could not be carried out simply, as the star sensors used on the spacecraft for the attitude determination were highly magnetic and could not be placed in the proximity of the sensors. The sensors were located at the end of a deployable boom that could not be constructed to ensure the necessary rigidity to ensure the required ± 5 arc sec accuracy, as illustrated in Fig. 35. Hence a complex Attitude Transfer System (ATS) was designed to implement the requirements (Mobley et al. 1980). A further requirement on the boom was to ensure that the ATS remained in its linear range for the determination of the orientation of the vector measurements. The total error budget for the vector magnetometer was ~ 6 nT (rms) along each axis. On the magnetometer itself, the accuracy requirement was 3.75 nT (including 0.5 nT for the spacecraft stray field). The error budget related to the attitude determination translated to ~ 4 nT (rms), taking into account the angular uncertainties from the star cameras (~ 10 arc sec) and from the ATS (7 arc sec). There was also an error budget of 1.5 nT associated with the position determination of the spacecraft. The overall performance measured in orbit depended on the use of the star cameras and the sun sensor for attitude determination; small inconsistencies resulted in occasional small discontinuities in the data. The in-flight calibration of the measurements effectively confirmed the pre-flight expectations (Lancaster et al. 1980). The near-polar, sun-synchronous orbit allowed a complete latitudinal coverage, but within a restricted range of magnetic local times that needed to be taken into consideration for the analysis of the data. Magsat, as a dedicated mission to survey the geomagnetic field was successful in providing high precision data to extend the harmonic terms of the Earth's magnetic field and the calibrated data collected the mission remained the basic data set until the Ørsted and CHAMP missions, 20 years later, came to provide new and more extensive data.

The Ørsted satellite was launched on 23 February 1999 into a near-polar orbit of inclination 96.5°, with a perigee of 638 km and an apogee of 849 km. Contrary to the fixed local

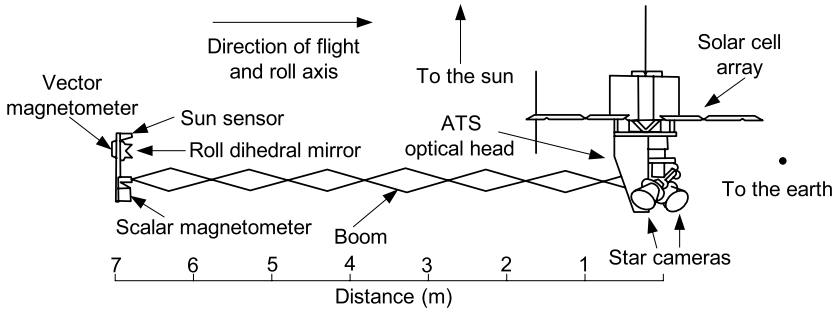

Fig. 35 Sketch of the Magsat spacecraft in flight configuration, with the boom that carried the scalar and vector magnetometers extended

time sun synchronous orbit of Magsat, the orbit of Ørsted drifted in local time by ∼0.46 hours per standard month. This allowed a survey of local times over the mission and several studies of the local-time dependent external contributions (such as ionospheric currents). It was equipped with a scalar and a vector magnetometer. The magnetometers were mounted on an 8 m boom, with the scalar at the boom tip and the vector fluxgate sensor at ∼2 m inboard. The Overhauser scalar magnetometer (for its operating details, see Kernevez and Glénat 1991) as used on Ørsted was described by Duret et al. (1995, 1996). The operation of the Overhauser magnetometer is based on proton Larmor precession, the Larmor frequency is proportional to the magnetic field strength. The measurement range of the Overhauser scalar magnetometer was 16,000 to 64,000 nT with a resolution of 0.1 nT and an absolute accuracy ∼0.5 nT. The absolute magnitude measurements were used to calibrate the measurements by the vector magnetometer.

The vector magnetometer on Ørsted was a new development (Nielsen et al. 1995). It was a triaxial fluxgate sensor, using for its magnetic core material, for the first time, a metallic glass, instead of the more conventional crystalline permalloy type magnetic alloy (Nielsen et al. 1991). This material was developed to make the sensors less sensitive to acoustic vibrations and mechanical deformations. Additional heat treatment reduced the hysteresis of the material to close to zero. The single sensor assembly, consisting of the toroidal core with the tape of metallic glass material, the drive winding around the core and a sense or pickup winding on a rectangular former was of classical design. The three orthogonally mounted single axis sensors, however, were enclosed in a spherically mounted three-axis coil system that provided the feedback to null the field at the sensor assembly (Primdahl and Jensen 1982). The vector magnetometer sensitivity was limited by the sensor noise (∼15 pT rms in the bandwidth 0.06–10 Hz). With a typically $1/f$ noise spectrum, this corresponded to ∼6 pT/Hz$^{1/2}$ at 1 Hz. The operating range of the instrument was ±65,536 nT; using an 18-bit analogue-to-digital converter this corresponded to a resolution of 0.5 nT. The bandwidth of the instrument was set at 250 Hz. Its temperature stability was better than 1 nT in the range −20° to +60°C.

A key component of the magnetic field instrumentation is its association with a star camera, the Advanced Stellar Compass (ASC) that enables the absolute attitude to be determined to the required accuracy (Jørgensen et al. 1997). The ASC and the vector magnetometer were mounted on a common optical bench on the spacecraft boom. This solution, different from that implemented on Magsat, had a requirement to enable the vector magnetometer to achieve an attitude determination accuracy of ∼20 arc sec per axis. The ASC differed from more standard star trackers by the way it transferred the image on its CCD camera to

a Data Processing Unit which used the Hipparcos star catalogue as a stored data base for establishing the exact pointing attitude of the ASC and hence the optical bench on which the vector magnetometer was mounted. An important feature of the ASC was its close to zero stray magnetic field, so that it was possible to co-mount it with the vector magnetometer.

An Argentinean satellite, SAC-C, in cooperation with NASA, was launched on 21 November 2000 into a circular sun-synchronous polar orbit of height ∼700 km, with equator crossing (local) times of 10:15 and 22:30 (Colomb et al. 2004). The satellite carried a magnetic field investigation package similar to that of Ørsted, with a vector-compensated vector fluxgate magnetometer, co-mounted on an optical bench with an ASC, both identical to the instrument on Ørsted. The scalar magnetometer was, however, a scalar helium magnetometer, a model identical to that flown on Cassini (Smith et al. 2001). However, the ASC failed to function in orbit and therefore the attitude information that can be used with the vector data are not sufficiently accurate for precise measurements of the Earth's magnetic field. The scalar magnetometer was shown to be accurate to better than 2.5 nT; however, there were concerns that the stray field of the complex spacecraft may affect the measurements and these cannot meet the target of 1 nT accuracy. However, by cross-calibrating between CHAMP (see below) and Ørsted on the one hand and SAC-C on the other when the spacecraft came sufficiently close in orbit, the SAC-C data could be sufficiently calibrated to enable their use in conjunction with the other two spacecraft.

The Ørsted satellite was a significant success and contributed a large amount of data for the very detailed study of the earth's magnetic field (Olsen 2002; Mandea 2006). Only a year and a half after the launch of Ørsted, the German CHAMP satellite was launched on 15 July 2000 into near-circular orbit of initial altitude 454 km, with a near-polar inclination of 87° (Reigber et al. 2002). (By December 2009, the altitude of the orbit decayed to ∼300 km.) Similarly to Orsted, CHAMP's orbit was not sun-synchronous (at constant local time) but it advanced one hour in local time within eleven days, thus was able to cover all local times. In order to ensure a longer duration for the mission, while retaining an altitude less than that of Ørsted, the spacecraft was made deliberately heavy (522 kg) and a small along-track cross section to minimize atmospheric drag. The mission was dedicated to measuring the Earth's gravitational field as well as its magnetic field. The satellite carried a very similar magnetic instrument package to Ørsted on a 4 m boom: an Overhauser scalar magnetometer of identical design and construction to that flown on Ørsted, two vector fluxgate magnetometers (for redundancy and gradiometry) identical to the one on Ørsted, and an Advanced Stellar Compass with two optical heads, one each for the two vector magnetometers, but with a common Data Processing Unit. Because of the possible magnetic interference from the vector feedback system with the operation of the Overhauser scalar sensor, the two sensor systems were mounted at a distance of about 2 m from each other along the boom. The fluxgate sensors were rigidly mounted on an optical bench with the ASC optical heads; this provided a mechanical stability better than 10 arc sec. (Another dual-head ASC was used in the spacecraft for attitude control.)

The vector magnetometer, although using identical sensors to Ørsted, had a higher resolution (24-bit ADC, 10 pT/bit). The noise level was stated to be $<$100 pT (rms), with a linearity of the same order and an offset drift about 0.5 nT. The sampling rate was 50 Hz, but several different data schemes could be used, employing both data compression and reduced sampling rates. The high quality of the measurements, combined with an orbit lower than that of Ørsted, enabled CHAMP to contribute to investigate both new current-related phenomena in the ionosphere (Lühr et al. 2002) and new details of the Earth's magnetic field, in particular its lithosphere (Maus et al. 2002). CHAMP, combined with Ørsted, have made the current greatly refined model of the Earth's magnetic field possible (Olsen et al. 2009), thanks to the unexpected longevity of these missions.

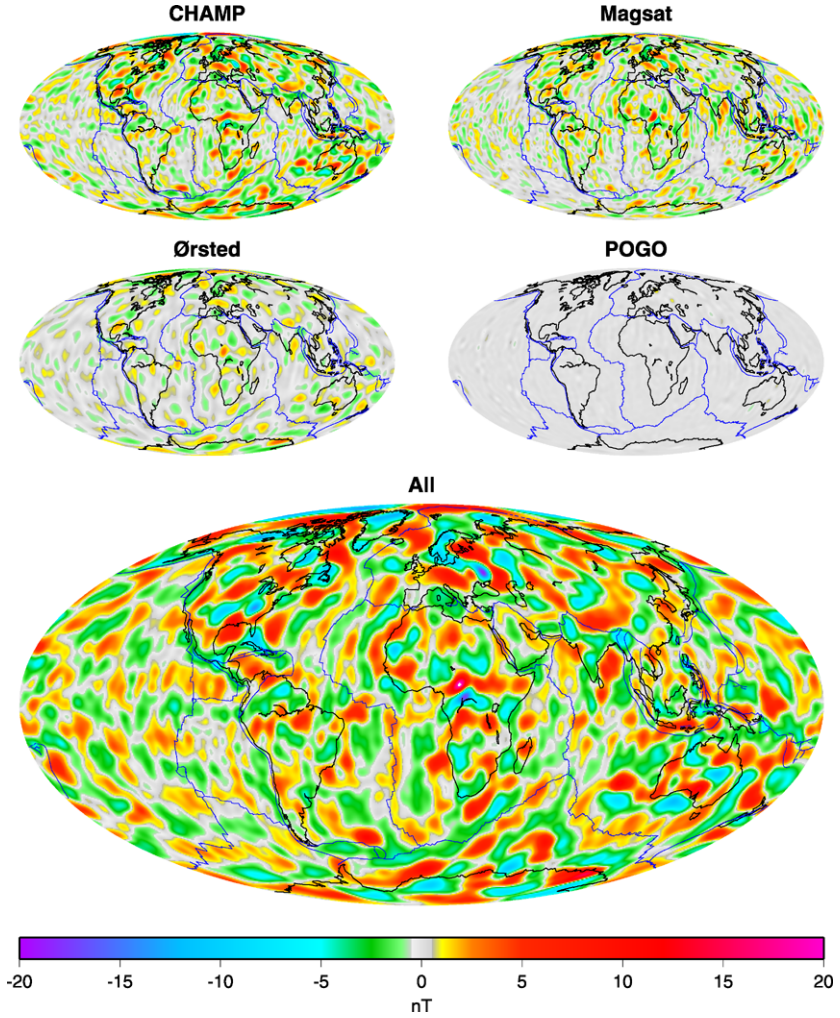

Fig. 36 Using a comprehensive model of the Earth's magnetic field, the graphs show the portion of the radial component of the lithospheric magnetic field at 400 km altitude as resolved by the satellites CHAMP, Magsat, Ørsted and POGO. Using all data, the resolution and coverage of the lithospheric field is greatly increased. The major tectonic boundaries are also shown for reference (from Sabaka et al. 2004)

Remarkable progress has been made in collecting large amounts of data to model not just the Earth's main magnetic field, but its lithospheric field as well as several aspects of the (variable) external contributions. The improvement that has been possible from combining data from all dedicated terrestrial magnetic field missions is illustrated in Fig. 36. However, further progress requires a simultaneous and coordinated set of measurements at several locations. In particular, simultaneous coverage at different longitudes is necessary for separating the terms that vary as a function of local time. The next major mission to study the Earth's magnetic field is ESA's three-spacecraft SWARM, to be launched in 2012 (Friis-Christensen et al. 2006, 2008). Two of the spacecraft, SWARM-A and -B will be in identical orbits, at ∼450 km height, but separated in longitude by ∼1°. The third, SWARM-C will be

in a higher orbit (∼530 km initially) with the right ascension of the ascending node close to the other two satellites.

The three spacecraft will have a shape and layout similar to CHAMP. The magnetic field instrumentation will also be similar (Merayo et al. 2008). There will be a single vector fluxgate magnetometer with vector feedback in a spherical configuration as for Ørsted and CHAMP, with redundant electronics and performance figures comparable or better than previous comparable missions. The magnetometer will be mounted together with the Advanced Stellar Compass star camera on an optical bench. Three orthogonally mounted optical heads will be used to minimise attitude errors affecting the vector measurements. In addition, the sensor itself will be mounted at a distance ∼40 cm from the ASC heads to minimise further the stray fields at the location of the vector magnetometer. The absolute magnitude of the magnetic field is measured by two optically pumped helium 4 scalar instruments. Compared to the Overhauser magnetometer used on Ørsted and CHAMP, the helium magnetometer offers reduced noise (higher sensitivity, ∼1 pT/Hz$^{1/2}$), an absolute accuracy ∼0.1 nT and a much higher rate of measurements (in principle several hundred Hz).

3.5 The Moon

The Moon belongs to the family of terrestrial planets by association and its magnetism can be considered in the same terms as those of the terrestrial planets. While it was discovered early that the Moon has no global scale, internally generated magnetic field (none was expected), the weak but still significant magnetic fields that have been observed have many important implications for models of its early history, particularly its cratering history, and its material properties.

The first mission to reach the Moon, the Soviet Luna 2, was launched on 12 September 1959 and crashed on the surface two days later. The data returned showed that the Moon was non-magnetic, with a relatively crude upper limit for its surface field of ∼100 nT. The instrument sensor itself, of the fluxgate type, was placed on a boom protruding from the spacecraft (see Fig. 37). The previous mission attempt, Luna 1 that flew by at a distance of 6000 km from the Moon also carried an identical magnetometer, except that the measurement range for Luna 1 was ±3000 nT, while it was reduced to ±750 nT for Luna 2 that also had a digitization uncertainty of 12 nT and an offset/background between 50 and 100 nT. The null result from the instrument was thus compatible with an upper limit of 100 nT as the Moon's magnetic field.

There were several other Luna missions in the early to mid-1960s, but no definitive value was found for the lunar magnetic field, in fact not even any evidence of its existence but only upper limits, due to a combination of relatively high orbits and the sensitivity of the magnetometers. This was reported by Dolginov et al. (1966) for the Luna missions up to Luna 10 and by Sonett et al. (1967) and Ness et al. (1967) based on the findings of the first NASA lunar orbiter Explorer 35 that carried two magnetometers. The Explorer 35 magnetometer operated into the Apollo era when, as described below, it was used in conjunction with the lunar Surface Magnetometers to investigate induction effects in the planetary body and thereby to deduce the electrical properties of the Moon's interior. A revisit of the observations following the first Moon landings also allowed an interpretation of some of the variability observed on the far side of the Moon to be ascribed to patchy but strong crustal magnetization (Mihalov et al. 1971).

The first evidence for remnant magnetisation was found in the lunar samples returned by the Apollo 11 astronauts in July 1969 (see, e.g., Runcorn et al. 1970 and the retrospective review by Fuller 1998). More such evidence was collected from the samples brought

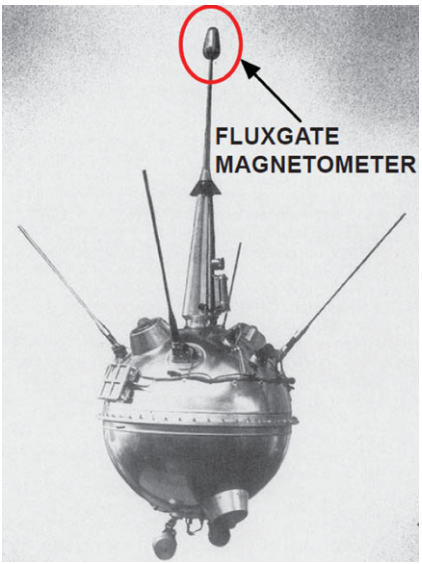

Fig. 37 A photo of the Soviet Luna 2 spacecraft that was the first to reach the Moon in 1959; this mission showed that, as expected, the Moon did not have a significant global magnetic field. The instrument and impact orbit did not allow for the detection of the crustal magnetic field signatures identified on the Moon during Apollo programme and later missions

back by Apollo 12 (Runcorn et al. 1971) and subsequent Apollo missions. (Some of the interpretation of the early evidence for the presence of magnetised material in the samples was controversial, see Fuller 1974.) However, direct evidence of the magnitude of the surface field was obtained through the use of the first lunar surface magnetometer delivered by Apollo 12 (Dyal et al. 1970a). Using similar surface magnetometers on subsequent Apollo missions described by Dyal et al. (1974) around the landing sites provided data that confirmed the existence of crustal magnetism. The surface magnetometers found a variable level of natural remnant magnetisation. There is uncertainty even today whether the magnetisation is compatible with models of the Moon's core that could operate an early dynamo in its history. Additionally, particles and fields sub-satellites for Apollo 15 and 16 measured magnetic fields in orbit which supported the overall picture of non-uniform crustal magnetisation with a hint of trends related to cratering combined with an induced magnetic field in the lunar interior that is by definition highly variable.

The Lunar Surface Magnetometers and the way they were used have been described by Dyal et al. (1970b) and Dyal and Gordon (1973). The basic design of the static magnetometers used on the Apollo 12, 14, 15 and 16 missions was the same, although detailed improvements were made from mission to mission. Portable magnetometers were also carried on the Apollo 14 and 16 missions. The Apollo 16 static magnetometer fluxgate sensors used a new design based on highly stable ringcores. This development by the US Naval Ordnance Laboratory of the special high-permeability material for the fluxgate sensors with low intrinsic noise when used in a magnetometer, the construction of the sensor itself with its coil formers and drive and sense windings was to bring a general improvement in magnetometer performance for all space applications. Indeed this sensor, as described by Gordon and Brown (1972) was to be a template for fluxgate magnetometers for the next three and a half decades; most of these used the same high permeability magnetic tape from the material developed by the Naval Ordnance Laboratory on the ringcores.

In the light of later developments of operating fluxgate sensors, it is interesting to note that the sensor was driven by a 6 kHz constant voltage sine wave. (In the lunar portable magnetometers used on Apollo flights 14 and 16, the drive waveform was a constant voltage

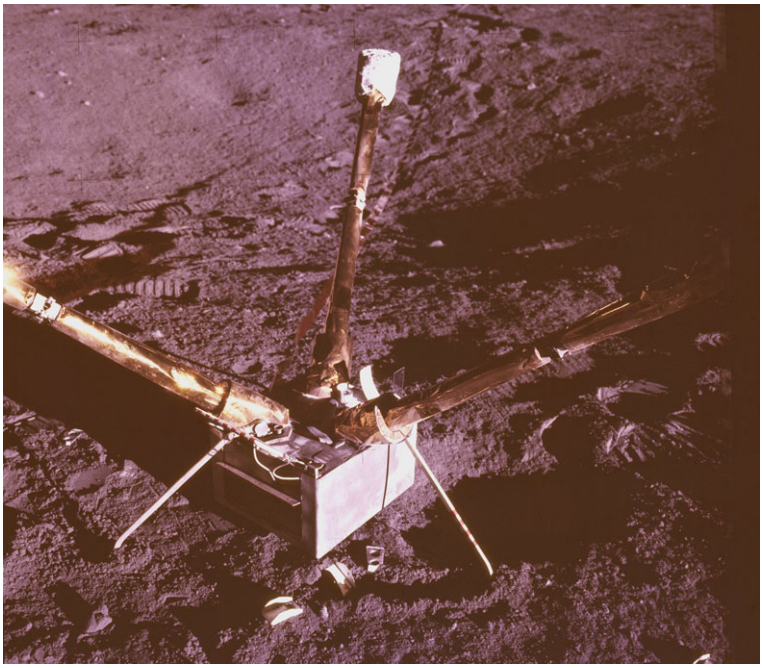

Fig. 38 The Lunar Surface Magnetometer deployed on the Moon by the astronauts of the Apollo 12, 14, 15 and 16 missions. These magnetometers first measured the steady crustal magnetization of the Moon but that was found to be highly variable from site to site (photo: NASA)

square wave.) The signal from the pick-up or sense coil did not contain the fundamental of the drive frequency because of the orthogonal geometry of the winding and it was the second harmonic and its phase with respect to the drive waveform that was used for measuring the ambient field component magnitude and sign. In later fluxgate sensors, the drive waveform used routinely is approximately a shaped bipolar exponential current waveform.

The three single axis sensors were located on separate booms of about 1 m each that formed an orthogonal triad. The sensor booms were oriented at an angle approximately 35° from the lunar surface. In order to reference the measurements in lunar coordinates, the magnetometer assembly was aligned with its Z axis to the East by an astronaut using a shadowgraph, the X sensor arm was aligned to the Northwest, and the Y sensor made up the right-handed orthogonal triad. In addition, level sensors were used to determine the orientation of the assembly with respect to the horizontal plane. Each sensor had thermally operated flippers that rotated the sensors by 90° to calibrate the zero levels. The magnetometers were built for operation for one year and were remotely operated from the Manned Spacecraft Center, Houston. The overall accuracy was $\sim$1° in lunar coordinates. The field values measured by the static lunar magnetometers were 38 nT, 103 nT, 3 nT and 327 nT, respectively from the four missions. A photograph of the setup of the Lunar Surface Magnetometer is shown in Fig. 38.

Results from the observations by the magnetometers on the Apollo sub-satellites 15 and 16 provided a detailed and convincing view of the crustal magnetisation of the Moon and induction effects in its interior (Coleman et al. 1972, 1972b). The sub-satellites were released from the Apollo Service Module in Moon orbit intended for a nominal mission duration of one year. The first was launched into a low eccentricity first orbit 102 km × 139 km, but with

rapidly changing orbital parameters because of gravitational perturbations. The second was placed in a similarly low orbit; the decay of the orbit to low altitudes above the lunar surface allowed some detailed mapping of anomalies in crustal magnetisation and associating these with surface/geological features (see, e.g. Hood et al. 1979). Combining the in-orbit data from Explorer 35 and the data from the surface, it was possible to estimate parameters of the induction caused in the lunar crust by sudden changes in the interplanetary magnetic field. One such simultaneous set of observations is shown in Fig. 39.

There were identical magnetometers on the two sub-satellites. The design was a two-axis fluxgate. One of the sensors was aligned with the spin axis of the spacecraft, the other was aligned in the spin plane. The spin rate was ∼12 rpm; demodulation of the spin-plane sensor provided the direction and magnitude of the spin-plane component of the magnetic field (Coleman et al. 1972). The observations made by the magnetometers of the nature and geological distribution of crustal magnetism formed the historical data base for lunar magnetic fields for 25 years.

A powerful technique for the study of small-scale planetary crustal magnetic fields was developed using the energetic electron instrument on the two Apollo sub-satellites (Anderson et al. 1972). The technique, named Electron Reflectometry, is based on the effect of localized magnetic fields on the pitch angle distribution of energetic electrons that are reflected from close to the planetary surface by the crustal field concentrations (Anderson et al. 1974; Howe et al. 1974). This technique was used for matching the fine-scale magnetic crustal anomalies detected by the sub-satellites' magnetometers to the geological formations of different structures, origins and ages (McCoy et al. 1975; Lin et al. 1976). The applicability of the technique to both the lunar and Martian crustal magnetisation was exploited on the Lunar Prospector and Mars Global Surveyor mission which both flew magnetometer—electron reflectometer combinations.

After the first decade of space missions to the Moon in the Apollo era, there was a hiatus of more that 25 years before a magnetometer-carrying spacecraft again visited the Moon. One of NASA's Discovery missions, Lunar Prospector was launched on 6 January 1998 and reached a circular lunar polar orbit at a height of 100 km above the surface on 11 January 1998. The orbit had to be restored periodically, because of its degradation due to gravitational perturbations. After one year, the orbit was lowered to a much lower, 15 km (minimum) and 45 km (maximum) height orbit. On 31 July, 1999, the spacecraft impacted the lunar surface, ending the mission.

Magnetic fields were measured by a magnetometer—electron reflectometer combination similar to the one used on Mars Global Surveyor and also following the serendipitous discovery of the technique based on the Apollo 15 and 17 sub-satellites observations (Howe et al. 1974). The two instruments were mounted on a 2.5 m boom, with the magnetometer sensor (a tri-axial fluxgate) on an additional 0.8 m extension arm outboard of the reflectometer. Given the polar orbit of the spacecraft and the relatively long duration of the mission, very comprehensive mapping of the lunar crustal magnetic fields could be achieved (Halekas et al. 2001; Hood et al. 2001; Mitchell et al. 2008). The most recent work (Richmond and Hood 2008) has used a considerable amount of data from the low-altitude, 30 to 40 km, phase of the Lunar Prospector mission, in particular 329 passes at the nightside and the terminator that are best suited for analysis without solar wind and other background effects, to generate detailed maps of the crustal anomalies. The low altitude Lunar Prospector observations have also made possible an evaluation of the very weak internal magnetic field of the Moon (Purucker 2009) that can be applied to refine the model of the lunar interaction with the solar wind.

The latest mission to the Moon was the Japanese Kaguya (Selene), launched on 14 September 2007. It was placed initially into a circular polar orbit on 18 October 2007 at an

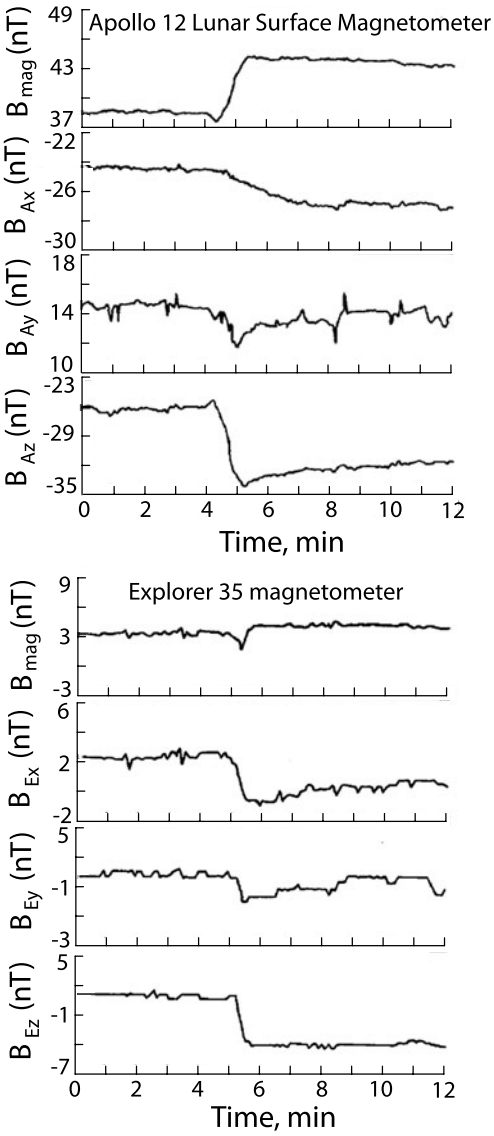

Fig. 39 Simultaneously measured magnetic field variations at the Apollo 12 landing site by the Lunar Surface Magnetometer (*upper panels*) and at Explorer 35 in orbit around the Moon (*lower panels*). The measurements start on 8 December 1969 at 13:38 UT. The large amplitude angular discontinuity at Explorer 35 at about 5 minutes after the start of the measurements caused a variation in the field measured by the LSM that is superposed on the steady ∼38 nT crustal field background (from Dyal et al. 1972a)

altitude of 100 km for a 10-months long operational phase, followed by a mission extension that came to an end on 11 June 2009 when the spacecraft was deorbited to impact the Moon. Kaguya carried a magnetometer that had been very carefully calibrated (Shimizu et al. 2008), and a long, 12-m magnetometer boom that was successfully deployed after launch. The Lunar Magnetometer (LMAG) is a triaxial fluxgate sensor of classical construction. The frequency range of the instrument is limited to 10 Hz and a 32 Hz sampling rate. The accuracy of the measurements is better than 0.1 nT. It has four operating ranges, ±64 nT, ±256 nT, ±1024 nT, and a range that had been used for ground testing before launch, in the Earth's field. A special feature of the in-flight calibration of the instrument is the use of two orthogonal coils near the boom root that generate calibrated 2 nT fields at

the location of the sensor at the boom tip, similar to the coils used on the Cassini spacecraft described in Sect. 4.2. (The Voyager spacecraft had a single calibration coil at its magnetometer boom root.)

Preliminary results of the magnetic field mapping and the modelling of the data were reported by Shibuya et al. (2008). It is expected that following this development of the methodology for assessing the crustal fields, the observations of Kaguya will add further data to resolve the problems raised by the complexities of lunar magnetism. (The Lunar Reconnaissance Orbiter of NASA, launched in 2009, does not carry a magnetometer.)

3.6 Comets and Asteroids

Comets are not expected to have magnetic fields, but the outgassing that occurs in a complex manner as comets approach the sun during their perihelion passage creates a complex plasma-magnetic field environment as the cometary material interacts with the ambient solar wind flow. Studying this complex and dynamic environment is primarily of interest for learning more about comets. So far four comets have been visited by spacecraft equipped with magnetometers: 21P/Giacobini-Zinner in 1985 (Smith et al. 1986), 1P/Halley's comet in 1986 (Neubauer et al. 1986; Riedler et al. 1986a; Saito et al. 1986), 26P/Grigg-Skjellerup in 1992 (Neubauer et al. 1993) and 19P/Borelly (Glassmeier et al. 2007b). The magnetometer on the ISEE-3/ICE mission that flew by Giacobini-Zinner in 1985 was a Vector-Helium magnetometer that has already been described (Frandsen et al. 1978). The two spacecraft that flew close to Halley's comet in 1986 were ESA's Giotto and the Soviet Vega spacecraft, both equipped with fluxgate magnetometers (Neubauer et al. 1987; Riedler et al. 1986b). The Giotto magnetometer sensors were mounted very close to the spacecraft body and in particular to the despin motor of the antenna that was made to point at Earth on the spinning spacecraft. The data were contaminated by the spacecraft's stray magnetic fields; however, extensive and careful assessment of the noise background has led to valuable science data and results concerning the comet's environment. The Vega magnetometer consisted of a triaxial fluxgate sensor mounted on a boom at the end of the extended solar panels, and another, single axis fluxgate about 1 m inboard, used as a gradiometer to resolve the spacecraft-generated background field at the outboard sensor. The Vega magnetometer was closely similar to the instruments flown on the Venera 13 and 14 missions to Venus. After the Halley encounter, the Giotto spacecraft was redirected to make a close flyby (at only 200 km) of comet 26P/Grigg-Skjellerup in 1992. The magnetometer and the plasma instrumentation had survived the encounter with Halley and provided valuable data about the plasma environment of this comet (Glassmeier and Neubauer 1993). A further cometary flyby, within a distance of 2200 km, was carried out by NASA's Deep Space 1 mission on 22 September 2001. The target comet was 19 P/Borelly.

The dedicated comet rendezvous mission of ESA, Rosetta, was launched in 2004 and will reach Comet 67 P/Churyumov-Gerasimenko, after a 10-year complex trajectory, in 2014 (Glassmeier et al. 2007c; Schulz 2009). The spacecraft will then be captured into an orbit at about 25 km height around the comet and will accompany it on its journey towards perihelion. A five-instrument plasma science package includes a magnetometer (Glassmeier et al. 2007b) for the study of the plasma environment and its dynamical processes through the developing activity phase of the comet. Rosetta also carries a lander that will be released from the main spacecraft bus once a suitable landing site has been identified. The lander carries a miniature magnetometer that will measure the magnetic field during the descent and also on the surface to try and identify the structure of the comet's remanent magnetisation, if any (Auster et al. 2007). In addition, coordinated measurements between the magnetometers on the orbiter and lander under changing interplanetary magnetic field conditions can

be used, as was done for the Moon (Dyal et al. 1972b, 1974) to study the conductivity of the comet nucleus.

Asteroids represent a vast population of objects presenting a very great variety in terms of size, origin, and material composition. Learning more about the material properties of asteroids, in particular though their magnetic properties is important for better understanding the formation of the solar system. The magnetism of asteroids can only be measured in situ, on a sufficiently close flyby or by an orbiter and/or lander. There have been a number of serendipitous asteroid flybys over the past two decades that have resulted in an interesting set of properties. Of the three asteroid-focussed missions flown so-far, only NASA's NEAR to 433 Eros, launched on 17 February 1996, carried a magnetometer (Lohr et al. 1997; Acuña et al. 1997). Japan's Hayabusa launched on 9 May 2003 to asteroid 25143 Itokawa and NASA's Dawn mission to the largest asteroids, 1 Ceres and 4 Vesta, launched on 27 September 2007 do not carry a magnetometer. This is particularly disappointing for the Vesta flyby, as it appears to be an evolved body with, potentially, an important magnetic signature.

The Galileo spacecraft, on its way to Jupiter, flew by two asteroids. The first was 951 Gaspra, on 29 October 1991, at a closest approach distance of 1600 km; the second was 243 Ida, on 28 August 1993, at a distance of 2400 km. The Galileo magnetic field investigation already described in Sect. 4.1 (Kivelson et al. 1992) carried out measurements during both flybys, to study the interaction of the asteroids with the interplanetary medium and to detect any intrinsic magnetic field. The flyby of Gaspra yielded a surprising result: the surface magnetic field value deduced from the signature of the magnetosphere-like interaction was commensurate with that of the earth (Kivelson et al. 1993). The asteroid is classed as an S-type, potentially within a family of the parent bodies of stony-iron meteorites (covered, probably, by regolith). The magnetic field measurements were consistent with this interpretation, yielding a magnetic moment per unit mass characteristic of iron meteorites and highly magnetized chondrites. This also supports the hypothesis that Gaspra is a fragment of a previously differentiated and magnetised parent body. Measurements during the flyby of Ida did not imply an intrinsic magnetic field, but signatures of the interaction of the asteroid with the solar wind were still noted in the data. A comparison of the different signatures at Gaspra and Ida have been investigated and interpreted as whistler waves generated by the interaction of the asteroids with the solar wind (Kivelson et al. 1995).

NASA's Deep Space-1 mission, a technological demonstrator for an ion drive orbital booster, flew by asteroid 9969 Braille on 29 July 1999, at a closest approach distance of only 28 km, on the night side of the asteroid. Although the magnetic signature needed to be recovered from a very noisy background (the magnetometer was primarily included as a diagnostic sensor for the ion engine), there remained a significant residual signal that could be associated with the asteroid. The two miniature tri-axial fluxgate sensors included in the spacecraft were in fact the prototypes of the sensors used for the Rosetta cometary mission, described above (Glassmeier et al. 2007b). The magnetic signal has been interpreted as evidence for an intrinsic magnetic field, with an upper limit value for an equivalent dipole moment of 2.1×10^{11} Am^2 (Richter et al. 2001).

The Cassini approach to asteroid 2685 Masursky on 23 January 2000 was not suited to observing any aspect of its interaction with the solar wind, as it occurred at 1.5 million km from the asteroid. On June 27, 1997 the NEAR spacecraft passed within 1200 km of main belt asteroid 253 Mathilde, a C-type asteroid. No magnetic signature was observed during the flyby that could have been attributed to the asteroid.

The prime objective of the Near-Earth Asteroid Rendezvous (NEAR) mission of NASA was the asteroid 433 Eros. NEAR was launched on 17 February 1996. There were several close orbiting phases, at 200 km, 50 km and 35 km heights. Eventually, the spacecraft

touched down on Eros 12 February 2001. Contrary to the other S-type asteroids (Gaspra, Braille) that had been found to have a magnetic field, Eros was found to be completely unmagnetised (Acuña et al. 2002). The result is robust as the NEAR magnetometer was extensively calibrated in flight (Anderson et al. 2001). The interaction of Eros with the ambient solar wind was also found to be devoid of any signature that may have indicated the presence of a magnetic field (Anderson and Acuña 2004).

The Rosetta mission includes two asteroid flybys (Barucci et al. 2007); the first with the rare E-type 2867 Steins has already taken place on 5 September 2008 (Auster et al. 2010). The flyby with the much larger (∼100 km) C-type 21 Lutetia is expected on 10 July 2010. C-type asteroids are considered to be the most primitive type that had not undergone heating or differentiation. Consequently, no magnetic signature is expected during the flyby, although the magnetometer will make measurements in the asteroid environment.

4 The Outer Planets

4.1 Jupiter and Its Moons

Analysis of radio emissions from Jupiter that were first detected from Earth (Burke and Franklin 1955) indicated that the source of the radio waves was emission by energetic charged particles in a strong magnetic field. This implied a large planetary scale magnetic field as exists for the Earth, except much stronger. The radio measurements and their implications in terms of the magnetic field of Jupiter have been reviewed by Berge and Gulkis (1976) and Smith and Gulkis (1979). However, the details of the field (magnitude, dipolar or higher order polarity, direction of axes) needed confirming to establish its origin and, in general, the internal structure of the planet.

The first spacecraft to fly by Jupiter and measure its magnetic field was Pioneer 10 (see the spacecraft in Fig. 1 in the Introduction). It was launched on 3 March 1972 and flew by Jupiter on 3 December 1973. The identical Pioneer 11 spacecraft was launched on 6 April 1973 and reached Jupiter on 4 December 1974. Pioneer 11 was targeted to Jupiter in such a way that the flyby would redirect it to a close flyby of Saturn that took place on 1 September 1979. After the planetary flybys, the trajectories of both Pioneer 10 and 11 were directed to the outer heliosphere; both remained operational into the 1990s.

The magnetometer sensors were carried on a boom of 6.6 m from the main body of the spacecraft. The primary instruments on both missions were high sensitivity Vector Helium Magnetometers (Smith et al. 1975a) that have been described in Sect. 2.3. Pioneer 11 also carried a vector fluxgate magnetometer designed for measuring the high fields in the vicinity of Jupiter and Saturn (Acuña and Ness 1975a, 1975b). The results from the magnetometer of the first flyby were reported by Smith et al. (1974a, 1974b) and the second flyby by Smith et al. (1975b) and Acuña and Ness (1976). The Pioneer results were reviewed by Smith et al. (1976). Plots of the magnetic field magnitude from the two Pioneer flybys measured by the VHM, together with the jovicentric distance during the flybys, are shown in Fig. 40. Models of Jupiter's very large internal magnetic field were published by the same authors, although differences were reported between the model based on the VHM and High Field FGM data.

The radio measurements that implied much higher magnetic field values at Jupiter than at the Earth set a requirement for a broader measurement range than for near-Earth missions. For the magnetometers on missions to Jupiter the expected maximum field was of order of several Gauss, or of order of m T. At the same time, the interplanetary magnetic field at the orbit of Jupiter that needed to be measured was of order of 1 nT. So a measurement range

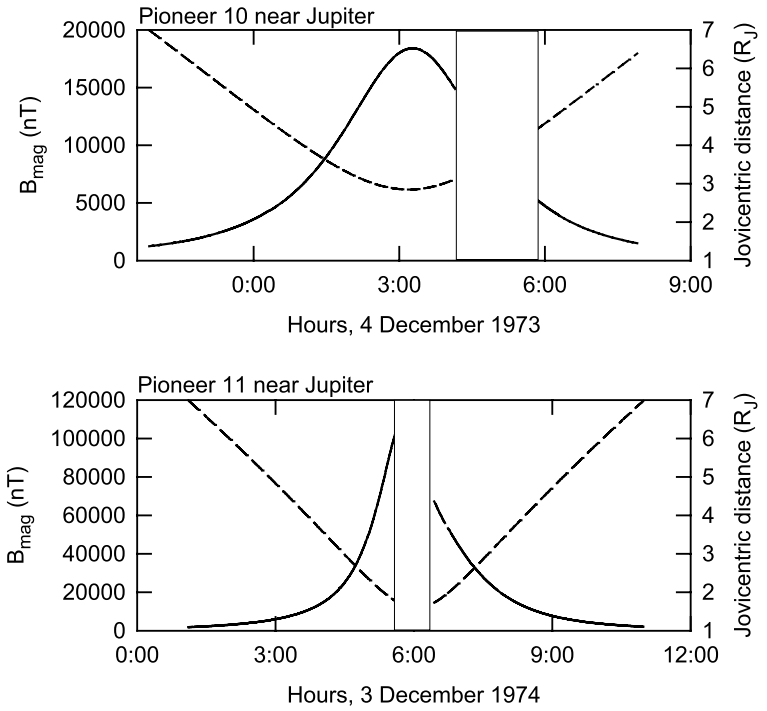

Fig. 40 The magnetic field intensities measured by the Vector Helium Magnetometer during the hours of closest approach to Jupiter during the flybys of Pioneer 10 and 11 (*solid lines*) and the jovicentric distance of the spacecraft (*dashed lines*). *The blanked out* intervals correspond to the two spacecraft being occulted from the Earth by the planet on the two flybys. The closest approach distances were $2.84R_J$ for Pioneer 10 and $1.62R_J$ for Pioneer 11. For Pioneer 11, the closest approach occurred during the occultation interval

covering about 6 orders of magnitude was needed. The VHM designed for Pioneers 10 and 11 had eight ranges, from ±4 nT per vector component to ±140,000 nT (Smith et al. 1975a). Switching between the ranges was either automatic or manual, the mode being selected by ground command. The digital resolution was determined by the 9-bit Analogue-to-Digital Converter (ADC) that included 1 bit for the sign of the signal; thus for the ±4 nT range the resolution was 0.016 nT, while in the highest range it was 547 nT. As shown in Fig. 40, the maximum field measured and telemetered from Jupiter by Pioneer 11 was about 110,000 nT, so that the relative accuracy of the measurements close to Jupiter was about 0.5%. It was this instrument that, developed from the early Mariner 4 and 5 magnetometers using improved electronic components and adapted to the different mission requirements, was to be used on the ISEE-3/International Cometary Explorer mission, on Ulysses and on the Cassini Saturn Orbiter.

The fluxgate magnetometer that was carried on Pioneer 11 was a unique design for that mission that was severely limited in resources as a late addition to the payload (Acuña 1974; Acuña and Ness 1975a, 1975b). It shared its resources with an experiment that measured cosmic rays and was mounted on the spacecraft experiment platform, rather than at the boom tip as the VHM. Because of the expected high fields at Jupiter, the instrument was operated, uniquely for a spacecraft FGM, in open rather than in closed loop, so that there was no attempt to null the field at the location of the sensor. The instrument, in addition, used only two ringcore sensors, but each of these was designed to measure two orthogonal components

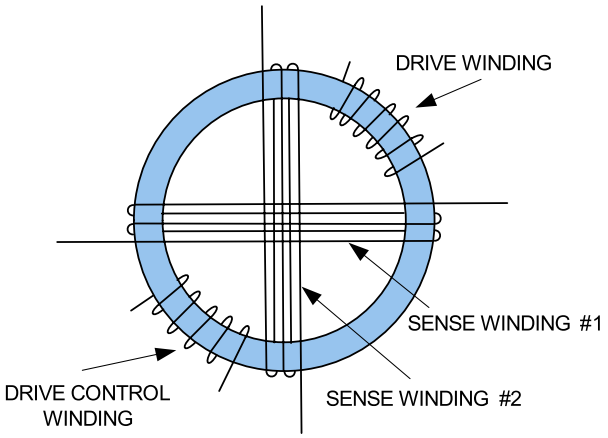

Fig. 41 Schematic arrangement of the ringcore sensor used on the High Field FGM on Pioneer 11. The sensor used two orthogonal sense windings so that the same ringcore could be used to measure two components of the magnetic field vector, thus making it possible to measure the three components of the magnetic field with two such sensors mounted orthogonally to each other (after Acuña 1974)

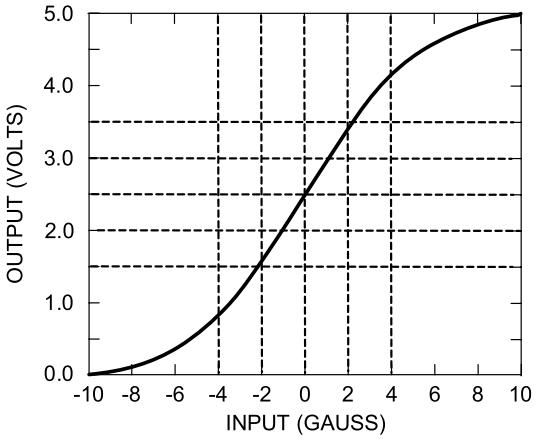

Fig. 42 Response function of the open-loop High Field FGM used on Pioneer 11. The output has adequate linearity below about 200,000 nT (after Acuña 1974)

of the ambient magnetic field by the use of two orthogonally placed sense windings as illustrated in Fig. 41 (Acuña 1974). The measurement range for each component was 1 mT (10 Gauss), with a resolution of 1 μT. It was thought that the spacecraft background at the body-mounted location of the sensor was less than that value; the two sensors needed for the vector measurements were in fact mounted as an integral part of the electronics box. As the sensors are operated without feedback, the response function (in terms of the voltage output for a given magnetic field) is in principle inherently non-linear; however, as illustrated in Fig. 42, for input fields less than about 200,000 nT (2 Gauss), the instrument was considered to be adequate given its resolution.

The two-component measurement geometry of the two ringcore sensors was arranged such that one of the sensors had sense windings along the X and Z axes, the other along the Y and Z axes, with the second Z axis signal (called Z_R, for redundant) not being processed by the instrument's own ADC, but by that of the spacecraft. The first analysis of the Jupiter flyby using the High Field FGM (Acuña and Ness 1975b) indicated that, contrary to the Pioneer 10 flyby analysis by Smith et al. (1974b), there were very large quadrupole and octupole moments in Jupiter's main magnetic field. However, a later analysis of the measurements by the redundant Z_R sensor through the spacecraft ADC indicated that a 10%

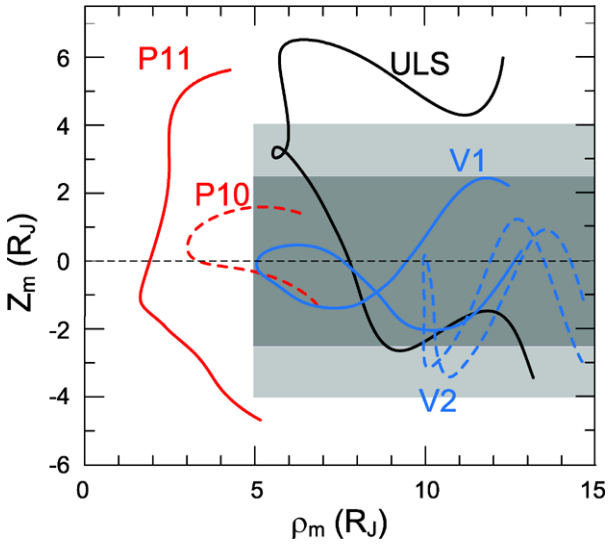

Fig. 43 The trajectories of the five spacecraft that made magnetic field measurements near their closest approach to Jupiter (P10 and P11 = Pioneer 10 and 11, V1 and V2 = Voyagers 1 and 2, ULS = Ulysses). *The vertical axis* is the distance along the dipole axis and *the horizontal axis* is the distance normal to the dipole axis, hence the oscillations in the trajectory plots, due to the 10-hour rotation period of the planet. *The darker shaded area* represents the Jovian current sheet in the O6 model of the magnetic field in Jupiter's vicinity (Connerney et al. 1981a, 1981b; Connerney 1992), the lighter shaded area is the current sheet determined from the Ulysses measurements. The figure has been adapted from Dougherty et al. (1996)

sensitivity correction had to be carried out on the data from the instrument's other, $X-Z$ sensor, considerably reducing the values of the higher order terms (Acuña and Ness 1976) and better matching the data obtained by the other instruments on the spacecraft.

The results of the Pioneer 10 and 11 flybys remain important for the internal magnetic field of Jupiter, because to date no other spacecraft approached Jupiter closer. The following four flybys were more distant from the planet: Voyagers 1 and 2 in March and July 1979 (at periapsis distances of 4.9 and $10.1\,R_\mathrm{J}$), Ulysses in February 1992 (at a periapsis distance of $6.3\,R_\mathrm{J}$) and Cassini-Huygens in December 2000 at a distance of $138\,R_\mathrm{J}$. The Galileo mission targeted primarily the moons of Jupiter and will be referred to in more detail below.

The two Voyager spacecraft were launched on 20 August 1977 (Voyager 1) and on 5 September 1977 (Voyager 2). Both were targeted to flyby first Jupiter and then Saturn. However, after the Saturn flybys, Voyager 1 was sent on to encounter Uranus and Neptune. The trajectories of both spacecraft were to take them subsequently to the outermost regions of the heliosphere. The spacecraft crossed the termination shock of the heliosphere in late 2004 and in 2007, respectively.

The Jovian flybys took place on 5 March 1979 at a closest approach distance of $4.89\,R_\mathrm{J}$ (Voyager 1) and 9 July 1979 at $10.1\,R_\mathrm{J}$ (Voyager 2). The close-in flyby trajectories of the first five spacecraft that flew past Jupiter are illustrated in Fig. 43, in a Jupiter centred coordinate system that has its vertical axis aligned with Jupiter's dominant dipole axis. The measurements of the magnetic field in the planetary environment were reported by Ness et al. (1979a, 1979b). The planetary field of Jupiter, based on the Voyager and Pioneer results was presented by Connerney et al. (1982a), the Jovian current sheet and the inner magnetosphere were described by Connerney et al. (1981a).

The magnetic field investigation on the two Voyager spacecraft was described by Behannon et al. (1977). It consists of two sets of triaxial (vector) fluxgate sensors that are boom-mounted and the corresponding electronics in the spacecraft instrument bay. The deployable Voyager boom is 13 m in length from the spacecraft body to the boom tip. The two Low-Field Magnetometer (LFM) triaxial sensors are mounted on the boom tip and at a distance of 7.4 m from the spacecraft, respectively. The LFM measures the magnetic field vector in eight ranges, from ±8.8 nT to ±50,000 nT on each orthogonal axis; the corresponding digitisation errors are ±2.2 pT to ±12.2 nT. The sensor noise was ∼6 pT RMS; it was shown as a function of frequency in Fig. 6 in Sect. 2.2. The vector sampling rate was 16.67 Hz and the bandwidth of the instrument was 8.3 Hz to satisfy the Nyquist criterion. The two High-Field Magnetometer (HFM) triaxial sensors are mounted about 1 m apart, close to the spacecraft along the canister that contained the expandable boom. The HFM used specially developed small cores in the sensors, to minimise the power consumption that scales with the intensity of the field being measured. Its two measurement ranges were conservatively designed for the potentially large fields encountered near Jupiter and Saturn, covering ±50 μT and ±2 mT in each orthogonal axis, at a sampling rate of 1.67 vectors/s. During the Jupiter flyby, the Voyager 1 LFM operated in seven of its eight possible ranges, up to ±6, 400 nT per axis, so that there was no need to use the HFM data which had coarser resolution.

There were two specific aspects related to the Voyager magnetometer investigation that can be mentioned in addition. One is the use of the dual magnetometer technique applied to the two LFM sensor data. For Voyager, the dual magnetometer technique originally proposed by Ness et al. (1971) and refined by Neubauer and Schatten (1974) was written by Behannon et al. (1977) as

$$\mathbf{B}_{\mathrm{sc}}^{\mathrm{est}}(r_2) = \alpha \frac{[\mathbf{B}_{\mathrm{obs}}(r_1) - \mathbf{B}_{\mathrm{obs}}(r_2)]}{1-\alpha}$$

where $\mathbf{B}_{\mathrm{sc}}^{\mathrm{est}}(r_2)$ is the estimated value of the value of the magnetic field due to the spacecraft at the location (r_2) of the outboard sensor, $\mathbf{B}_{\mathrm{obs}}(r_1)$ and $\mathbf{B}_{\mathrm{obs}}(r_2)$ are the measured magnetic field values at the location of the inboard and outboard sensors, respectively, and $\alpha = (r_1/r_2)^3$ is the correction factor. Subtracting the estimated value of the spacecraft-caused background field $\mathbf{B}_{\mathrm{sc}}^{\mathrm{est}}(r_2)$∼0.2 nT from the measured value, $\mathbf{B}_{\mathrm{obs}}(r_2)$, at the outboard sensor is taken to provide the true value of the ambient field.

The second aspect is related to the knowledge of the orientation of the magnetometer axes with respect to the spacecraft reference frame on the 13 m expandable boom. The boom construction is a form of coiled spring which, when expanded, is quite stable against bending (±0.5° around axes perpendicular to the boom axis), but prelaunch tests have shown that the twist angle (rotation around the boom axis) is only reproducible to about 7°. To determine the orientation of the sensor axes after deployment of the boom in space, a calibration coil was installed around the high gain antenna dish of Voyager which, when energised with a 0.5 A current, generated a known magnetic field of amplitudes 6.1 nT and 33.4 nT respectively at the outboard and inboard LFM sensors. While this is not sufficient to provide an unambiguous calibration of the orientation of the sensor axes, appropriate assumptions and approximations made the calibration process of sufficient accuracy for the measurement of the planetary fields encountered by the two Voyager spacecraft (Behannon et al. 1977). A dual coil system was used for the same purpose of determining the magnetometer sensor alignment on the Cassini spacecraft (Dougherty et al. 2004) which has a boom of similar construction to that of the Voyager boom and is described below.

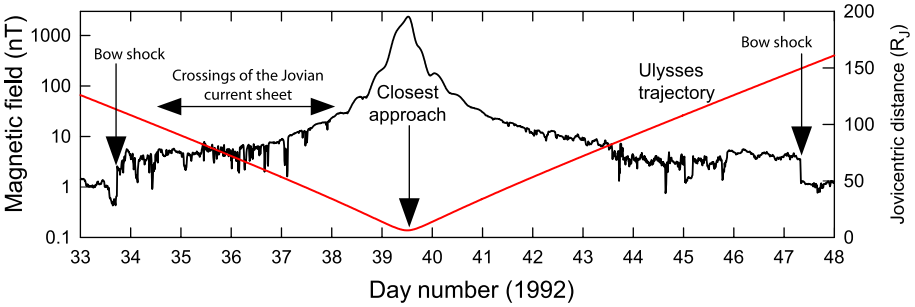

Fig. 44 The Jovian magnetic field during the Ulysses flyby in February 1992. Note the repeated crossings of the Jovian current sheet during the inbound part of the trajectory and the disturbed, dynamic nature of the magnetospheric magnetic field away from the closest approach to the planet. The jovicentric distance is shown in *red*

The Ulysses spacecraft flew by Jupiter in February 1992 for a gravity assist manoeuvre to deflect the trajectory of the spacecraft out of the ecliptic plane. The magnetic field observations during the flyby have been described by Balogh et al. (1992a), see in Fig. 44 the magnitude of the magnetic field through the 15 days interval while the spacecraft was inside the magnetosphere of Jupiter. Closest approach was at $6.3\,R_J$ on 8 February 1992. Given the closest part of the flyby trajectory (Fig. 43) that covered higher Jovian latitudes than either Voyager or Pioneer 10, but crossed the current sheet near the equator, Ulysses could assess the extent of the current sheet near its inner edge. It was found that for the Ulysses epoch, the current sheet was somewhat thicker (about $4\,R_J$ half width) than during the Voyager epoch (Connerney 1981) but with a reduced current density. Variations in the current sheet parameters are not surprising even near Jupiter, in response to the highly variable conditions that have been observed in the Jovian magnetosphere (Smith et al. 1975b; Connerney 1981; Dougherty et al. 1996).

In the Ulysses case, the sunward bow shock was encountered at $113\,R_J$ followed at $110\,R_J$ by an encounter with the magnetopause. The much larger distances seen by Ulysses than by any of the previous flybys by Pioneer and Voyager spacecraft indicate a much expanded magnetosphere during the Ulysses epoch, probably due to a sudden drop in solar wind pressure also noted by Ulysses (Balogh et al. 1992b). The bow shock and magnetopause encounters were also very close, given the size of the magnetosphere; this indicated a still expanding magnetosphere. It is generally recognised, that the outer part of the Jovian magnetosphere is subject to very large-scale dynamic effects dependent mostly on variations in the dynamic pressure of the solar wind.

The prominent feature of the middle and inner magnetosphere is the current sheet that was first discovered by Pioneer 10 (Smith et al. 1974a, 1974b) and observed by all subsequent spacecraft that reached the inner part of the Jovian magnetosphere. Observations from the last spacecraft to sample it (Russell et al. 1999a, 1999b) reported on its structure and summarized its variable features in the context of previous observations. The current sheet, extending from $5\,R_J$ to about $50\,R_J$ from the planet but with its outer edge ill-defined and variable, dominates the structure of the magnetosphere inside its outer edge. In addition, the current strength is strong enough to make a significant contribution to the measured magnetic field close to the planet (see Fig. 43) so that it makes the task of separating the internal planetary field considerably harder. Jupiter is, in this way, quite different from the other planets and it is difficult to apply concepts of external current systems derived from

similarity with earth-like magnetospheres (see review by Baumjohann et al. 2010a, 2010b, this issue).

The Ulysses magnetic field instrument was described by Balogh et al. (1992a). The instrument was optimized for the primary mission of Ulysses, exploring the heliospheric medium over the poles of the Sun. It consisted in two tri-axial sensors mounted on a 5 m long boom attached in the spin plane of the spacecraft. The outboard sensor is a Vector Helium Magnetometer (VHM) following the Pioneer 10 and 11 and ISEE-3 heritage, the inboard sensor is a ring-core vector Fluxgate Magnetometer (FGM). Because of the expected very weak magnetic fields in the heliosphere at 5 AU, an extremely careful magnetic cleanliness programme was carried out for the Ulysses spacecraft. It involved the magnetic compensation and test of the Radioisotope Thermoelectric Generator, as well as a full spacecraft level test programme in the MFSA facility (see Sect. 2.1) that resulted in a spacecraft background field of ∼0.03 nT at the location of the VHM and ∼0.1 nT at the location of the FGM. The VHM and FGM both had operating ranges of ±8 nT and ±64 nT per axis intended for the heliospheric medium and also for the outer regions of the Jovian magnetosphere; in addition, the FGM also had operating ranges for the Jovian flyby of ±2048 nT (resolution 1 nT) and ±44,000 nT (resolution ∼11 nT). The time resolution of the measurements was 1 vector/s for each of the magnetometers. As the spacecraft was spinning, the spin plane axes of the two magnetometers were easily calibrated for zero offset; for the spin axis offset, the method developed by Hedgecock (1975) was used. (The sensor offsets have been discussed in Sect. 2.4 above, see also Fig. 14.) By matching the two Jupiter ranges of the FGM during the flyby, the overall accuracy of the measurements (once the highest range data were averaged over 1 minute) was about 1 nT even for the data taken at closest approach (∼2,500 nT).

Although the published models of Jupiter's planetary magnetic field differ in some detail, the value of the dipole is well established within ∼5% from 1.46×10^{20} T m^3 corresponding to the original value reported by Smith et al. (1974a, 1974b) as $4.0GR_J^3$ to about 1.55×10^{20} T m^3 ($4.23 \times GR_J^3$, quoted by Connerney 1993 for Pioneer 11). The Ulysses value was 1.48×10^{20} T m^3 (Dougherty et al. 1996). The range of values for the dipole moment deduced from radio observations and from the direct spacecraft observations were compared by Smith and Gulkis (1979); the two sets generally agree within the variability of the values obtained either way. The angle between the dipole axis and the rotation axis is ∼10° and there are significant higher order multipoles in the spherical expansion of the internal field (see, e.g. Connerney 1993; Russell and Dougherty 2010). In fact, the ratios of the dipole, quadrupole and octupole terms for Jupiter are, about 1:0.25:0.2 compared to Earth for which these ratios are 1:0.14:0.1, indicating that the region of field generation in the interior of Jupiter extends out to about $0.8R_J$ (see, e.g. Stevenson 1983).

The Galileo spacecraft, the only orbiter so far around Jupiter, followed a complex mission plan with orbits targeted for a comprehensive exploration of the Jovian magnetosphere and the Galilean satellites. It was launched in 1989 and was inserted into Jupiter orbit in 1995 then repeatedly flew to $\sim 10R_J$ perijove during its orbiting mission (see Fig. 45 and discussion below). The orbits were modified by targeted flybys of the satellites, to set up successive phases of the exploration. The orbits during the first two years of operations in Jupiter orbit are shown in Fig. 45. The jovicentric distance of perijove passes is also shown in Fig. 45. However, the perijove distances of the orbits remained too high (Fig. 45) for higher order terms of the planetary magnetic field to be determined. Analysis of the magnetic field observations close to Jupiter have shown that there may have been some secular change in the dipole term (Russell et al. 2001, 2002), consistent with the type of change observed for the Earth's magnetic field.

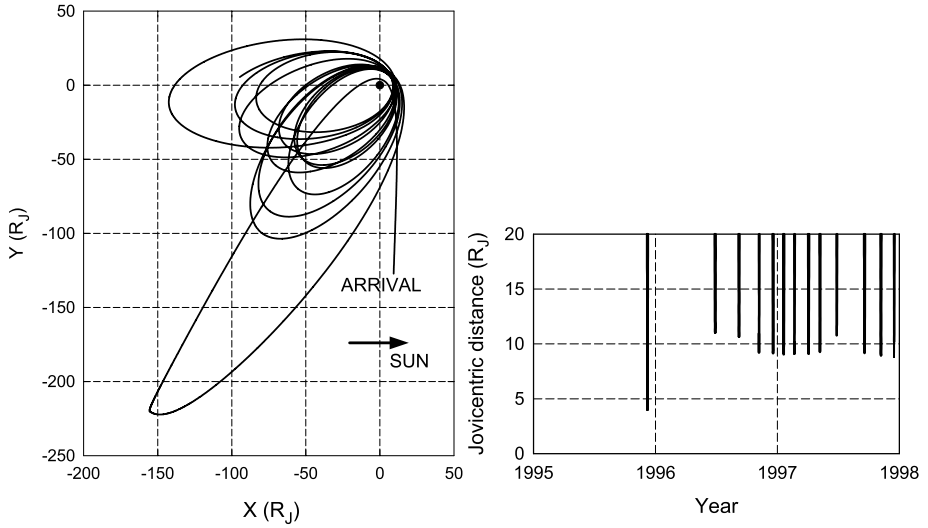

Fig. 45 *Left panel*: The operational orbits of the Galileo spacecraft in 1995–1997, following the arrival at Jupiter. The orbits were designed and optimised for close encounters with the Galilean moons. *Right panel*: Perijove passages of Galileo. The closest approach to Jupiter occurred on arrival to the planet

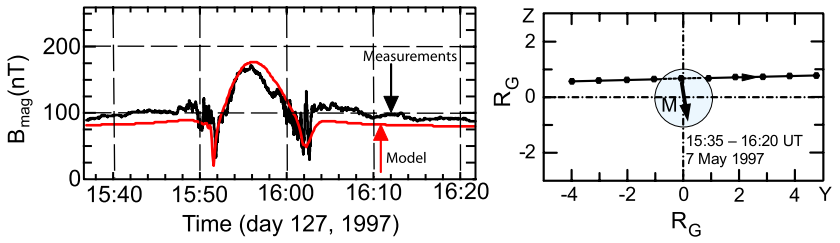

Fig. 46 (*Left panel*) The magnetic field magnitude measured by the Galileo spacecraft on one of its close flybys (G8) of the Galilean moon Ganymede (after Jia et al. 2010). (*Right panel*) The flyby geometry close to Ganymede. The trajectory is shown projected in the Jovian meridian plane passing through the centre of Ganymede; units along the axes are Ganymede radii. Markers along the trajectory are at intervals of 5 minutes. The trajectory passes in front of the moon, so that it samples the upstream region of Ganymede's magnetosphere. The modelled magnetic dipole of Ganymede is illustrated (after Kivelson et al. 1997)

The magnetic properties of the four Galilean moons were extensively investigated during the Galileo mission from December 1995 to September 2003. For a review of the magnetic fields of the satellites of Jupiter and Saturn, see Jia et al. (2010). The Galileo magnetometer discovered the internal, dynamo-generated magnetic field of Ganymede (Kivelson et al. 1996, 1997). Data from the eight close flybys of Ganymede were presented and analysed in terms of an internal dynamo component and a component due to induction by Kivelson et al. (2002). Magnetic field observations during one of the close passes by Ganymede are shown in Fig. 46, together with a model fit that estimates the dipole moment of Ganymede to be 1.4×10^{13} T m^3.

After six close flybys of the volcanic moon Io, the Galileo magnetic field observations did not show any evidence of an internal magnetic field. The magnetic signatures, however, showed the high level of complexity and variability of the interaction of the Jovian magnetic

field with Io's ionosphere that originates from the volcanic emissions (Khurana et al. 2002). Galileo also discovered the induced magnetic field in the interiors of Europa and Callisto (Khurana et al. 1998), both assumed to originate in subsurface oceans.

The induced magnetic field signatures observed by Galileo during the close flybys of Callisto and Europa (Khurana et al. 1998) and their interpretation has been extensively discussed (Schilling et al. 2004, see also for up-to-date assessments Jia et al. 2010; Saur et al. 2009). In particular, Europa has received close attention as there are indications that under its icy surface there may be a liquid ocean that provides the conductivity for its inductive signatures (Neubauer 1998). Europa is differentiated, with a metallic core, a silicate mantle and water-ice with the likelihood of liquid water covered by the ice sheets seen in images by the Galileo spacecraft. The magnetic field data acquired by Galileo during close flybys of Europa show that the induction signatures are clear when the moon is outside the Jovian current sheet, but that the magnetic signatures are more complex within the sheet due to the interaction of the induced field inside the moon with the current sheet.

The Galileo magnetic field investigation has been described by Kivelson et al. (1992). Two triaxial vector fluxgate magnetometer sensors are mounted on an extendable 11 m boom, one at the boom tip, the other at 6.87 m from the spacecraft spin axis. The Galileo spacecraft consisted of two sections, one section (with the in situ instruments including the magnetometer sensors) spinning at 3 rpm, the other despun for fixed direction pointing of the remote sensing instruments such as the camera system. One of the axes of the magnetometer sensors was aligned with the spacecraft spin axis, the other two were orthogonal in the spin plane. There were several sampling schemes foreseen, including a despun data stream with a resolution of $\sim$30 s/vector and a small data store capable of storing 200 averaged vectors for later transmission. Care was taken in the electronics and data sampling modes to include data filtering matching the Nyquist criterion.

As an in-flight calibration feature of the sensors, a thermally activated, bimetallic strip operated flipper mechanism was built into the sensors which allowed rotating the spin-axis oriented ring-core sensor into the spin plane, thus replacing the spin-axis sensor with one of the spin-plane sensors. The objective of such a flipper mechanism (first used on the lunar-orbiting Explorer 35 spacecraft, launched in 1967) is to determine the zero level of all three single-axis sensors. Offsets of the two sensors in the spin plane can be determined with great accuracy, as the signal from these two sensors are two sine waves in quadrature, synchronous with the spin (when the magnetic field is nearly steady over a spin period); the offset of the sine waves from a zero average is the value of the zero offset of the sensor. This, however, is not the case for the spin axis sensor for which the zero level determination is more complex (see, e.g. Hedgecock 1975). Additional in-flight calibration was foreseen using a MAG Cal Coil, a 0.5 m $\times$ 0.45 m square coil near the root of the boom which was to generate a calibration field of amplitude $\sim$4.5 nT at the outboard sensor with a sequence of on-off cycles at several frequencies. Synchronous detection of the calibration signal allowed the very precise determination of the orientation of the sensors (thus safeguarding against possible temperature-induced deformations in the boom) and their scale factors. The magnetometer analogue electronics was calibrated using internal calibration signals.

The measurement ranges on the Galileo magnetometer were $\pm$32 nT and $\pm$512 nT on each axis on the boom-tip magnetometer and $\pm$512 nT and $\pm$16, 384 nT on the inboard magnetometer. Some of the operations modes planned pre-launch (including planned high temporal resolution coverage) could not be carried out because of the non-deployment of the Galileo high-gain antenna after launch. However, a closely planned and highly targeted operations schedule for the magnetometer yielded extensive data during the mission, from both the magnetosphere and from the close flybys of the Galilean moons.

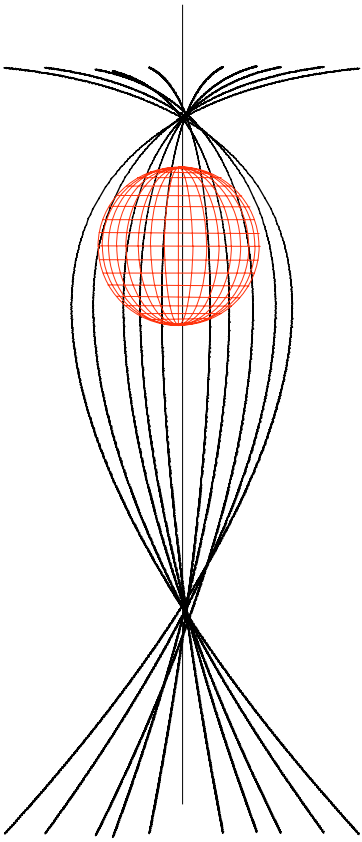

Fig. 47 Typical orbits of the Juno spacecraft close to perijove. A total of 30, 11-day period high inclination orbits will be spaced at 12° longitude intervals during the planned operational mission phase

The next mission to Jupiter will be NASA's Juno spacecraft (Bolton et al. 2006; Dodge et al. 2007; Matousek 2007). The spacecraft will be launched in 2011 and will, after a gravity assist flyby of Earth late in 2013, arrive at Jupiter in late 2016. The nominal orbit around Jupiter is very highly eccentric, with a polar inclination and has a period of 11 days. The apoapsis is at $\sim 39 R_J$, while periapsis distance is nominally $1.06 R_J$, and the orbit will vary between heights of 4200 and 5200 km above the planet at closest approach at about 30° north of the Jovian equator. The primary science operations will be concentrated in ± 3 hours around perijove. In all 32 such orbits are foreseen, with 30 of these orbits devoted to science data acquisition. The first 15 science orbits are phased with a separation of 24°, then, following an adjustment of 12°, the next 15 orbits, again at 24° phase separation, will complete the complete coverage of the planet at a longitudinal phasing of 12°. Typical orbits near perijove are sketched in Fig. 47.

The spacecraft is a spinner and has three solar panels. At the outboard edge of one of the solar panels, there is a special mounting platform for the magnetic field investigation. This investigation consists of two tri-axial fluxgate magnetometers, each co-mounted on an optical bench with two star cameras (Advanced Stellar Compasses) to determine with high accuracy the orientation of the magnetic field vector measurements (Connerney and Acuña 2008). The mounting platform and the locations of the two magnetometers is illustrated in Fig. 48. (The figure also shows the location of a planned Scalar helium Magnetometer that was originally foreseen for the mission but was descoped due to limitation of resources.)

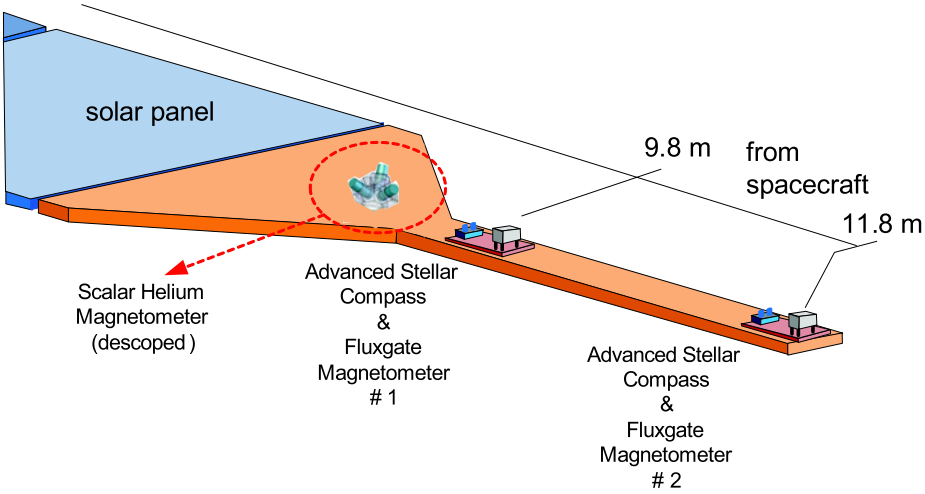

Fig. 48 The accommodation of the two triaxial Fluxgate Magnetometers on an extension to one of the solar panels on NASA's forthcoming Juno mission to Jupiter. The sensors are co-mounted on optical benches with the Advanced Stellar Compasses that provide very high accuracy pointing information. This is to minimise the attitude error in the magnetic field measurements. The originally planned Scalar Helium Magnetometer was descoped late in the development programme due to resources limitations

Given the very close passage of the spacecraft over the northern polar regions, the prime scientific objectives of the magnetic field investigation include detailed measurements of the jovian auroral system, field aligned currents and magnetosphere-ionosphere coupling.

The magnetometer is expected to measure field strengths of up to 12 Gauss (1.2 mT) near perijove, within a very rapidly changing magnetic field environment. The highest sampling frequency of the magnetometer is 64 Hz, used near the planet. The magnetometers have to be able to cover the variation field strength expected around the orbit, down to the level of a few nT, or at least six orders of magnitude.

4.2 Saturn

Unlike in the case of Jupiter, no kilometric radiation had been detected from Earth to conclude about the existence and size of its magnetic field (for an extensive discussion see, e.g. Kaiser et al. 1984). The discovery of modulation in the radio emissions observed by Voyager 1 before encountering Saturn (Kaiser et al. 1980) revealed features in the planet's magnetic field that needed closer investigation by the magnetometers on the flyby missions. Scaling laws based on planetary models comparing Jupiter and Saturn had predicted a larger internal dipole moment than was found by in situ measurements. The differences with the predictions and their consequences for the structure and composition of Saturn's interior were first discussed by Stevenson (1980) and, more recently, by Christensen and Wicht (2008). The first measurements of Saturn's magnetic field were taken on 1 September 1979 when Pioneer 11 flew by the planet, in a close to equatorial orbit, making a closest approach at a Kronocentric distance of $1.35 R_S$, or about 21,000 km above the planet's surface.

The measurements made by the Pioneer 11 VHM instrument (Smith et al. 1980a, 1980b), illustrated in Fig. 49, were used to construct a model of Saturn's magnetic field. Thanks to the very close flyby distance, the data provided sufficient resolution to the model so

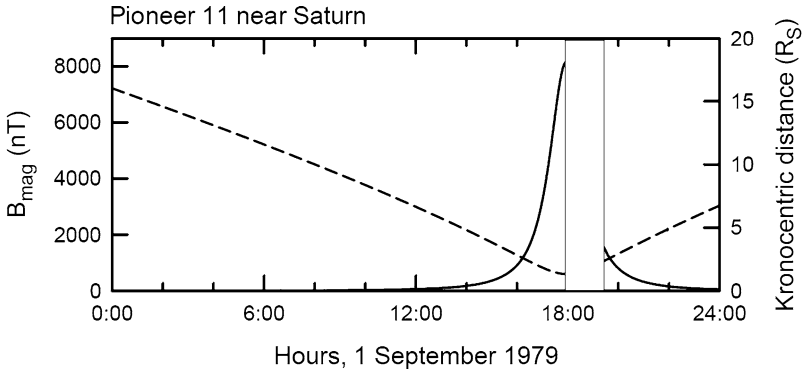

Fig. 49 The magnitude of the magnetic field measured by the VHM instrument on the Pioneer 11 spacecraft on the day of closest approach to Saturn (1 September 1979). The Kronospheric distance is shown in *dashed lines*

that differences between the measurements and the model field were found to be consistently less than 0.5%. In particular, the Pioneer 11 measurements showed the remarkable and unexpected axisymmetry of the internal magnetic field. A similar conclusion was drawn from the High Field Magnetometer measurements (Acuña and Ness 1980a; Acuña et al. 1980b). However, when comparing the models derived from Pioneer 11 to the models based on the subsequent Voyager flybys (see below), it was found that due to the very small angle between the spacecraft-Sun direction and the spacecraft spin axis during the encounter, the modulation signal provided by the spacecraft sun-sensor from which the spin phase angle of the spacecraft was derived was probably in error by about 1.4° (Connerney et al. 1984). As the spin phase angle is used for the demodulation of the magnetometer signal, this error was found to be a source of a small discrepancy between the models derived from Pioneer 11 and Voyager 1 and 2 (Acuña et al. 1983; Connerney et al. 1984; Davis and Smith 1986, 1990).

The axisymmetry of the magnetic field found by Pioneer 11 and subsequently by Voyagers 1 and 2 (Connerney et al. 1982b) was difficult to reconcile not only with the dynamo theorem that excluded the existence of such dynamos Cowling 1933, but also with the modulation detected in the Saturn kilometric radiation (SKR, e.g. Kaiser et al. 1984) that showed a strong periodicity at what was interpreted as the internal rotation rate of the planet. Following the analysis of Ulysses observations of the SKR, Galopeau and Lecacheux (2000) found that there was a variability in the modulation of the radio signal, contrary to what had been found by Voyager. The results of the Cassini orbiter concerning the rotation rate of Saturn, using the magnetic field data (Giampieri et al. 2006) or the radio data or both (Gurnett et al. 2007) have not attributed a firm period but have shown instead a variability that remains fully to be explained (Kurth et al. 2008; Burton et al. 2009). However, the modulation of the Saturn kilometric radiation is sufficiently strong and has been used to establish a kronographic longitude system that is now in general use (Kurth et al. 2008).

Voyagers 1 and 2 reached their closest approach to Saturn on 12 November 1980 at $3.07 R_S$ and on 26 August 1981, at a distance of $2.69 R_S$, respectively. Contrary to Pioneer 11 which had a closer approach than the Voyager spacecraft but remained close to Saturn's equatorial plane, the Voyager flyby trajectories covered a wider range of kronospheric latitudes and their longitude coverage was largely complementary around the planet (Fig. 50).

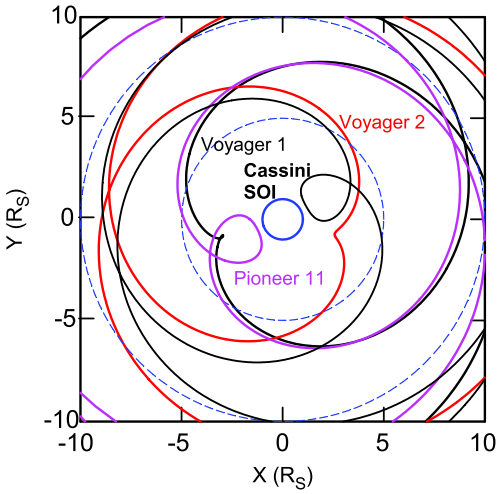

Fig. 50 Flyby orbits of Pioneer 11, Voyager 1 and 2 spacecraft close to Saturn in the kronographic equatorial plane and the Saturn Orbit Injection trajectory of Cassini. (Saturn is the blue circle at the centre of the coordinate system, the dashed blue circles show kronocentric distances of 5 and $10R_S$, respectively.) The closest approaches were, respectively, 1.35 (P11), 3.07 (V1), 2.69 (V2) and $1.33R_S$ (Cassini). While Pioneer 11 covered a limited range of latitudes close to the equatorial plane, the two Voyager spacecraft covered complementary kronographic longitude ranges and latitude ranges of more than $\pm 30°$. Cassini's close approaches during its orbiting phase have also covered a broad range of latitudes (see Fig. 51)

The magnetic field observations, made with the same instrumentation that had already visited Jupiter, were reported by Ness et al. (1981, 1982).

The Voyager measurements confirmed the near-axial orientation of the dominant dipole moment of Saturn's internal magnetic field as well as the magnitude of the dipole moment as 4.3×10^{18} T m^3 (or, as quoted by Ness et al. 1982, ~0.21 Gauss R_S^3). For detailed confirmation and analysis of the Voyager 2 data, an initial error in the spacecraft roll orientation needed correcting (Ness et al. 1982; Connerney et al. 1982a). Such a correction, even if small, affects some of the detailed interpretation of the data; this is particularly relevant near Saturn, because of the complex deciphering needed to assess the respective contributions of the internal field and the spatially and temporally varying external current systems (Connerney et al. 1983, and for the latest assessment of the problem, see Arridge et al. 2008, Blanc et al., 2009). The axisymmetry of Saturn's magnetic field remains to be fully understood. Models of its interior structure that explain the axisymmetry have been proposed (Stevenson 1982); in such models, the dynamo generation region is masked by an overlaying stratified layer still deep in the planet's interior.

Following the analyses carried out first on the data from Pioneer 11 and then of the two Voyagers, a comprehensive review of the combined data set was carried out by Davis and Smith (1990). This review confirmed the previous findings concerning the axisymmetry of the magnetic field. It also considered the higher order, axial quadrupole and octupole terms and examined the sensitivity of these higher order terms, and in particular any non-axisymmetric terms and found that the flyby data were not sufficient to constrain them uniquely. As in all cases, orbiter spacecraft are, in principle required for a comprehensive determination of planetary magnetic fields; the arrival of the Cassini orbiter around Saturn on 1 July 2004 (Dougherty et al. 2005) was the start of a new phase in the exploration of the magnetic fields and the environment of Saturn. The still-unresolved question of Saturn's

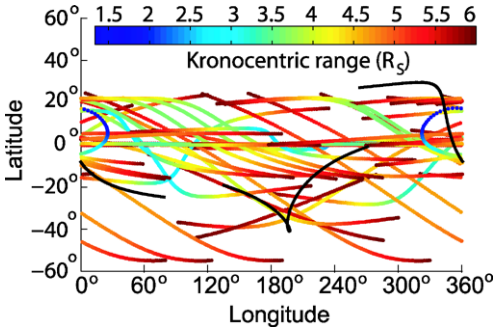

Fig. 51 Orbital coverage of the Cassini spacecraft in kronographic coordinates from Saturn Orbit Insertion on 1 July 2004 up to 12 June 2007. The kronocentric radial distance is colour coded on the tracks and covers the range up to $6R_S$. Data acquired during these orbits have been used to determine Saturn's internal magnetic field by Burton et al. (2009). *The heavy black lines* show the coverage of the Voyager 1 and 2 spacecraft also up to $6R_S$ (after Burton et al. 2009)

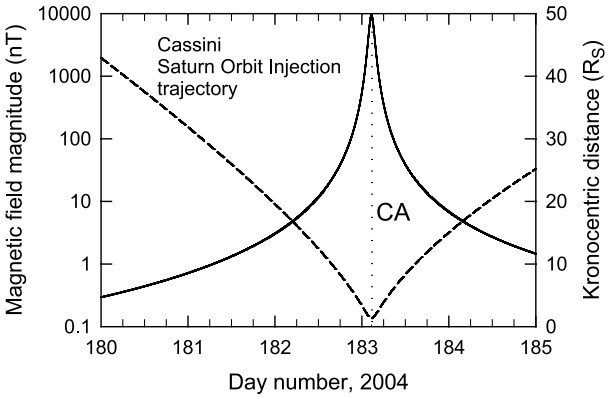

Fig. 52 The magnetic field magnitude measured by the Cassini magnetometer prior and following the closest approach passage to Saturn during orbit injection. The Kronocentric distance of the spacecraft is shown as a *dashed line*. In contrast to the close jovian passages when the current sheet noticeably affected the magnetic field on similar timescales (Fig. 43), note the absence of a significant contribution from Saturn's external environment to the field magnitude

rotation period and the processes that it generates to yield complex periodic signals in radio waves and the magnetic field has already been mentioned. The internal field has recently been the subject of a comprehensive reappraisal by Burton et al. (2009), using those parts of the Cassini orbits which were within $6R_S$ of the planet over a close to three year interval from Saturn Orbit Injection; the projections of these orbit segments in cronographic latitude and longitude are shown in Fig. 51, together with the two orbit segments from the Voyager flybys that were also within $6R_S$.

The Cassini magnetometer investigation has been described in detail by Kellock et al. (1996), Smith et al. (2001) and Dougherty et al. (2004). It consists of two sensors mounted on an 11 m boom that was extended during the cruise phase of the mission, prior to the spacecraft's swingby of the Earth on 18 August 1999. The results of the Earth's flyby, primarily intended to boost the spacecraft's speed on its way to Jupiter and Saturn, was also useful in providing an opportunity to calibrate the magnetometers; the results of the flyby have been described by Smith et al. (2001) and Southwood et al. (2001). The sensors are a Vector/Scalar Helium Magnetometer (V/SHM) mounted at the tip of the 11-m long magnetometer boom and a Fluxgate Magnetometer at 5.5 m inboard from the boom tip (see above, Fig. 11 in Sect. 2.3).

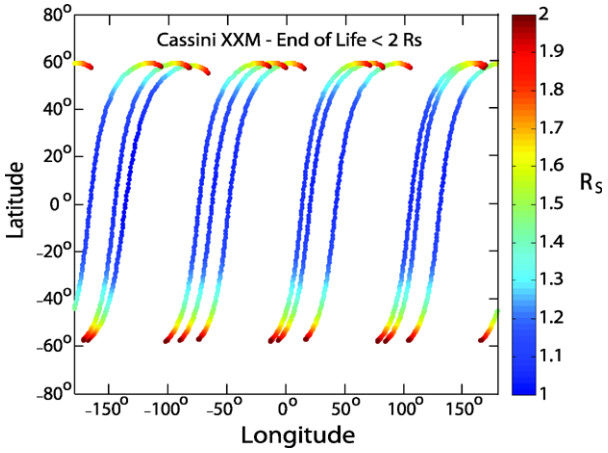

Fig. 53 Planned end-of-life orbits for the Cassini mission at the conclusion of its Extended-Extended Mission (XXM) in 2017. The wide latitude coverage enabled by the high latitude inclination orbit with a very low periapsis near the equatorial plane will lead to a significant addition to the magnetic field measurements from which the internal field of Saturn can be better characterised figure courtesy of M. Burton)

The Fluxgate magnetometer (FGM) is of classical construction using three orthogonally arranged ringcore sensors mounted on a ceramic holder chosen for its low thermal expansion coefficient and machined for dimensional stability. The noise performance of the FGM sensors is better than 5 pT/Hz$^{1/2}$ at 1 Hz. The FGM measures the magnetic field vector at a rate of 32 vectors/s. The operating ranges in normal use are $\pm$40 nT, $\pm$400 nT and $\pm$10,000 nT per axis with corresponding resolutions of $\sim$5 pT, 49 pT and 1.2 nT. The instrument also has a range of $\pm$44,000 nT that was used for ground testing. It is noted that the maximum value of the magnetic field amplitude at closest approach (at $1.33 R^{\mathrm{S}}$ planetocentric distance) during Saturn orbit injection was 9,420 nT (see Fig. 52), thus maximising the relative resolution through the operating range.

The V/SHM is an optically pumped helium magnetometer, built using the inheritance of previous missions, in particular Ulysses, described in Sect. 2.3. It normally operated in vector mode, measuring the ambient field at the rate of 2 vectors/s through the cruise phases of the mission.

A particularly interesting possibility for extending the magnetic field measurements is being planned at the conclusion of the so-called Extended-Extended Mission (XXM) of Cassini. This phase of the mission will cover the years 2011 to 2017, with, at its conclusion, 28 orbits reaching inclinations $\sim$63°, with a height above the 1 bar pressure level ("the cloud tops") of only 2000 to 5000 km. These orbits are sketched in Fig. 53. This set of orbits would allow a significant increase in the accuracy of the magnetic field measurements that could be used to refine the internal field model that is offset to the northern hemisphere and also the rotation rate of the planet.

4.3 Uranus and Neptune

The two outermost planets in the solar system, the icy giants, have only been visited once, by Voyager 2 when the spacecraft trajectory took advantage of the special alignment of the planets that only occurs every 187 years. The Uranus flyby took place on 24 January 1986, at a closest approach of $4.19 R_{\mathrm{U}}$ where $R_{\mathrm{U}} = 25{,}559$ km. Voyager 2 flew by Neptune on 25 August 1989 at a closest approach distance of $1.18 R_{\mathrm{N}}$ where $R_{\mathrm{N}} = 24{,}760$ km.

The magnetic field measurements around the closet approach and their interpretations were described by Ness et al. (1986) for the Uranus flyby and by Ness et al. (1989) for the Neptune flyby. The results are recalled and summarised by Ness (2010). The Voyager

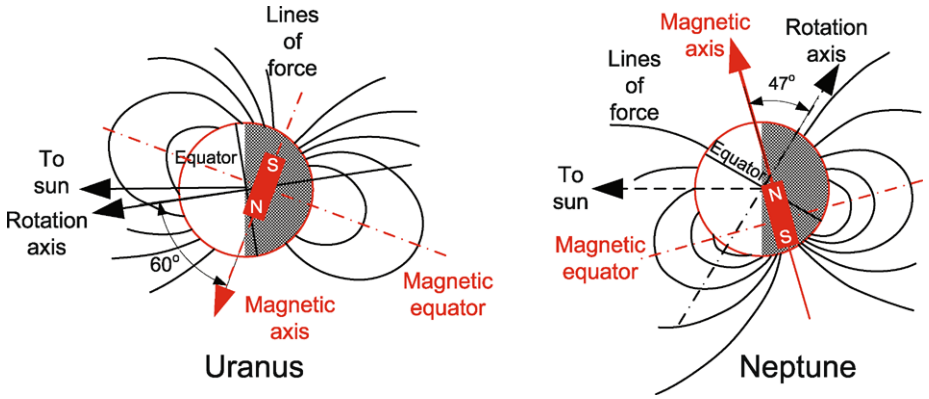

Fig. 54 Equivalent dipoles representing the internal magnetic fields of Uranus and Neptune (after Ness et al. 1986, 1989, see also Ness 2010)

magnetometers have been described above in Sect. 4.1. The following brief descriptions follow the two discovery papers (Ness et al. 1986, 1989).

In the case of both these planets, significant magnetic fields of internal origin were observed. The maximum field measured at Uranus was 413 nT, a few minutes away from closest approach. Uranus' rotation axis is fact close to the planet's orbital plane, so that the spacecraft's flyby trajectory, not far off Uranus' orbital plane, covered a wide range of latitudes. Both the magnetosphere of Uranus and its internal magnetic field have orientations which are far from that of the other planets (except Neptune). The analysis of the flyby data was best fitted (Connerney et al. 1987) with an offset, tilted dipole as illustrated in Fig. 54. A very special feature of Uranus' internal magnetic field, when represented by the equivalent offset, tilted dipole is the large angle (∼60°) between the rotation axis of the planet and the dipole axis.

During the much closer approach (when compared to that near Uranus) during the flyby of Neptune the maximum magnetic field observed by the Voyager magnetometer was 9,700 nT. Similarly to Uranus, the observations could be fitted with an offset, tilted dipole with an axis at ∼47° from the rotation axis, shown schematically in Fig. 54.

In addition to the very different orientation and location of the internal dipoles of Uranus and Neptune, when compared to the other two giant planets, Jupiter and Saturn, large quadrupolar terms were found as well (Connerney et al. 1991; Connerney 1993). Clearly, the very different internal structure and composition in the case of the icy giants leads to dynamo mechanisms and geometries which are unique to these two planets. Detailed modelling and numerical simulations have led to a better understanding of the dynamo processes (Stanley and Bloxham 2004, 2006; Stanley and Glatzmaier 2010) as well as the internal structure and material characteristics of these planets. Given the challenges to reach both the icy giants, it is unlikely that follow-up missions will be envisaged for a considerable time, so that the Voyager 2 observations will remain the benchmark against which continued understanding of these planets will be tested.

5 Conclusion

In the past five decades, about five dozen space missions have made useful magnetic field measurements in the vicinity of the eight planets of the solar system as well as close to some

of the smaller bodies. As reviewed by Stevenson (2010), there is a good basic understanding and detailed knowledge of the magnetic properties of all the planets, despite their considerable diversity. The degree of similarity is small among the usual grouping of the planets (terrestrial planets, gas giants, ice giants).

It is recognised that magnetic field measurements contribute information about the interiors of planets that is not accessible by other measurements. Furthermore, the magnetic state of planets is also an important factor in understanding the evolution of planets from the time of their formation. As this importance is recognised by planetary scientists, there is a requirement for future missions that will provide even more detailed magnetic field measurements to constrain planetary interiors and their evolution. While it is unlikely that the planets will be as well characterised as the Earth is now, but enough uncertain parameters remain concerning the operation of planetary dynamos to make more precise observational constraints necessary.

Planetary spacecraft that measure magnetic fields precisely need to have low-altitude and high-inclination orbits to ensure appropriate coverage. In several cases, this is difficult: at Mercury, the thermal constraints are very demanding and expensive, at Jupiter and Saturn there are challenges in terms of both orbital dynamics and tolerable radiation dose. Simply reaching the ice giants within the next generation will be unlikely, due to the combination of relatively small interest and the high cost. A possible future motivation for better understanding the planets in our solar system (which involves better understanding their magnetic properties) will be the need to make comparisons with extrasolar planetary systems as these will be discovered and characterised in increasing detail.

In terms of instrumentation, the magnetometers available today have the required performance to make the high resolution measurements that will be required. This applies equally to the fluxgate magnetometers and to the quantum (Helium 4) magnetometers. There will be an effort to further optimise resources required by these instruments, but it is likely that appropriate performance will be achieved by resources (mass, power) that are similar to contemporary instruments. Another resource, telemetry bandwidth, needs to be increased (higher vector measurement rates). There has been some erosion of telemetry rates: it is symptomatic that the vector rate allocated to the magnetometer on BepiColombo is less than that used on Mariner 10 almost 40 years ago. The need for higher telemetry rates arises partly from the requirement for denser spatial coverage and partly for the identification of the time variable component of the magnetic field at the location of the measurements due to external sources. Understanding the nature of the external sources that in all cases influence the in situ measurements is a necessary requirement for identifying the internal sources of planetary magnetic fields. These external terms are always significant and, because of their origin in dynamic plasma interactions, are always variable.

The greatest challenge to useful magnetic field measurements comes from the spacecraft-generated background at the location of the magnetometer sensor. Many ground-breaking early missions had a long boom for mounting the magnetometer away from the spacecraft. This was combined with a magnetic cleanliness programme that ensured that both the static and dynamic components of the disturbing background were minimised. Due to the pressure on costs, booms and the magnetic cleanliness programme are increasingly considered to be luxuries on planetary missions and often inadequate alternatives are pressed on experimenters who are then faced with an almost impossible challenge to clean the measurements from the spacecraft interference. There have been notable successes: the Giotto mission to comet Halley, the Mars Global Surveyor that identified the source of Mars' magnetism and Venus Express that is able to provide detailed characterisation of the Venus magnetic environment are examples where the experimenters were able to clean the raw data sufficiently

for major discoveries to be made. However, the need for future measurements is for accuracies that can only achieved by space missions on which the magnetometer can measure the ambient magnetic field without any significant background from the spacecraft.

Acknowledgements The author thanks his many colleagues who over the years have helped him understand magnetometers and their measurements in planetary environments. Particular thanks are due to Dr Ed Smith (JPL) who has been a great source of knowledge and wisdom on magnetic field measurements and missions that carried magnetometers. The author is also privileged to have known and collaborated with the late Dr Mario Acuña who has had the opportunity to visit with his magnetometers all the planets as well as comets and asteroids. Thanks are also due to the International Space Science Institute, its Founding Director, Professor Johannes Geiss and its current Executive Director Professor Roger Bonnet for creating a highly successful environment in which scientists can make significant progress in understanding a wide range of space science topics.

References

M.H. Acuña, IEEE Trans. Magn. **MAG-10**, 519–523 (1974)
M.H. Acuña, John Hopkins APL Tech. Dig. **1**, 210–213 (1980)
M.H. Acuña, Rev. Sci. Instrum. **73**, 3717–3735 (2002)
M.H. Acuña, C.J. Pellerin, IEEE Trans. Geosci. Electron. **GE-7**, 252–260 (1969)
M.H. Acuña, N.F. Ness, Space Sci. Instrum. **1**, 177–188 (1975a)
M.H. Acuña, N.F. Ness, Nature **253**, 327 (1975b)
M.H. Acuña, N.F. Ness, J. Geophys. Res. **81**, 2917–2922 (1976)
M.H. Acuña, N.F. Ness, Science **207**, 444 (1980a)
M.H. Acuña, C.S. Scearce, J. Seek, J. Scheifele, NASA Technical Memorandum 79656, NASA/GSFC, 1978
M.H. Acuña, N.F. Ness, J.E.P. Connerney, J. Geophys. Res. **85**, 5675–5678 (1980b)
M.H. Acuña, J.E.P. Connerney, N.F. Ness, J. Geophys. Res. **88**, 8771–8778 (1983)
M.H. Acuña, J.E.P. Connerney, P. Wasilewski, R.P. Lin, K.A. Anderson, C.W. Carlson, J. McFadden, D.W. Curtis, H. Réme, A. Cros, J.L. Médale, J.-A. Sauvaud, C. d'Uston, S. Bauer, P. Cloutier, M. Mayhew, N.F. Ness, J. Geophys. Res. **97**, 7799–7814 (1992)
M.H. Acuña, J.L. Scheifele, P. Stella, C. Kloss, B. Smith, G. Heinshohn, K. Sharmit, in *Photovoltaic Specialists Conference, Conference Record of the Twenty Fifth IEEE* (1996), pp. 325–328
M.H. Acuña, C.T. Russell, L.J. Zanetti, B.J. Anderson, J. Geophys. Res. **102**, 23751–23760 (1997)
M.H. Acuña, J.E.P. Connerney, P. Wasilewski, R.P. Lin, K.A. Anderson, C.W. Carlson, J. McFadden, D.W. Curtis, D. Mitchell, H. Reme, C. Mazelle, J.A. Sauvaud, C. d'Uston, A. Cros, J.L. Medale, S.J. Bauer, P. Cloutier, M. Mayhew, D. Winterhalter, N.F. Ness, Science **279**, 1676–1680 (1998)
M.H. Acuña, J.E.P. Connerney, N.F. Ness, R.P. Lin, D. Mitchell, C.W. Carlson, J. McFadden, K.A. Anderson, H. Rème, C. Mazelle, D. Vignes, P. Wasilewski, P. Cloutier, Science **284**, 790–793 (1999)
M.H. Acuña, J.E.P. Connerney, P. Wasilewski, R.P. Lin, D. Mitchell, K.A. Anderson, C.W. Carlson, J. McFadden, H. Réme, C. Mazelle, D. Vignes, S.J. Bauer, P. Cloutier, N.F. Ness, J. Geophys. Res. **106**, 23,403–23,417 (2001)
M.H. Acuña, B.J. Anderson, C.T. Russell, P. Wasilewski, G. Kletetshka, L. Zanetti, N. Omidi, Icarus **155**, 220–228 (2002)
I.I. Alexeev, E.S. Belenkaya, S.Yu. Bobrovnikov, J.A. Slavin, M. Sarantos, J. Geophys. Res. **113**, CiteID A12210 (2008). doi:10.1029/2008JA013368
B.J. Anderson, L.J. Zanetti, D.A. Lohr, J.R. Hayes, M.H. Acuña, C.T. Russell, T. Mulligan, IEEE Trans. Geosci. Remote Sens. **39**, 907–917 (2001)
B.J. Anderson, M.H. Acuña, D.A. Lohr, J. Scheifele, A. Raval, H. Korth, J.A. Slavin, Space Sci. Rev. **131**, 417–450 (2007)
B.J. Anderson, M.H. Acuña, Adv. Space Res. **33**, 1989–1995 (2004)
B.J. Anderson, M.H. Acuña, H. Korth, M.E. Purucker, C.L. Johnson, J.A. Slavin, S.C. Solomon, R.L. McNutt Jr., Science **321**, 82–85 (2008)
B.J. Anderson, M.H. Acuña, H. Korth, J.A. Slavin, H. Uno, C.L. Johnson, M.E. Purucker, S.C. Solomon, J.M. Raines, T.H. Zurbuchen, G. Gloeckler, R.L. McNutt Jr., Space Sci. Rev. (2009). doi:10.1007/s11214-009-9544-3, this issue
K.A. Anderson, L.M. Chase, R.P. Lin, J.E. McCoy, R.E. McGuire, J. Geophys. Res. **77**, 4611–4626 (1972)
K.A. Anderson, H.C. Howe, R.P. Lin, R.E. McGuire, L.M. Chase, J.E. McCoy, Lunar Planet. Sci. Conf. **5**, 18 (1974)

C.S. Arridge, C.T. Russell, K.K. Khurana, N. Achilleos, S.W.H. Cowley, M.K. Dougherty, D.J. Southwood, E.J. Bunce, J. Geophys. Res. **113**, 4214 (2008)
H.-U. Auster, K.-H. Fornacon, J. Rustenbach, Th. Roatsch, R. Schoredter, K. Schwingenschuh, V. Auster, Geophys. Res. Lett. **17**, 881–884 (1990)
H.-U. Auster, A. Lichopoj, J. Rustenbach, H. Bitterlich, K.-H. Fornacon, O. Hillenmaier, R. Krause, S. Schenk, V. Auster, Meas. Sci. Technol. **6**, 477–481 (1995)
H.-U. Auster, I. Apathy, G. Berghofer, A. Remizov, R. Roll, K.H. Fornacon, K.H. Glassmeier, G. Haerendel, I. Hejja, E. Kührt, W. Magnes, D. Moehlmann, U. Motschmann, I. Richter, H. Rosenbauer, C.T. Russell, J. Rustenbach, K. Sauer, K. Schwingenschuh, I. Szemerey, R. Waesch, Space Sci. Rev. **128**, 221–240 (2007)
H.-U. Auster, I. Richter, K.-H. Glassmeier, G. Berghofer, C.M. Carr, U. Motschmann, Magnetic field investigations during Rosetta's 2867 Steins flyby. Planet. Space Sci. (2010, in press)
A. Balogh, T.J. Beek, R.J. Forsyth, P.C. Hedgecock, R.J. Marquedant, E.J. Smith, D.J. Southwood, B.T. Tsurutani, Astron. Astrophys. Suppl. Ser. **92**, 221–236 (1992b)
A. Balogh, M.K. Dougherty, R.J. Forsyth, D.J. Southwood, E.J. Smith, B.T. Tsurutani, N. Murphy, M.E. Burton, Science **257**, 1515–1518 (1992a)
A. Balogh, C.M. Carr, M.H. Acuña, M.W. Dunlop, T.J. Beek, P. Brown, K.-H. Fornacon, E. Georgescu, K.-H. Glassmeier, J. Harris, G. Musmann, T. Oddy, K. Schwingenschuh, Ann. Geophys. **19**, 1207–1217 (2001)
M.A. Barucci, M. Fuchignoni, A. Rossi, Space Sci. Rev. **128**, 67–78 (2007)
W. Baumjohann, M. Blanc, A. Fedorov, K.-H. Glassmeier, Space Sci. Rev. (2010a). doi:10.1007/s11214-010-9629-z
W. Baumjohann, A. Matsuoka, W. Magnes, K.-H. Glassmeier, R. Nakamura, H. Biernat, M. Delva, K. Schwingenschuh, T. Zhang, H.U. Auster, K.-H. Fornacon, U. Motschmann, I. Richter, A. Balogh, C. Carr et al., Planet. Space Sci. **58**, 279–286 (2010b)
K.W. Behannon, M.H. Acuña, L.F. Burlaga, R.P. Lepping, N.F. Ness, F.M. Neugebauer, Space Sci. Rev. **21**, 235–257 (1977)
J.W. Belcher, J. Geophys. Res. **78**, 6480–6490 (1973)
J. Benkhoff, J. van Casteren, H. Hayakawa, M. Fujimoto, H. Laakso, M. Novara, P. Ferri, Planet. Space Sci. **58**, 2–20 (2010)
G.L. Berge, S. Gulkis, in *Jupiter*, ed. by T. Gehrels (University of Arizona Press, Tucson, 1976), pp. 621–692
S. Bolton (The Juno Science Team), in *1st European Planetary Science Conference*, Berlin (2006)
P. Brauer, J.M.G. Merayo, O.V. Nielsen, F. Primdahl, J.R. Petersen, Sens. Actuators A **59**, 70–74 (1997)
W. Braunbek, Z. Phys. **88**, 399–402 (1934)
H.S. Bridge, A.J. Lazarus, C.W. Snyder, E.J. Smith, L. Davis Jr., P.J. Coleman Jr., D.E. Jones Mariner V, Science **158**, 1669–1673 (1967)
B.F. Burke, K.L. Franklin, J. Geophys. Res. **60**, 213–217 (1955)
M.E. Burton, M.K. Dougherty, C.T. Russell, Planet. Space Sci. **57**, 1706–1713 (2009)
F.H. Busse, Phys. Earth Planet. Inter. **12**, 350–358 (1976)
J.C. Cain, R.E. Sweeney, J. Geophys. Res. **75**, 4360–4362 (1970)
J.C. Cain, Rev. Geophys. Space Phys. **9**, 259–272 (1971)
C.M. Carr, P. Brown, T.L. Zhang et al., Ann. Geophys. **23**, 2713–2732 (2005)
J.J. Chaillout, N. Kernevez, J.-M. Leger, Optical pumping, resonance magnetometer using a light beam with controlled polarization, US Patent, No. 5,272,436 (1993)
U.R. Christensen, J. Wicht, Icarus **196**, 16–34 (2008)
F.D. Colegrove, P.A. Franken, Phys. Rev. **119**, 680–690 (1960)
P.J. Coleman Jr., G. Schubert, C.T. Russell, L.R. Sharp, in *Apollo 15 Preliminary Science Report*, NASA SP-289, pp. (22)1–(22)9 (1972a)
P.J. Coleman Jr., B.R. Lichtenstein, G. Schubert, C.T. Russell, L.R. Sharp, in *Apollo 16 Preliminary Science Report*, NASA SP-315, pp. (23)1–(23)13 (1972b)
F.R. Colomb, C. Alonso, C. Hofmann, I. Nollmann, Adv. Space Res. **34**, 2194–2199 (2004)
J.E.P. Connerney, J. Geophys. Res. **86**, 7679–7693 (1981)
J.E.P. Connerney, in *Planetary Radio Emissions III*, ed. by H.O. Rucker, S.J. Bauer, M.L. Kaiser (Austrian Acad. of Sci. Press, Vienna, 1992), pp. 13–33
J.E.P. Connerney, J. Geophys. Res. **98**, 18,659–18,679 (1993)
J.E.P. Connerney, M.H. Acuña, The Juno magnetic field investigation (MAG): exploration of the polar magnetosphere, American Geophysical Union, Fall Meeting, abstract #SM41B-1679 (2008)
J.E.P. Connerney, M.H. Acuña, N.F. Ness, J. Geophys. Res. **86**, 8370–8384 (1981a)
J.E.P. Connerney, M.H. Acuña, N.F. Ness, Nature **292**, 724–726 (1981b)
J.E.P. Connerney, M.H. Acuña, N.F. Ness, J. Geophys. Res. **87**, 3623–3627 (1982a)
J.E.P. Connerney, N.F. Ness, M.H. Acuña, Nature **298**, 44 (1982b)

J.E.P. Connerney, M.H. Acuña, N.F. Ness, J. Geophys. Res. **88**, 8779–8789 (1983)
J.E.P. Connerney, M.H. Acuña, N.F. Ness, J. Geophys. Res. **89**, 7541–7544 (1984)
J.E.P. Connerney, M.H. Acuña, N.F. Ness, J. Geophys. Res. **92**, 15329–15336 (1987)
J.E.P. Connerney, M.H. Acuña, N.F. Ness, J. Geophys. Res. **96**, 19023–19042 (1991)
J.E.P. Connerney, N.F. Ness, in *Mercury*, ed. by F. Vilas, C.R. Chapman, M.S. Matthews (University of Arizona Press, Tucson, 1988), pp. 494–513
J.E.P. Connerney, M.H. Acuña, P. Wasilewski, N.F. Ness, H. Rème, C. Mazelle, D. Vignes, R.P. Lin, D. Mitchell, P. Cloutier, Science **284**, 794–798 (1999)
B.V. Connor, IEEE Trans. Magn. **MAG-4**, 391–397 (1968)
T.G. Cowling, Mon. Not. R. Astron. Soc. **94**, 39–48 (1933)
S.S. Dallas, IEEE Aerospace Conf. Proc. **4**, 173–189 (1997)
L. Davis Jr., E.J. Smith, Trans. AGU **49**, 257 (1968)
L. Davis Jr., E.J. Smith, D.E. Jones, J. Geophys. Res. **78**, 4803–4808 (1973)
L. Davis Jr., E.J. Smith, J. Geophys. Res. **91**, 1373–1380 (1986)
L. Davis Jr., E.J. Smith, J. Geophys. Res. **95**, 15257–15261 (1990)
M. Delva, H. Feldhofer, K. Schwingenschuh, K. Mehlem, Multiple magnetic sensor technique for field measurements in space, EGS–AGU–EUG Joint Assembly, *Abstracts from the meeting held in Nice*, France, 6–11 April 2003, abstract #5053 (2003)
R. Dodge, M.A. Boyles, C.E. Rasbach, Key and driving requirements for the Juno Payload of instruments. Paper AIAA 2007-6111, *AIAA Space Conference & Exposition*, Long Beach, California, September 18–20 (2007)
Sh.Sh. Dolginov, E.G. Eroshenko, L.N. Zhuzgov, N.V. Pushkov, Dokl. Akad. Nauk SSSR **170**, 574–577 (1966)
Sh.Sh. Dolginov, Ye.G. Yeroshenko, L.N. Zhuzgov, J. Geophys. Res. **78**, 4779–4886 (1973)
Sh.Sh. Dolginov, Ye.G. Yeroshenko, L.N. Zhuzgov, J. Geophys. Res. **81**, 3353–3362 (1976)
Sh.Sh. Dolginov, L.N. Zhuzgov, V.A. Sharova, V.B. Buzin, Kosm. Issled. **16**, 827–863 (1978)
Sh.Sh. Dolginov, Adv. Space Res. **12**(8), (8)187–(8)211 (1992)
T.M. Donahue, Science **205**, 41–44 (1979)
M.K. Dougherty, A. Balogh, D.J. Southwood, E.J. Smith, J. Geophys. Res. **101**, 24929–24942 (1996)
M.K. Dougherty, S. Kellock, D.J. Southwood, A. Balogh, E.J. Smith, B.T. Tsurutani, B. Gerlach, K.-H. Glassmeier, F. Gliem, C.T. Russell, G. Erdos, F.M. Neubauer, S.W.H. Cowley, Space Sci. Rev. **114**, 331–383 (2004)
M.K. Dougherty, N. Achilleos, N. Andre, C.S. Arridge, A. Balogh, C. Bertucci, M.E. Burton, S.W.H. Cowley, G. Erdos, G. Giampieri, K.-H. Glassmeier, K.K. Khurana, J. Leisner, F.M. Neubauer, C.T. Russell, E.J. Smith, D.J. Southwood, B.T. Tsurutani, Science **307**, 1266 (2005)
M. Dryer, G.R. Heckman, Solar Phys. **2**, 112–124 (1967)
D. Duret, J. Bonzom, M. Brochier, M. Francès, J.M. Léger, R. Odru, C. Salvi, T. Thomas, A. Perret, Overhauser magnetometer for the Danish Oersted satellite. IEEE Trans. Magn. 3197–3199 (1995)
D. Duret, J.M. Léger, M. Francès, J. Bonzom, F. Alcouffe, A. Perret, J.C. Llorens, C. Baby, Performances of the OVH magnetometer for the Danish Oersted satellite. IEEE Trans. Magn. 4935–4937 (1996)
P. Dyal, C.W. Parkin, C.P. Sonett, Science **169**, 762–764 (1970a)
P. Dyal, C.W. Parkin, C.P. Sonett, IEEE Trans. Geosci. Electron. **GE-8**, 203–215 (1970b)
P. Dyal, C.W. Parkin, C.P. Sonett, in *Apollo 15 Preliminary Science Report*, NASA SP-289, pp. (9)1–(9)16 (1972a)
P. Dyal, C.W. Parkin, P. Cassen, in *Proc. Third Lunar Sci. Conf.*, 3 (Suppl. 3, Geochim. Cosmochem. Acta), pp. 2287–2307 (1972b)
P. Dyal, D.I. Gordon, IEEE Trans. Magn. **Mag-9**, 226–231 (1973)
P. Dyal, C.W. Parkin, W.D. Daily, Rev. Geophys. **12**(4), 568–591 (1974)
W.H. Farthing, W.C. Folz, Rev. Sci. Instrum. **38**, 1023–1030 (1967)
W.H. Farthing, John Hopkins APL Tech. Dig. **1**, 205–209 (1980)
A.M.A. Frandsen, B.V. Connor, J. van Amersfoort, E.J. Smith, IEEE Trans. Geosci. Electron. **GE-16**, 195–198 (1978)
E. Friis-Christensen, H. Lühr, G. Hulot, Earth Planets Space **58**, 351–358 (2006)
E. Friis-Christensen, H. Lühr, D. Knudsen, R. Haagmans, Adv. Space Res. **41**, 210–216 (2008)
M. Fuller, Rev. Geophys. **12**, 23–70 (1974)
M. Fuller, Phys. Chem. Earth **23**, 725–735 (1998)
P.H.M. Galopeau, A. Lecacheux, J. Geophys. Res. **105**, 13089 (2000)
E. Georgescu, H. Vaith, K.-H. Fornaçon, U. Auster, A. Balogh, C.M. Carr, M. Chutter, M.W. Dunlop, M. Foerster, K.-H. Glassmeier, J. Gloag, G. Paschmann, J. Quinn, R. Torbert, in *Cluster and Double Star Symposium*, ed. by K. Fletcher. ESA SP-598, p. 63.1 (2006)

E. Georgescu, H.U. Auster, T. Takada, J. Gloag, H. Eichelberger, K.-H. Fornaçon, P. Brown, C.M. Carr, T.L. Zhang, Adv. Space Res. **41**, 1579–1584 (2008)
J.M. Gloag, E.A. Lucek, L.-N. Alconcel, A. Balogh, P. Brown, C.M. Carr, C.N. Dunford, T. Oddy, J. Soucek, in *The Cluster Active Archive, Studying the Earth's Space Plasma Environment*, ed. by H. Laakso, M.G.T.T. Taylor, C.P. Escoubet. Astrophysics and Space Science Proceedings (Springer, Berlin, 2010), pp.109–128
G. Giampieri, M.K. Dougherty, E.J. Smith, C.T. Russell, Nature **441**, 62 (2006)
K.-H. Glassmeier, F.M. Neubauer, J. Geophys. Res. **98**, 20921–20935 (1993)
K.-H. Glassmeier, J. Grosser, U. Auster, D. Constantinescu, Y. Narita, S. Stellmach, Space Sci. Rev. **132**, 511–527 (2007a)
K.-H. Glassmeier, I. Richter, A. Diedrich, G. Musmann, U. Auster, U. Motschmann, A. Balogh, C. Carr, E. Cupido, A. Coates, M. Rother, K. Schwingenschuh, K. Szego, B. Tsurutani, Space Sci. Rev. **128**, 649–670 (2007b)
K.-H. Glassmeier, H. Boehnhardt, D. Koschny, E. Kürth, I. Richter, Space Sci. Rev. **128**, 1–21 (2007c)
K.-H. Glassmeier, H.-U. Auster, D. Heyner, K. Okrafka, C. Carr, G. Berghofer, B.J. Anderson, A. Balogh, W. Baumjohann et al., Planet. Space Sci. **58**, 287–299 (2010)
D. Gordon, R. Brown, IEEE Trans. Magn. **8**, 76–82 (1972)
O. Gravrand, A. Khokhlov, J.L. Le Mouël, J.M. Léger, Earth Planets Space **53**, 949–958 (2001)
J. Grosser, K.-H. Glassmeier, A. Stadelmann, Planet. Space Sci. **52**, 1251–1260 (2004)
D.A. Gurnett, W.S. Kurth, D.L. Kirchner et al., Space Sci. Rev. **114**, 395–463 (2004)
D.A. Gurnett, A.M. Persoon, W.S. Kurth, J.B. Groene, T.F. Averkamp, M.K. Dougherty, D.J. Southwood, Science **316**, 442 (2007)
C. Guttin, J.M. Léger, E. Stoeckel, J. Phys. III, Suppl. **4**, C4-655–C4-659 (1994)
A.A. Halacsi, Study to develop methods of predicting spacecraft magnetic fields, *NASA* CR-73256 (1969)
J.S. Halekas, D.L. Mitchell, R.P. Lin, S. Frey, L.L. Hood, M.H. Acuña, A.B. Binder, J. Geophys. Res. **106**, 27841–27852 (2001)
F. Hartmann, IEEE Trans. Magn. **MAG-8**, 66–75 (1972)
P.C. Hedgecock, Space Sci. Instrum. **1**, 83–90 (1975)
L.L. Hood, P.J. Coleman, D.E. Wilhelms, Science **204**, 53–57 (1979)
L.L. Hood, A. Zakharian, J. Halekas, D.L. Mitchell, R.P. Lin, M.H. Acuña, A.B. Binder, J. Geophys. Res. **106**, 27,825–27,840 (2001)
H.C. Howe, R.P. Lin, R.E. McGuire, K.A. Anderson, Geophys. Res. Lett. **1**, 101–104 (1974)
G. Hulot, C.C. Finlay, C.G. Constable, N. Olsen, M. Mandea, Space Sci. Rev. (2010). doi:10.1007/s11214-010-9644-0, this issue
E.J. Iufer, Rev. Phys. Appl. **5**, 169–174 (1970)
X. Jia, M.G. Kivelson, K.K. Khurana, R.J. Walker, Space Sci. Rev. (2010). doi:10.1007/s11214-009-9507-8, this issue
C.L. Johnson, H. Uno, M.E. Purucker, B.J. Anderson, H. Korth, J.A. Slavin, S.C. Solomon, in *40th Lunar Planet. Sci. Conf.* Id. 1385 (2009)
J.L. Jørgensen, C.C. Liebe, A.R. Eisenman, G.B. Jensen, in *Spacecraft Guidance, Navigation and Control Systems, ESA SP-381*, ed. by B. Kaldeich-Schuermann (European Space Agency, Paris, 1997), pp. 303–309
M.L. Kaiser, M.D. Desch, J.W. Warwick, J.B. Pearce, Science **209**, 1238 (1980)
M.L. Kaiser, M.D. Desch, W.S. Kurth, A. Lecacheux, F. Genova, B.M. Pedersen, D.R. Evans, in *Saturn*, ed. by T. Gehrels, M.S. Matthews (University of Arizona Press, Tucson, 1984), pp. 378–415
S. Kellock, P. Austin, A. Balogh, B. Gerlach, R. Marquedant, G. Musmann, E. Smith, D. Southwood, S. Szalai, in *Cassini/Huygens: A Mission to the Saturnian Systems*, ed. by L. Horn. Proc. SPIE, vol. 2803 (SPIE, Bellingham, 1996), pp. 141–152
N. Kernevez, H. Glénat, IEEE Trans. Magn. **27**, 5402–5404 (1991)
K.K. Khurana, M.G. Kivelson, D.J. Stevenson, G. Schubert, C.T. Russell, R.J. Walker, C. Polanskey, Nature **395**, 777–780 (1998)
K.K. Khurana, M.G. Kivelson, C.T. Russell, R.J. Walker, S. Joy, in *EGS XXVII General Assembly*, abstract #5119, Nice, 21–26 April 2002
M.G. Kivelson, K.K. Khurana, J.D. Means, C.T. Russell, R.C. Snare, Space Sci. Rev. **60**, 357–383 (1992)
M.G. Kivelson, L.F. Bargatze, K.K. Khurana, D.J. Southwood, R.J. Walker, P.J. Coleman Jr., Science **261**, 331–334 (1993)
M.G. Kivelson, K.K. Khurana, C.T. Russell, R.J. Walker, J. Warnecke, F.V. Coroniti, C. Polanskey, D.J. Southwood, G. Schubert, Nature **384**, 537–541 (1996)
M.G. Kivelson, Z. Wang, S. Joy, K.K. Khurana, C. Polanskey, D.J. Southwood, R.J. Walker, Adv. Space Res. **16**, (4)59–(4)68 (1995)

M.G. Kivelson, K.K. Khurana, F.V. Coroniti, S. Joy, C.T. Russell, R.J. Walker, J. Warnecke, L. Bennett, C. Polanskey, Geophys. Res. Lett. **24**, 2155–2158 (1997)
M.G. Kivelson, K.K. Khurana, M. Volwerk, Icarus **157**, 507–522 (2002)
H. Korth, B. Anderson, M.H. Acuña, J.A. Slavin, N.A. Tsyganenko, S.C. Solomon, R.L. McNutt, Planet. Space Sci. **52**, 733–746 (2004)
H.J. Kramer, *Observation of the Earth and Its Environment: Survey of Missions and Sensors*, 4th edn. (Springer, Berlin, 2002), pp. 595–600
W.S. Kurth, T.F. Averkamp, D.A. Gurnett, J.B. Groene, A. Lecacheux, J. Geophys. Res. **113** (2008). doi:10.1029/2007JA012861
H. Kügler, in *Proceedings 4th International Symposium on Environmental Testing for Space Programmes*, ESA SP-467, pp. 69–72 (2001)
H. Kügler, in *Proc. 5th Int. Symp. on Env. Testing for Space Programmes*, ESA SP-558, pp. 407–411 (2004)
E.R. Lancaster, T. Jennings, M. Morrissey, R. Langel, *NASA Tech. Mem.* 82046, NASA/GSFC (1980)
R.A. Langel, J. Geophys. Res. **79**, 2363–2371 (1974)
R.A. Langel, R.T. Baldwin, in *Types and Characteristics of Data for Geomagnetic Field Modelling, NASA CP-3153*, ed. by R.A. Langel, R.T. Baldwin (NASA, Washington, 1992), pp. 75–136
R. Langel, G. Ousley, J. Berbert, J. Murphy, M. Settle, Geophys. Res. Lett. **9**, 243–245 (1982)
J.-M. Leger, Resonance magnetometer with optical pumping using a monolithic laser. US Patent 5,436,561 (1995)
H.K. Leinweber, C.T. Russell, K. Torkar, T.L. Zhang, V. Angelopoulos, Meas. Sci. Technol. **19**, 055104 (2008). doi:10.1088/0957-0233/19/5/055104
R.P. Lin, K.A. Anderson, R. Bush, R.E. McGuire, J.E. McCoy, in *Proc. Lunar Sci. Conf. 7th*, pp. 2691–2703 (1976)
D.A. Lohr, L.J. Zanetti, B.J. Anderson, T.A. Potemra, J.R. Hayes, R.E. Gold, R.M. Henshaw, F.F. Mobley, D.B. Holland, M.H. Acuña, J.L. Scheifele, Space Sci. Rev. **82**, 255–281 (1997)
H. Lühr, S. Maus, M. Rother, Res. Lett. **29**, 1489 (2002). doi:10.1029/2001GL013845
W. Magnes, D. Pierce, A. Valavanoglou, J. Means, W. Baumjohann, C.T. Russell, K. Schwingenschuh, G. Graber, Meas. Sci. Technol. **14**, 1003–1012 (2003)
W. Magnes, M. Oberst, A. Valavanoglou, H. Hauer, C. Hagen, I. Jernej, H. Neubauer, W. Baumjohann, D. Pierce, J. Means, P. Falkner, Meas. Sci. Technol. **19**, 115801–13 (2008). doi:10.1088/0957-0233/19/11/115801
M. Mandea, C. R. Geosci. **338**, 1002–1011 (2006)
S. Maus, M. Rother, R. Holme, H. Lühr, N. Olsen, V. Haak, Geophys. Res. Lett. **29**, 1702 (2002). doi:10.1029/2001GL013685
S. Matousek, Acta Astron. **61**, 932–939 (2007)
J.W. McAdams, Adv. Astronaut. Sci. **114**, 1549–1567 (2003). Part III: Spaceflight Mechanics
J.E. McCoy, K.A. Anderson, R.P. Lin, H.C. Howe, R.E. McGuire, The Moon **14**, 35–47 (1975)
K. Mehlem, IEEE Trans. Magn. **MAG-14**, 1064–1071 (1978)
K. Mehlem, P. Narvaez, in *Proc. IEEE EMC Symposium*, Seattle, WA, pp. 899–904 (1999)
J.M.G. Merayo, P. Brauer, F. Primdahl, J.R. Petersen, O.V. Nielsen, Meas. Sci. Technol. **11**, 120–132 (2000)
J.M.G. Merayo, J.L. Jørgensen, E. Friis-Christensen, P. Brauer, F. Primdahl, P.S. Jørgensen, T.H. Allin, T. Denver, in *Small Satellites for Earth Observation*, ed. by R. Sandau, H.-P. Röser, A. Valenzuela (Springer, Dordrecht, 2008), pp. 143–151
J.D. Mihalov, C.P. Sonett, J.H. Binsack, M.D. Moutsoulas, Science **171**, 892–895 (1971)
D.L. Mitchell, J.S. Halekas, R.P. Lin, S. Frey, L.L. Hood, M.H. Acuña, A. Binder, Icarus **194**, 401–409 (2008)
F.F. Mobley, L.D. Eckard, G.H. Fountain, G.W. Ousley, IEEE Trans. Magn. **MAG-16**, 758–760 (1980)
D. Möhlmann, W. Riedler, J. Rustenbach, K. Schwingenschuh, J. Kurths, U. Motschmann, T. Roatsch, K. Sauer, H.T.M. Lichtenegger, Planet. Space Sci. **39**, 83–88 (1991)
G. Musmann, Ocean Dyn. **41**, 265–276 (1988)
G. Musmann, Y. Afanassiev, Fluxgate Magnetometers for Space Research. Books on Demand GmbH (2010). ISBN-13: 978-3-8391-3702-4
S. Nazakawa, Y. Iijima, H. Tsunakawa, M. Matsushima, T. Ono, A. Kumamoto, Y. Kasahara, S. Ikegamis, T. Ishikawa, Electromagnetic compatibility of SELENE (KAGUYA). Preprint (2009)
P. Narvaez, Space Sci. Rev. **114**, 385–394 (2004)
N.F. Ness, *NASA/GSFC Report* X-612-64-389 (1964)
N.F. Ness, Space Sci. Rev. **11**, 459–554 (1970)
N.F. Ness, Space Sci. Rev. **21**, 527–553 (1978)
N.F. Ness, Space Sci. Rev. (2010). doi:10.1007/s11214-009-9567-9, this issue
N.F. Ness, B.W. Behannon, C.S. Scearce, S.C. Cantarano, J. Geophys. Res. **72**, 5769–5778 (1967)
N.F. Ness, K.W. Behannon, R.P. Lepping, K.H. Schatten, J. Geophys. Res. **76**, 3564–3573 (1971)

N.F. Ness, K.W. Behannon, R.P. Lepping, Y.C. Whang, K.H. Schatten, Science **183**, 1301–1306 (1974)
N.F. Ness, K.W. Behannon, R.P. Lepping, Y.C. Whang, K.H. Schatten, Science **185**, 151–160 (1975)
N.F. Ness, K.W. Behannon, R.P. Lepping, Y.C. Whang, J. Geophys. Res. **80**, 2708–2716 (1976a)
N.F. Ness, K.W. Behannon, R.P. Lepping, Y.C. Whang, Icarus **28**, 479–488 (1976b)
N.F. Ness, M.H. Acuña, R.P. Lepping, L.F. Burlaga, K.W. Behannon, F.M. Neubauer, Science **204**, 982–987 (1979a)
N.F. Ness, M.H. Acuña, R.P. Lepping, L.F. Burlaga, K.W. Behannon, F.M. Neubauer, Science **206**, 966–972 (1979b)
N.F. Ness, M.H. Acuña, R.P. Lepping, J.E.P. Connerney, K.W. Behannon, L.F. Burlaga, F.M. Neubauer, Science **212**, 211–217 (1981)
N.F. Ness, M.H. Acuña, K.W. Behannon, L.F. Burlaga, J.E.P. Connerney, R.P. Lepping, F.M. Neubauer, Science **215**, 588 (1982)
N.F. Ness, M.H. Acuña, K.W. Behannon, L.F. Burlaga, J.E.P. Connerney, R.P. Lepping, Science **233**, 85–89 (1986)
N.F. Ness, M.H. Acuña, L.F. Burlaga, J.E.P. Connerney, R.P. Lepping, Science **246**, 1473–1478 (1989)
N.F. Ness, M.H. Acuña, J. Connerney, P. Wasilewski, C. Mazelle, J. Sauvaud, D. Vignes, C. d'Uston, H. Reme, R. Lin, D.L. Mitchell, J. McFadden, D. Curtis, P. Cloutier, S.J. Bauer, Adv. Space Res. **23**, 1879–1886 (1999)
F.M. Neubauer, J. Geophys. Res. **80**, 3235–3240 (1975)
F.M. Neubauer, Nature **395**, 749–751 (1998)
F.M. Neubauer, K.H. Schatten, J. Geophys. Res. **79**, 1550–1554 (1974)
F.M. Neubauer, K.H. Glassmeier, M. Pohl, J. Raeder, M.H. Acuña, L.F. Burlaga, N.F. Ness, G. Musmann, F. Mariani, M.K. Wallis, E. Ungstrup, H.U. Schmidt, Nature **321**, 352–355 (1986)
F.M. Neubauer, M.H. Acuña, L.F. Burlaga, B. Franke, B. Gramkow, F. Mariani, G. Musmann, N.F. Ness, H.U. Schmidt, R. Terenzi, E. Ungstrup, M. Wallis, J. Phys. E, Sci. Instrum. **20**, 714–720 (1987)
F.M. Neubauer, H. Marschall, M. Pohl, K.-H. Glassmeier, G. Musmann, F. Mariani, M.H. Acuña, L.F. Burlaga, N.F. Ness, M.K. Wallis, H.U. Schmidt, E. Ungstrup, Astron. Astrophys. **268**, L5–L8 (1993)
O.V. Nielsen, J.R. Petersen, A. Femindez, B. Hernando, P. Spisak, F. Primdahl, N. Moser, Meas. Sci. Technol. **2**, 435–440 (1991)
O.V. Nielsen, J.R. Petersen, F. Primdahl, P. Brauer, B. Hernando, A. Fernandez, J.M.G. Merayo, P. Ripka, Meas. Sci. Technol. **6**, 1099–1115 (1995)
F. Nimmo, D.J. Stevenson, J. Geophys. Res. **105**, 11969–11979 (2000)
H. O'Brien, P. Brown, T. Beek, C. Carr, E. Cupido, T. Oddy, Meas. Sci. Technol. **18**, 3645–3650 (2007)
N. Olsen, Geophys. J. Int. **149**, 454–462 (2002)
N. Olsen, T. Moretto, E. Friis-Christensen, J. Geodyn. **33**, 29–41 (2002)
N. Olsen, L. Tøffner-Clausen, T.J. Sabaka, P. Brauer, J.M.G. Merayo, J.L. Jørgensen, J.-M. Leger, O.V. Nielsen, F. Primdahl, T. Risbo, Earth Planets Space **55**, 11–18 (2003)
N. Olsen, K.-H. Glassmeier, X. Jia, Space Sci. Rev. (2009). doi:10.1007/s11214-009-9563-0, this issue
J.L. Phillips, C.T. Russell, J. Geophys. Res. **92**, 2253–2263 (1987)
S.A. Pope, T.L. Zhang, M. Delva, M. Balikhin, L. Hvizdoš, K. Kudela, Z. Vörös, in *ESA Workshop on Aerospace EMC*, Florence, Italy, 2009
F. Primdahl, J. Phys. E, Sci. Instrum. **12**, 241–253 (1982)
F. Primdahl, in *Measurement Techniques in Space Plasmas: Fields*, ed. by R.F. Pfaff, J.E. Borovsky, D.T. Young. Geophys. Monograph, vol. 103 (American Geophysical Union, Washington, 1998), pp. 85–99
F. Primdahl, P.A. Jensen, J. Phys. E, Sci. Instrum. **15**, 221–226 (1982)
F. Primdahl, T. Risbo, J.M.G. Merayo, P. Brauer, L. Tøffner-Clausen, Meas. Sci. Technol. **17**, 1563–1569 (2006)
M.E. Purucker, Icarus **197**, 19–23 (2009)
Ch. Reigber, H. Luhr, P. Schwintzer, Adv. Space Res. **30**, 129–134 (2002)
N.C. Richmond, L.L. Hood, A preliminary global map of the vector lunar crustal magnetic field based on Lunar Prospector magnetometer data. J. Geophys. Res. **113**, CiteID E02010 (2008). doi:10.1029/2007JE002933
I. Richter, D.E. Brinza, M. Cassel, K.-H. Glassmeier, F. Kuhnke, G. Musmann, C. Othmer, K. Schwingenschuh, B.T. Tsurutani, Geophys. Res. Lett. **28**, 1913–1916 (2001)
W. Riedler, K. Schwingenschuh, Y.G. Yeroshenko, V.A. Styashkin, C.T. Russell, Nature **321**, 288–289 (1986a)
W. Riedler, K. Schwingenschuh, Y.G. Yeroshenko, V.A. Styashkin, C.T. Russell, in *Field, Particle and Wave Experiments on Cometary Missions*, ed. by K. Schwingenschuh, W. Riedler (Verlag der Osterreichischen Akademie der Wissenschaften, Wien, 1986b), pp. 155–168.

T. Risbo, P. Brauer, J.M.G. Merayo, O.V. Nielsen, J.R. Petersen, F. Primdahl, I. Richter, Meas. Sci. Technol. **14**, 674–688 (2003)
S.K. Runcorn, D.W. Collinson, W. O'Reilly, A. Stephenson, N.N. Greenwood, M.H. Battey, Science **167**, 697–699 (1970)
S.K. Runcorn, D.W. Collinson, W. O'Reilly, A. Stephenson, M.H. Battey, A.J. Manson, P.W. Readman, Proc. R. Soc. Lond. Ser. A **325**, 157–174 (1971)
C.T. Russell, Geophys. Res. Lett. **5**, 81–84 (1978)
C.T. Russell, J.G. Luhmann, K. Schwingenschuh, Planet. Space Sci. **40**, 707–710 (1992)
C.T. Russell, R.C. Snare, J.D. Means, R.C. Elphic, IEEE Trans. Geosci. Remote Sens. **GE-18**, 32–35 (1980a)
C.T. Russell, R.C. Elphic, J.G. Luhmann, J.A. Slavin, J. Geophys. Res. **85**, 8319–8332 (1980b)
C.T. Russell, R.C. Elphic, J.G. Luhmann, J.A. Slavin, in *Proc. 11th Lunar Planet. Sci. Conf.*, pp. 1897–1906 (1980c)
C.T. Russell, D.N. Baker, J.A. Slavin, in *Mercury*, ed. by F. Vilas, C.R. Chapman, M.S. Matthews (University of Arizona Press, Tucscon, 1988), pp. 514–561
C.T. Russell, D.E. Huddleston, K.K. Khurana, M.G. Kivelson, Planet. Space Sci. **47**, 521–527 (1999a)
C.T. Russell, D.E. Huddleston, K.K. Khurana, M.G. Kivelson, Planet. Space Sci. **47**, 1101–1109 (1999b)
C.T. Russell, Z.J. Yu, K.K. Khurana, M.G. Kivelson, Adv. Space Res. **28**, 897–902 (2001)
C.T. Russell, Z.J. Yu, K.K. Khurana, S.P. Joy, M.G. Kivelson, in *EGS XXVII General Assembly*, Nice, 21–26 April 2002, abstract #609 (2002)
C.T. Russell, M.K. Dougherty, Space Sci. Rev. (2010). doi:10.1007/s11214-009-9621-7, this issue
T.J. Sabaka, N. Olsen, M.E. Purucker, Geophys. J. Int. **159**, 521–547 (2004)
T. Saito, K. Yumoto, K. Hirao, T. Nagakawa, K. Saito, Nature **321**, 303–307 (1986)
N. Sanders, R. Broce, G. Inouye, IEEE Trans. Magn. **MAG-8**, 591–593 (1972)
J. Saur, F.M. Neubauer, K.-H. Glassmeier, Space Sci. Rev. (2009). doi:10.1007/s11214-009-9581-y, this issue
N. Schilling, K.K. Khurana, M.G. Kivelson, J. Geophys. Res. **109**, CiteID E05006 (2004). doi:10.1029/2003JE002166
R. Schulz, Solar Syst. Res. **43**, 343–352 (2009)
J. Scuffham, A. Balogh, Adv. Space Res. **38**, 616–626 (2006)
J. Scuffham, G. Giampieri, A. Balogh, Adv. Space Res. **38**, 610–615 (2006)
H. Shibuya, M. Toyoshima, M. Matsushima, H. Shimizu, F. Takahashi, H. Tsunakawa, *American Geophysical Union*, abstract #P31B-1399, Fall Meeting 2008
H. Shimizu, F. Takahashi, N. Horii, A. Matsuoka, M. Matsushima, H. Shibuya, H. Tsunakawa, Earth Planets Space **60**, 353–363 (2008)
J.A. Slavin, Adv. Space Res. **33**, 1859–1874 (2004)
J.A. Slavin, R.E. Holzer, in *Proc. Third International Colloquium on Mars, published by the Lunar and Planetary Institute*, pp. 239–241 (1981)
J.A. Slavin, K. Schwingenschuh, W. Riedler, Y. Yeroshenko, J. Geophys. Res. **96**, 11,235–11,241 (1991)
J.A. Slavin, M.H. Acuña, B.J. Andreson et al., Science **324**, 606–610 (2009)
R.E. Slocum, Phys. Rev. Lett. **29**, 1642–1645 (1972)
R.E. Slocum, Radiation source for helium magnetometers. US Patent, No. 5,036,278 (1991)
R.E. Slocum, in *American Geophysical Union, Spring Meeting 2002*, abstract #GP51A-07 (2002)
R.E. Slocum, F.N. Reilly, IEEE Trans. Nucl. Sci. **10**, 165–171 (1963)
R.E. Slocum, P.C. Cabiness, S.L. Blevins, Rev. Sci. Instrum. **42**, 763–766 (1971)
R.E. Slocum, L.D. Schearer, P. Tin, R. Marquedant, J. Appl. Phys. **64**, 6615–6617 (1988)
E.J. Smith, Adv. Space Experiments **25**, pp. 103–130 (1969), AAS 68-186
E.J. Smith, L. Davis Jr., P.J. Coleman Jr., C.P. Sonett, Science **139**, 909 (1963)
E.J. Smith, L. Davis Jr., P.J. Coleman Jr., C.P. Sonett, J. Geophys. Res. **70**, 1571–1586 (1965a)
E.J. Smith, L. Davis Jr., P.J. Coleman Jr., D.E. Jones, Science **149**, 1241–1242 (1965b)
E.J. Smith, L. Davis Jr., D.E. Jones, D.S. Colburn, P.J. Coleman, P. Dyal, C.P. Sonett, Science **183**, 305–306 (1974a)
E.J. Smith, L. Davis Jr., D.E. Jones, P.J. Coleman, D.S. Colburn, P. Dyal, C.P. Sonett, A.M.A. Frandsen, J. Geophys. Res. **79**, 3501–3513 (1974b)
E.J. Smith, B.V. Connor, G.T. Foster Jr., IEEE Trans. Magn. **MAG-11**, 962–980 (1975a)
E.J. Smith, L. Davis Jr., D.E. Jones, P.J. Coleman, D.S. Colburn, P. Dyal, C.P. Sonett, Science **188**, 451–455 (1975b)
E.J. Smith, C.P. Sonett, IEEE Trans. Geosci. Electron. **GE-14**, 154–171 (1976)
E.J. Smith, S. Gulkis, Annu. Rev. Earth Planet. Sci. **7**, 385–415 (1979)
E.J. Smith, L. Davis Jr., D.E. Jones, in *Jupiter*, ed. by T. Gehrels (University of Arizona Press, Tuscon, 1976), pp. 788–829

E.J. Smith, L. Davis Jr., D.E. Jones, P.J. Coleman Jr., D.S. Colburn, P. Dyal, C.P. Sonett, Science **207**, 407–410 (1980a)
E.J. Smith, L. Davis Jr., D.E. Jones, P.J. Colman Jr., D.S. Colburn, P. Dyal, C.P. Sonett, J. Geophys. Res. **85**, 5655–5674 (1980b)
E.J. Smith, B.T. Tsurutani, J.A. Slavin, D.E. Jones, G.L. Siscoe, D.A. Mendis, Science **232**, 382–385 (1986)
E.J. Smith, M.K. Dougherty, C.T. Russell, D.J. Southwood, J. Geophys. Res. **106**, 30,129–30,139 (2001)
R.C. Snare, in *Measurement Techniques in Space Plasmas—Fields*, ed. by R.F. Pfaff, J.E. Borovsky, D.T. Young. Geophys. Monograph, vol. 103 (American Geophysical Union, Washington, 1998), p. 101
R.C. Snare, J.D. Means, IEEE Trans. Magn. **MAG-13**, 1107–1109 (1977)
C.P. Sonett, D.S. Colburn, R.G. Currie, J. Geophys. Res. **72**, 5503–5507 (1967)
D.J. Southwood, M.K. Dougherty, A. Balogh, S.W.H. Cowley, E.J. Smith, B.T. Tsurutani, C.T. Russell, G.L. Siscoe, G. Erdos, K.-H. Glassmeier, F. Gliem, F.M. Neubauer, J. Geophys. Res. **106**, 30,109–30,128 (2001)
S. Stanley, J. Bloxham, Nature **428**, 151–153 (2004)
S. Stanley, J. Bloxham, Icarus **184**, 556–572 (2006)
S. Stanley, G.A. Glatzmaier, Space Sci. Rev. (2010). doi:10.1007/s11214-009-9573-y, this issue
D.J. Stevenson, AIP Conf. Proc. **24**, 781–784 (1975)
D.J. Stevenson, Science **208**, 746–748 (1980)
D.J. Stevenson, Geophys. Astrophys. Fluid Dyn. **21**, 113–127 (1982)
D.J. Stevenson, Rep. Progr. Phys. **46**, 555–620 (1983)
D.J. Stevenson, Space Sci. Rev. (2010). doi:10.1007/s11214-009-9572-z, this issue
D.J. Stevenson, T. Spohn, G. Schubert, Icarus **54**, 466–489 (1983)
T.L. Zhang, W. Baumjohann, M. Delva, H.-U. Auster, A. Balogh, C.T. Russell et al., Planet. Space Sci. **54**, 1336–1343 (2006)
T.L. Zhang, M. Delva, W. Baumjohann, M. Volwerk et al., Planet. Space Sci. **56**, 785–789 (2008)